Use of ground and air-based photogrammetry for soil erosion assessment

Bernardo Moreira Candido

This dissertation is submitted for the degree of Doctor of Philosophy

September 2019

Lancaster Environment Centre

I dedicate this thesis to my dear cousin, friend and brother
Clebinho (In Memorian), for being part of the most important
moments of my life.
May God always bless you.

Declaration

This thesis has not been submitted in support of an application for another degree at this university. It is the result of my own work and includes nothing that is the outcome of work done in collaboration except where specifically indicated. Many of the ideas in this thesis were the product of discussion with my supervisors John N. Quinton, Michael R. James and Marx L. N. Silva.

Bernardo Moreira Candido

Lancaster University, UK

ACKNOWLEDGMENTS

This thesis would not have been possible without the support and guidance of many people. I would like to thank:

My wife Isabella, for doing this PhD with me. The many challenges brought by this PhD were overcome by both of us, together.

My parents, who taught me responsibility and respect. My grandparents, who gave me all the support to live and study in Lavras.

My brothers, Vitor Hugo, Pablo and Miguel, for always remind me of smiling.

I would particularly like to thank my supervisors for their constant support, advices and patience over the past few years:

Professor Marx Silva, who believed in me since the beginning and always supported me to dedicate myself to one of the things that I most love to do, learning.

Professor John Quinton, who I am glad to have had the opportunity of meeting and knowing his inspiring way of doing science and dealing with those starting in the sciences, like me.

Professor Mike James, who made me even more fascinated with photogrammetry through his papers and through the interesting discussions we had while I joined his group.

Special mention must go to Wellington de Lima, for his assistance in setting up the flights over the experiments at UFLA while I was in Lancaster.

I thank the society from where the resources for my research came from. I thank the Conselho Nacional de Desenvolvimento Científico e Tecnológico (CNPq, grant numbers 233547/2014-2, 149622/2014-7, 306511/2017-7 and 202938/2018-2) for providing the scholarship and all necessary resources while I was in Lancaster, UK. I also thank the Fundação de Amparo a Pesquisa do Estado de

Minas Gerais (FAPEMIG, grant numbers APQ-00802-18 and CAG-APQ 01053-15) for providing the resources to buy equipment and software used in this work.

All my colleagues from the Federal University of Lavras for a very nice environment where I have been throughout the last 10 years.

All my friends and brother from UDV, for being my second family while I was in Lavras.

Lancaster University and the Lancaster Environment Centre. The Federal University of Lavras and the Department of Soil Science.

Finally, I am grateful to God and M. Gabriel, who taught me the importance of being humble and gave me the strength to overcome the challenges of this PhD.

GENERAL ABSTRACT

Water erosion affects all types of soils around the world at different intensities. However, in tropics water erosion is the most important form of soil erosion and has received much concern in the last decades. The major challenge in soil conservation is the development and implementation of strategies to mitigate the erosion processes in urban and rural areas. Thus, understanding the processes involved in each type of water erosion (sheet, rill and gully erosion), as well as its quantification, is a key factor in managing and developing soil conservation and erosion mitigation strategies. In that way, this thesis aims to investigate the efficiency of ground and air-based photogrammetry for soil erosion assessment, as well as to address some gaps in our understanding of the evolution of erosive processes in its different forms of occurrence. In doing so, we evaluated the factors that influence the development of erosion in micro and macro scales, with experiments in the laboratory and in the field. In the first chapter, it was evaluated the influence of gradient change and runoff volumes on rill erosion process, using digital close-range photogrammetry in a laboratory soil flume. In addition, morphological rill parameters were estimated to allow a better understanding of the rill erosion behaviour under different treatments. The results showed that the flow velocity in rills increased with water flow and slope, showing a strong correlation with the amount of rill erosion. On steep slopes the soil erosion was dominated by the rill erosion with less rill network density while, on low slopes, there were other types of soil erosion occurring together with rill erosion, causing the reduction of soil loss due to rill erosion. The digital close-range photogrammetry technique provided millimetric precision, which is sufficient for rill erosion investigations. In the second chapter aimed to evaluate the efficiency of SfM based on UAV images in obtaining accurate measurements of soil loss in areas of sheet erosion, under natural rainfall, where channelized erosion is not the principal mechanism. The measurements acquired from SfM were compared to the sediments collected in each soil erosion plots. The results of the soil losses obtained by UAV-SfM presented a high correlation with the sediments collected in the plots. This is of great relevance in the context of the monitoring and modelling of water erosion, since the quantification of soil loss around the world is mainly done using plots, a method that presents high operational cost. In addition, the study of laminar erosion through the UAV-SfM allows not only to calculate the soil loss values but to visualize the spatial variation of the erosion process (detachment, transport and deposition) practically in real time along the area. In the third chapter it was evaluated the application of UAV-SfM technique in a gully system. For the first time, a study was carried out evaluating the relative contribution of the different types of erosion (sheet, rill and gully sidewall) in the gully development. This was possible due to the millimetric level of precision of the point clouds, allowing to evaluate even the contribution of the laminar erosion, which is new in gullies studies. As a result, it was possible to quantify sediments volumes stored in the channels and lost from the gully system, as well as to determine the main sediment sources. The study suggests that the main source of sediments in the gully was due to the mass movements, followed by rills and sheet erosion. The UAV-SfM proved to be effective in the gully monitoring. The results findings by this thesis indicate that the use of ground and air-based photogrammetry are precise tools in detecting soil surface changes and can be used to assess water erosion in its various forms of occurrence in nature. In addition, the UAV-SfM has proven to be a very useful technique for monitoring soil erosion over time, especially in hard-to-reach areas.

Keywords: Structure-from-motion. Unmanned aerial vehicle. Digital close-range photogrammetry. Erosion plot. Sheet erosion. Rill erosion. Gully erosion.

Contents

1. Literature Review

1.1 Soil erosion

Soil is a non-renewable resource and essential to the maintenance of humans and natural ecosystems, ensuring food, fibre, energy, and water quality. However, the unplanned use of soil can cause its degradation, with negative economic and social impacts on present and future generations. Currently, about 800 million people are food insecure around the world (Lal, 2013) and 2 billion have no access to safe and affordable water (World Health Organization and UNICEF, 2015; Paul Obade and Lal, 2016). In addition, the world's population will probably reach 9·1 billion people in 2050 and, consequently, the demand for food is also expected to increase dramatically (Alexandratos and Bruinsma, 2012).

Considering that about 50 % of the earth's surface is dedicated to agriculture and more than 99·7% of the human’s food comes from the land (Pimentel, 2006) the soil is a key factor in order to provide food and water security for future generations. Thus, understanding the factors that cause its degradation is essential to implement reclamations and preservations measures of ecosystems and rural areas.

In natural conditions, the slow loss of soil by the erosion process has been responsible for transforming and sculpting the landscape throughout geologic time, through the mobilisation and deposition of soil particles, by water and air. However, whilst the natural soil erosion is a feature of any terrestrial ecosystem, anthropogenic soil erosion accelerates the geomorphic processes of natural soil erosion (Lal, 2001).

Anthropogenic soil erosion, most associated with inappropriate land use, has significantly accelerated the rate of soil loss, causing considerable impacts in environment, economy and society worldwide. According to Pimentel (2006), about 80% of the agricultural land around the world suffers from severe or moderate soil erosion and 10% shows slight signals of erosion. As a result, about 30% of productive areas worldwide have become infertile and abandoned for agriculture use (Pimentel, 2006). Therefore, due to the long-term negative impact on the soil properties, soil erosion becomes the most important land degradation problem in the world (Eswaran et al., 2001) and has been prioritized by environmental scientists and policymakers worldwide.

1.2 Soil erosion by water

Water erosion affects all types of soils around the world at different intensities (Blanco and Lal, 2010). However, in tropics water erosion is the most important form of soil erosion and has received much concern in the last decades. It is one of the most serious forms of soil degradation and a major threat to the sustainability of agroecosystems, affecting around one billion hectares worldwide (Lal, 2003; Luffman et al., 2015; Xu et al., 2016; Guo et al., 2017).

The water erosion is based on the processes of detachment, transport and deposition of soil particles by the impact of raindrop and overland runoff, mainly taking the form of concentrated and dispersed flow (Ellison, 1947; Kinnell, 2006; Shi et al., 2010). This refers to the movement of soil particles along the surface, with deposition of eroded materials in the lower slope regions and in watercourses (Horton, 1945). This eroded material may generate new soil, or simply silting rivers and lakes. In addition, these sediment losses are often associated with organic matter, nutrients, heavy metals and other contaminants, resulting in direct and indirect impacts on soil functions, and on aquatic and terrestrial ecosystems (Glendell and Brazier, 2014; Rickson, 2014).

Different factors influence the evolution of the erosive process, such as the intensity and duration of rainfall, soil properties, slope, vegetation cover and soil surface roughness (Le Bissonnais et al., 2005; Mahmoodabadi and Sajjadi, 2016; Wang et al., 2017; Hao et al., 2019).

The impact of raindrops plays an important role in water erosion because, in addition to promoting the detachment of soil particles, it also promotes increased transport of sediment through runoff (Zhang and Wang, 2017) (Figure 1). Soil properties, such as the texture and aggregates stability, affect soil resistance to detachment and water infiltration (Le Bissonnais, 1996). Thus, the effects of rain intensity on erosion strongly depends on soil type (Defersha and Melesse, 2012; Wu et al., 2018).

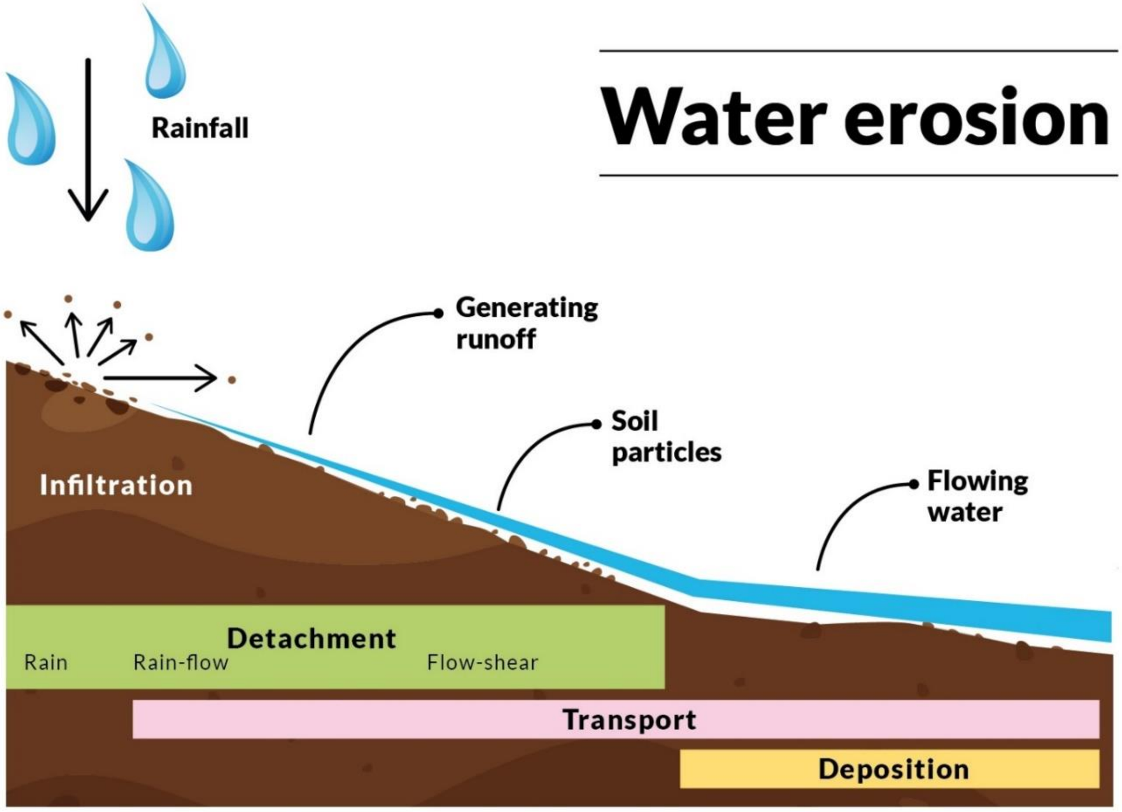

Fig. 1. Illustration of rainsplash erosion and soil-particle mobilization, transport, and deposition.

The major challenge of soil conservation today is the efficient implementation of conservation management practices in agricultural and urban areas. For this, the knowledge of the dynamics of erosion in the area, through the spatiotemporal studies of erosive processes and types of erosion (sheet, rills and gullies), as well as its quantification, are key factors in managing and developing soil conservation and erosion mitigation strategies.

1.2.1 Sheet erosion

Sheet erosion, also known as laminar and interrill erosion, mainly affects agricultural areas in sloping regions in tropical environments (Le Bissonnais et al., 1998; Sirjani and Mahoodabadi, 2014). Once it is started, the runoff develops in small rills and the portion of the overland flow flowing between the rills is called sheet erosion or interrill erosion. This type of erosion is characterized by the detachment of fine soil particles present on the surface due to the impact of raindrops and the dispersed flow over the surface (Kinnell, 2013; Maïga-Yaleu et al., 2015).

Laminar erosion is the most common type of erosion, corresponding to about 70% of total soil erosion, occurring simultaneously to other erosive processes (Blanco and Lal, 2010). This type of erosion is affected by several factors such as rainfall intensity, slope gradient, vegetation, soil properties and surface characteristics, such as roughness and crusting (Dlamini et al., 2011; Ibáñez et al., 2016; Zhang et al., 2019).

During the sheet erosion process, a mixture of water and solid particles flows over the soil as a sheet, causing erosion through loss of successive layers of soil (Fournier, 1960). Sheet erosion can carry only fine particles, such as clay and silt, while coarse particles are associated with the development of rill erosion (Hao et al., 2019). This selective behaviour in the transport of the most useful soil particles is a harmful aspect of the sheet flow. Thus, in hillslopes sheet erosion is much more severe than gully erosion (Descroix et al., 2008), contributing to soil fertility loss, reduced productivity and being the initial stage of rill erosion (Müller-Nedebock et al., 2016).

The correct measurement of soil losses from sheet erosion is a key factor for the development of conservation planning. However, the main form of monitoring and quantification of sheet erosion in the world is through erosion plots under natural and artificial rainfall (Cerdan et al., 2010; García-Ruiz et al., 2015; Guo et al., 2015; Zhao et al., 2019). This traditional method is considered a time-consuming and costly process, restricting the evaluation of sheet erosion only in places where there is a plot system installed in the field (Cerdan et al., 2010).

With the recent advances in technology, the use of high-resolution digital elevation models (DEM) has assumed an important role in the study of processes that occur on the earth's surface. These advances have become possible with the development of techniques such as Structure-from-Motion (SfM), which combines the principles of photogrammetry and modern methods of computer vision (Westoby et al., 2012).

The SfM photogrammetry has been widely used to evaluate erosion in rills and gullies (Bazzoffi, 2015; Nouwakpo et al., 2015; Hänsel et al., 2016; Neugirg et al., 2016; Morgan et al., 2017). However, there are no studies with the application of SfM in the measurement of sheet erosion in areas where there is no incision of channels of concentrated water flow. Thus, because of the difficulty in monitoring the loss of millimetre layers of soil, remote monitoring of sheet erosion is a major challenge in soil science.

1.2.2 Rill erosion

Rills are small concentrated flow paths in which the depth and flow velocity are greater than in the surface runoff and with erosive potential higher than sheet erosion (Govers et al., 2007; Blanco and Lal, 2010). Rill erosion occurs from soil detachment by scouring and transport of soil particles by the concentrated water flow in these narrow channels (Bagnold, 1966).

Rill erosion is the main source of sediments and mechanisms for sediment transport in erosive processes on hillslopes and is related to the increase in erosion rates (Bryan, 1990; Rauws, 1987; Di Stefano et al., 2017). Once the rills established in an area, sediment production can increase by up to 40 times (Morgan, 1977). In addition, the presence of rills in sloping areas may correspond to 70% to 90% of total erosion (Renard et al., 1997; Zheng and Tang, 1997).

Rill erosion is widespread mainly in dry regions, being one of the main forms of soil loss in agricultural lands around the world (Cerdan et al., 2002; Polyakov and Nearing, 2003; Hancock et al., 2008; Wirtz et al., 2012; Di Stefano et al., 2013; Jiang et al., 2018; Zhang et al., 2019). In addition, the transport of sediments from the hillslopes to the watercourses becomes more efficient as a rill network develops (Berger et al., 2010; Heras et al., 2011; Aksoy et al., 2013; He et al., 2016; Sofia et al., 2017). Thus, rill erosion affects significantly the micromorphology of the hillslopes, generating large rill networks in the area and increasing the connectivity between the sediments, besides promoting permanent changes in the landscape with the evolution of rills to gullies (Berger et al., 2010; Wirtz et al., 2010).

Several experiments have been conducted to study the formation and development of rill erosion (Bryan and Rockwell, 1998; Berger et al., 2010; Wirtz et al., 2012; He et al., 2016; Di Stefano et al., 2017; Lu et al., 2017; Sofia et al., 2017; Jiang et al., 2018; Zhang et al., 2019). Researches have shown that rill erosion is directly related to increased runoff (Mancilla et al., 2005), rainfall intensity (Brunton and Bryan, 2000) and slope (Berger et al., 2010).

However, Wirtz et al. (2012) have shown that rill erosion is not a simple function related to rainfall intensity or slope gradient, but a complex process that is influenced by surface sealing, rill development, headcut incision, and sidewall collapse. Therefore, there are differences in the experimental results obtained, which vary according to the type of soil, rainfall conditions and spatial and temporal scales (Devente and Poesen, 2005; Govers et al., 2007).

In the field, the slope gradient is constantly changing along the hillslope, influencing the flow velocity and, consequently, the rill network. However, due to the absence of adequate techniques for spatial monitoring of rill development, few studies are evaluating the influence of gradient change and runoff volume on the formation of the rill network. Thus, there is a gap to be explored in the study of morphological indicators and the spatial behaviour of the formation of rill networks at different slopes and water flow intensities. The understanding of the evolution and behaviour of rill erosion in each situation helps the development of prevention and recovery strategies in areas affected by this type of soil erosion.

1.2.3 Gully erosion

Gully erosion is the most severe type of water erosion when compared to sheet and rill erosion, promoting soil degradation and causing large volumes of soil loss in agricultural areas (Valentin et al., 2005). Gully erosion occurs when the concentrated runoff begins to develop deep channels that expand into deep trenches over time (Luffman et al., 2015). Erosion caused by the concentrated water flow reduces the soil surface layer through the formation of gullies, impacting soil fertility and polluting adjacent streams (Allen et al., 2018; Bastola et al., 2018; Zabihi et al., 2018). In the early stages, the gullies develop rapidly to great depths, making difficult to control through agricultural machinery and making the area recovery expensive (Nachtergaele and Poesen, 2002; Vanwalleghem et al., 2005).

Gullies represent a serious environmental problem in the world, occurring mainly in arid and semi-arid regions, where vegetation density is low, reducing soil protection to rainfall and runoff (Sankey and Draut, 2014). Although the gullies occupy around 5% of the area of a catchment, gully erosion represents the largest source of soil eroded sediments and may reach 94% of total erosion (Makanzu Imwangana et al., 2014; Ionita et al., 2015; Bollati et al., 2016). The development of gullies in an area promotes connectivity between sediment channels and increases the volume of runoff on the hillslope, generating flood risks and sedimentation of rivers, lakes and reservoirs (Poesen et al., 2003).

Gully erosion is controlled by several factors such as surface runoff, water movements in the sub-surface, and soil piping (Kirkby and Bracken, 2009; Poesen et al., 2018). Although the gullies are the result of natural processes that occur on the soil surface, human action can accelerate the formation and development of this type of erosion (Thorburn and Wilkinson, 2013; Rodrigo Comino et al., 2015).

Therefore, to prevent these negative effects and implement reclamation strategies, it is necessary to understand the magnitude of the problem and the factors causing it (Mitas and Mitasova, 1998; Poesen et al., 2003). Measuring gully erosion can be very challenging because it is a highly complex process, with erosion and deposition occurring at the same time and in the same place (Gómez-Gutiérrez et al., 2014). Consequently, the measurement accuracy of gullies is directly influenced by the spatial scales and by their morphology (Castillo et al., 2012). In this way, to provide reliable data about soil losses, several techniques for monitoring and quantifying gully erosion are currently available, such as pins (Chaplot, 2013), Light Detection and Ranging (LiDAR) (Perroy et al., 2010), hand-held mobile laser scanner (James and Quinton, 2014) and aerial photographs and photogrammetric techniques (Marzolff and Poesen, 2009; Castillo et al., 2012).

Among the new methodologies used to monitor gully erosion, photogrammetry combined with three-dimensional (3-D) soil surface reconstruction methods have been widely used recently (Castillo et al., 2012; Gómez-Gutiérrez et al., 2014; Kaiser et al., 2014; Di Stefano et al., 2017; Ben

Slimane et al., 2018). However, although many studies have described the formation and development of gullies (Harvey, 1992; Vandekerckhove et al., 1998; Sidorchuk et al., 2003; Conoscenti et al., 2014), few studies have evaluated the dynamics of the sediments movements and the relative contribution of each process to total erosion within the gullies complex. The understanding of the contribution rates of sheet erosion, rills and gully sidewalls, as well as the quantification of the sediments stored in the channels, is of great importance in the establishment of strategies for prevention, monitoring and recovery of gullies (Hosseinalizadeh et al., 2019).

1.3 Topographic methods for soil erosion assessment

During an erosive event, the soil surface is in continuous transformation. Depending on the volume of soil transported, the erosion processes can result in considerable topographic variations and may have negative impacts on agriculture (Heng et al., 2010). Thus, several technologies were developed by soil scientists to obtain detailed information on soil surface variation caused by erosion (Nouwakpo and Huang, 2012).

Contact techniques such as erosion pins and rillmeter have been used for a long time to study the changes of soil surface during the erosion process (Elliot et al., 1997; Kronvang et al., 2012). However, although the observed change in the exposed part of the pin can be used to calculate the amount of erosion after an erosive event, the accuracy of this technique is limited by the low spatial coverage due to the small number of pins installed in the monitored area (Sirvent et al. 1997; Zhang et al., 2011). Otherwise, the rillmeter technique can obtain accurate soil surface change data but may affect the results due to the contact between the device and the soil surface (Elliot et al., 1997). Simple topographic instruments (theodolites or total stations) with contact with the measured surface were also used for a long time to study soil topography (Moser et al., 2007).

Measurement techniques of soil microtopography change that do not involve surface contact during measurements are preferred as they do not cause any impact on the soil and reduce the time of data acquisition (Jester and Klik, 2005). Laser scanning and digital photogrammetry have been the most used technologies among non-contact methodologies to obtain soil surface topographic data at high-resolution.

1.3.1 High-resolution topographic methods

High-resolution topographic data is of great importance in almost all applications of geosciences (James and Quinton, 2014; Agüera-Vega et al., 2018; Deng et al., 2018; Azareh et al., 2019). Thus, a wide variety of methods have evolved to meet these surveys demands such as aerial and terrestrial laser scanning, multibeam SONAR, RTK-DGPS and total station (Brasington, 2010; Höfle and Rutzinger, 2011; Hohenthal et al., 2011; Castillo et al., 2012; Day et al., 2013; James and Quinton, 2014; Vinci et al., 2015).

However, despite the diversity of methods available, the generation of high-resolution DEMs requires large investments in personal training and equipment. Thus, with the emergence of image-based methods such as digital photogrammetry, it has drastically reduced these operating costs (Westoby et al., 2012).

1.3.2 Digital photogrammetry

Digital photogrammetry is becoming increasingly accessible to researchers and users, due to the development of methods that allow accurate calibration of non-metric cameras and the reliable automation of the photogrammetric process (Fonstad et al., 2013). Since the emergence of aerial and digital close-range digital photogrammetry, this powerful technique has been widely used in obtaining 3-D soil surface models (Rieke-Zapp and Nearing, 2005; Gessesse et al., 2010; Heng et al., 2010; Nouwakpo and Huang, 2012; Stöcker et al., 2015; Guo et al., 2016; Goetz et al., 2018).

Recent advances in digital close-range photogrammetry technologies, as well as computer vision, have made it possible to generate high-resolution soil topography models from consumer-grade digital cameras (Berger et al., 2010; Heng et al., 2010; Nouwakpo and Huang, 2012; Nouwakpo et al., 2014; Guo et al., 2016). Digital photogrammetry has the advantage of having a low cost of equipment acquisition, with values several orders of magnitude lower than laser scanner (Nouwakpo et al., 2014).

The reduction in cost and improvements in the quality of compact cameras and single lens reflex (SLR) has popularized the access to photogrammetric modelling and encouraged the use in several areas of the geosciences (Lane, 2000; Chandler et al., 2002; Brasington and Smart, 2003; Marzolff and Poesen, 2009; Bird et al., 2010). Thus, the digital close-range photogrammetry technique has been widely used to generate DEMs with sufficient resolution for soil microtopography studies (Babault et al., 2004; Rieke-Zapp and Nearing, 2005; Aguilar et al., 2009; Nouwakpo and Huang, 2012; Guo et al., 2016).

Several studies have demonstrated the efficiency of the high-resolution digital close-range photogrammetry in monitoring soil erosion, producing DEMs with resolution of grids ranging from 1 to 15 mm (Brasington and Smart, 2003; Abd Elbasit et al., 2009; Aguilar et al., 2009; Rieke-Zapp and Nearing, 2005; Heng et al., 2010; Stöcker et al., 2015; Guo et al., 2016).

1.3.3 Unmanned aerial vehicles (UAV)

In order to overcome the limitations of traditional photogrammetry techniques, the use of photographic cameras coupled in unmanned aerial vehicles (UAVs) to acquire images of the soil surface has been objecting of study in the last years (Bemis et al., 2014; James and Robson , 2014; Nex and Remondino, 2014; Clapuyt et al., 2016; Di Stefano et al., 2017; O'Connor et al., 2017; Eltner et al., 2018). UAVs have some advantages over piloted aircraft and satellites, especially in relation to low cost, operational flexibility and better spatial and temporal resolution of the images from which DEMs can be derived (Laliberte et al., 2010; Harwin and Lucieer, 2012; Anderson and Gaston, 2013; Hugenholtz et al., 2015; Balek and Blahůt, 2017).

UAVs require less time to acquire data when compared to other techniques, reducing operating costs. Moreover, the resolution and accuracy of the results obtained by UAVs cannot be achieved through satellite images (Immerzeel, et al., 2014), being useful mainly in places where the use of other techniques is not feasible or dangerous. The UAVs provide a convenient remote sensing platform for studies of landslides due to their ability to acquire high-resolution images on terrains difficult to access (Lucieer et al., 2014).

1.3.4 Structure-from-Motion (SfM)

The structure-from-motion (SfM) is based on the basic principles of traditional photogrammetry, where the three-dimensional (3-D) structure can be reconstructed from a series of overlapping images (Westoby et al., 2012). This technique combines the computational vision approaches SfM (Ullman, 1979) and multiview-stereo (MVS; Seitz et al., 2006) algorithms. However, it differs from conventional photogrammetry as the scene geometry, orientations and camera positions are estimated automatically, without the need to specify in advance targets with known 3-D positions.

These parameters are computed simultaneously using the highly redundant, iterative bundle adjustment procedure, based on the resources database extracted automatically from the set of overlapping images (Snavely, 2008). This technique is suitable for sets of images that have a high degree of overlap, with the capture of the entire 3-D structure of the scene from a wide variety of positions (James and Robson, 2012), or according to the name, images obtained from a moving sensor.

Based on the calculations of orientation and location of the camera, overlapping images are used to reconstruct a 3-D sparse point cloud from the surface. However, this result is still insufficiently detailed and very noisy for high-quality 3-D reconstruction. In the last years, 3-D reconstruction software has increased the quality of the models by linking the output of SfM with MVS image matching algorithms. The MVS process effectively filters out the noise and greatly increases the density of reconstructed points (James and Robson, 2012). Thus, the point clouds resulting from SfM-MVS processing are of sufficient quality to generate high-resolution DEMs but do not have geospatial or scale information. In this way, measurements of ground control points are necessary for later georeferencing of the models.

Studies show that the use of SfM combined with MVS can produce high-resolution 3-D models (centimetres to millimetres), with results similar to those generated from airborne LiDAR and terrestrial laser scanner (TLS) (Castillo et al., 2012; James and Quinton, 2014; Eltner et al., 2015). However, there are no studies evaluating the accuracy of eroded volumes estimates via UAV-SfM and comparing them with independent measurements by collecting eroded soil in a controlled environment, such as erosion plots. The validation of UAV-SfM for monitoring thin surface layers of erosion opens up opportunities in the use of this technique to elaborate strategies to control complex erosive environments, where sheet erosion, grooves and gullies occur at the same time.

Recent studies were carried out using UAV images and SfM techniques for soil surface mapping. The applications include monitoring of soil microtopography change detection (Eltner et al., 2018), rill and interrill erosion (Eltner et al., 2015), gully erosion (Gómez-Gutiérrez et al., 2014; Stöcker et al., 2015; Glendell et al., 2017), wind erosion (Pagán et al., 2019) and landslides (Lucieer et al., 2014; Turner et al., 2015). However, there is a gap of work using UAV-SfM to evaluate the behaviour of laminar erosion in the field, as well as the relative contributions of different types of erosion in the gully development.

In this thesis, the SfM-MVS technique will be treated only as SfM, following the trend of the recent works in the area of geosciences (Hänsel et al., 2016; Cook, 2017; Mlambo et al., 2017; Mosbrucker et al., 2017; Agüera-Vega et al., 2018; Zimmer et al., 2018).

1.4 Thesis aims and objectives

This project aims to investigate the efficiency of aerial and terrestrial photogrammetry in the detailed study of water erosion, as well as to address some gaps in our understanding of the evolution of erosive processes in its different forms (sheet, rill and gully erosion) of occurrence. In doing so, we will evaluate the factors that influence the development of erosion in micro and macro scales, with experiments in the laboratory and in the field. The hypothesis is that the use of digital photogrammetry will allow soil scientists to accurately quantify laminar erosion, making it possible to replace traditional methods, such as erosion plots, with high operating costs. In addition, high-resolution photogrammetry will make it possible to study the dynamics of evolution of the gullies in space and time, allowing to evaluate the relative contribution of sheet erosion and rills to the growth of the gullies complex.

This thesis sets out to develop an understanding at both a methodological level and in terms of wider soil erosion processes understandings. From a tightly controlled study to field observations, it will study the accuracy and application of ground and air-based photogrammetry for soil erosion assessment at a range of scales. The thesis consists of three experimental chapters designed to address the following objectives:

(i) To evaluate the influence of gradient change and runoff volumes on rill erosion process, using digital close-range photogrammetry in a laboratory soil flume. In addition, to estimate morphological rill parameters for a better understanding of the rill erosion behaviour under different treatments. (Chapter 1)

(ii) To evaluate the efficiency of SfM based on UAV images in obtaining accurate measurements of soil loss in areas of sheet erosion, under natural rainfall, where channelized erosion is not the principal mechanism. The measurements acquired from SfM were compared to the sediments collected in each soil erosion plots. (Chapter 2)

(iii) A case study of a gully in Brazil using SfM to provide a detailed understanding of the dynamics of the sediment movements in the gully system. Thus, to evaluate the relative contribution of sheet and rill erosion, as well as gully sidewalls to sediment generation. In addition, to quantify the total volume of sediments stored and lost from the gully system over time. (Chapter 3)

1.5 References

Abd Elbasit, M.A., Anyoji, H., Yasuda, H., Yamamoto, S., 2009. Potential of low cost close-range photogrammetry system in soil microtopography quantification. Hydrol. Process. 23, 1408–1417.

Agüera-Vega, F., Carvajal-Ramírez, F., Martínez-Carricondo, P., López, J.S-H., Mesas-Carrascosa, F.J., García-Ferrer, A., Pérez-Porras, F.J., 2018. Reconstruction of extreme topography from UAV structure from motion photogrammetry. Measurement 121, 127–138.

Aguilar, M.A., Aguilar, F.J., Negreiros, J., 2009. Off-the-shelf laser scanning and close-range digital photogrammetry for measuring agricultural soils microrelief. Biosyst. Eng. 103, 504–517.

Aksoy, H., Unal, N.E., Cokgor, S., Gedikli, A., Yoon, J., Koca, K., Inci, S.B., Eris, E., Pak, G., 2013. Laboratory experiments of sediment transport from bare soil with a rill. Hydrol. Sci. J. 58, 1505–1518.

Alexandratos, N., Bruinsma, J., 2012. World agriculture towards 2030/2050: the 2012 revision. ESA Working paper No. 12-03. Rome, FAO.

Allen, P.M., Arnold, J.G., Auguste, L., White, J., Dunbar, J., 2018. Application of a simple headcut advance model for gullies. Earth Surf. Process. Landf. 43, 202–217.

Anderson, K., Gaston, K.J., 2013. Lightweight unmanned aerial vehicles will revolutionize spatial ecology. Front. Ecol. Environ. 11, 138–146.

Azareh, A., Rahmati, O., Rafiei-Sardoo, E., Sankey, J.B., Lee, S., Shahabi, H., Ahmad, B.B., 2019. Modelling gully-erosion susceptibility in a semi-arid region, Iran: Investigation of applicability of certainty factor and maximum entropy models. Sci. Total Environ. 655, 684–696.

Babault, J., Bonnet, S., Crave, A., Van Den Driessche, J., 2004. Influence of piedmont sedimentation on erosion dynamics of an uplifting landscape: an experimental approach. Geology 33, 301–304.

Bagnold, R.A., 1966. An approach to the sediment transport problem from general physics. USGS Prof. Pap. 442-I. U.S. Gov. Print. Office, Washington, DC.

Balek, J., Blahůt, J., 2017. A critical evaluation of the use of an inexpensive camera mounted on a recreational unmanned aerial vehicle as a tool for landslide research, Landslides 14, 1217–1224.

Bastola, S., Dialynas, Y.G., Bras, R.L., Noto, L.V., Istanbulluoglu, E., 2018. The role of vegetation on gully erosion stabilization at a severely degraded landscape: a case study from Calhoun Experimental Critical Zone Observatory. Geomorphology 308, 25–39.

Bazoffi, P., 2015. Measurement of rill erosion through a new UAV-GIS methodology. Ital. J. Agron. 10 (s1), 708.

Bemis, S.P., Micklethwaite, S., Turner, D., James, M.R., Akciz, S., Thiele, S.T., Ali Bangash, H., 2014. Ground-based and UAV-Based photogrammetry: a multi-scale, high-resolution mapping tool for structural geology and paleoseismology. J. Struct. Geol. 69, P163–P178.

Ben Slimane, A., Raclot, D., Rebai, H., Le Bissonnais, Y., Planchon, O., Bouksila F., 2018. Combining field monitoring and aerial imagery to evaluate the role of gully erosion in a Mediterranean catchment (Tunisia). Catena 170, 73–83.

Berger, C., Schulze, M., Rieke-Zapp, D., Schlunegger, F., 2010. Rill development and soil erosion: a laboratory study of slope and rainfall intensity. Earth Surf. Process. Landf. 35, 1456–1467.

Bird, S., Hogan, D., Schwab, J., 2010. Photogrammetric monitoring of small streams under a riparian forest canopy. Earth Surf. Process. Landf. 35, 952–970.

Blanco, H., Lal, R., 2010. Principles of soil conservation and management. Springer, Heidelberg, Germany, 620 pp.

Bollati, I., Vergari, F., DelMonte,M., Pelfini,M., 2016. Multitemporal dendrogeomorphological analysis of slope instability in upper Orcia Valley (Southern Tuscany, Italy). Geogr. Fis. Din. Quat. 39, 105–120.

Brasington, J., 2010. From grain to floodplain: hyperscale models of braided rivers. J. Hydraul. Res. 48, 52–53.

Brasington, J., Smart, R.M.A., 2003. Close range digital photogrammetric analysis of experimental drainage basin evolution. Earth Surf. Process. Landf. 28, 231–247.

Brunton, D.A., Bryan, R.B., 2000. Rill network development and sediment budgets. Earth Surf. Process. Landf. 25, 783–800.

Bryan, R.B., 1990. Knickpoint evolution in rillwash. Catena Supplement 17, 111–132.

Bryan, R.B., Rockwell, D.L., 1998. Water table control on rill initiation and implications for erosional response. Geomorphology 23, 151–169.

Castillo, C., Pérez, R., James, M.R., Quinton, J.N., Taguas, E.V., Gómez, J.A., 2012. Comparing the accuracy of several field methods for measuring gully erosion. Soil Sci. Soc. Am. J. 76, 1319–1332.

Cerdan, O., Govers, G., Le Bissonnais, Y., Van Oost, K., Poesen, J., Saby, N., Gobin, A., Vacca, A., Quinton, J., Auerswald, K., Klik, A., Kwaad, F., Raclot, D., Ionita, I., Rejman, J., Rousseva, S., Muxart, T., Roxo, M., Dostal, T., 2010. Rates and spatial variations of soil erosion in Europe: A study based on erosion plot data. Geomorphology 122, 167–177.

Cerdan, O., Le Bissonnais, Y., Couturier, A., Saby, N., 2002. Modelling interrill erosion in small cultivated catchments. Hydrol. Process. 16, 3215–3226.

Chandler, J., Ashmore, P., Paola, C., Gooch, M., Varkaris, F., 2002. Monitoring river-channel change using terrestrial oblique digital imagery and automated digital photogrammetry. Ann. Assoc. Am. Geogr. 92, 631–644.

Chaplot, V., 2013. Impact of terrain attributes, parent material and soil types on gully erosion. Geomorphology 186, 1–11.

Clapuyt, F., Vanacker, V., Van Oost, K., 2016. Reproducibility of UAV-based earth topography reconstructions based on Structure-from-Motion algorithms. Geomorphology 260, 4–15.

Conoscenti, C., Angileri, S., Cappadonia, C., Rotigliano, E., Agnesi, V., Märker, M., 2014. Gully erosion susceptibility assessment by means of GIS-based logistic regression: a case of Sicily (Italy). Geomorphology 204, 399–411.

Cook, K.L., 2017. An evaluation of the effectiveness of low-cost UAVs and structure from motion for geomorphic change detection. Geomorphology 278, 195–208.

Day, S.S., Gran, K.B., Belmont, P., Wawrzyniec, T., 2013. Measuring bluff erosion part 2: pairing aerial photographs and terrestrial laser scanning to create a watershed scale sediment budget. Earth Surf. Process. Landf. 38, 1068–1082.

Defersha, M.B., Melesse, A.M., 2012. Effect of rainfall intensity, slope and antecedent moisture content on sediment concentration and sediment enrichment ratio. Catena 90, 47–52.

Deng, L., Mao, Z., Li, X., Hu, Z., Duan, F., Yan, Y., 2018. UAV-based multispectral remote sensing for precision agriculture: A comparison between different cameras. ISPRS-J. Photogramm. Remote Sens. 146, 124–136.

Descroix L., González Barrios, J.L., Viramontes, D., Poulenard, J., Anaya, E., Esteves, M., Estrada, J., 2008. Gully and sheet erosion on subtropical mountain slopes: Their respective roles and the scale effect. Catena 72, 325–339.

Devente, J., Poesen, J., 2005. Predicting soil erosion and sediment yield at the basin scale: scale issues and semi-quantitative models. Earth Sci. Rev. 71, 95–125.

Di Stefano, C., Ferro, V., Palmeri, V., Pampalone, V., 2017. Measuring rill erosion using structure from motion: A plot experiment. Catena 156, 383–392.

Di Stefano, C., Ferro, V., Pampalone, V., Sanzone, F., 2013. Field investigation of rill and ephemeral gully erosion in the Sparacia experimental area, South Italy. Catena 101, 226–234.

Dlamini, P., Orchard, C., Jewitt, G., Lorentz, S., Titshall, L., Chaplot, V., 2011. Controlling factors of sheet erosion under degraded grasslands in the sloping lands of KwaZulu-Natal, South Africa. Agric. Water Manage. 98, 1711–1718.

Elliot, W., Laflen, J., Thomas, A., Kohl, K., 1997. Photogrammetric and rillmeter techniques for hydraulic measurement in soil erosion studies. Trans. ASAE 40, 157–165.

Ellison, W.D., 1947. Soil erosion studies: I. Agric. Eng. 28, 145–146.

Eltner, A., Baumgart, P., Maas, H.G., Faust, D., 2015. Multi-temporal UAV data for automatic measurement of rill and interrill erosion on loess soil. Earth Surf. Process. Landf. 40, 741–755.

Eltner, A., Maas, H-G., Faust, D., 2018. Soil micro-topography change detection at hillslopes in fragile Mediterranean landscapes. Geoderma 313, 217–232.

Eswaran, H., Lal, R., Reich, P.F., 2001. Land degradation: An overview. In: E.M. Bridges, F.W.T. Penning de Vries, L.R. Oldeman, S. Sombatpanit, S.J. Scherr (Eds.), Response to land degradation. Science Publishers, Enfield, pp. 20-35.

Fonstad, M.A., Dietrich, J.T., Courville, B.C., Jensen, J.L., Carbonneau, P.B., 2013. Topographic structure from motion: a new development in photogrammetric measurement. Earth Surf. Process. Landf. 38, 421–430.

Fournier, F., 1960. Climate et érosion. Presses Universitaires de France, Paris. 201 pp.

García-Ruiz, J.M., Beguería, S., Nadal-Romero, E., Gonzalez-Hidalgo, J.C., Lana-Renault, N., Sansjuan, Y., 2015. A meta-analysis of soil erosion rates across the world. Geomorphology 239, 160–173.

Gessesse, G.D., Fuchs, H., Mansberger, R., Klik, A., Rieke-Zapp, D.H., 2010. Assessment of erosion, deposition and rill development on irregular soil surfaces using close range digital photogrammetry. Photogramm. Rec. 25, 299–318.

Glendell, M., Brazier, R.E., 2014. Accelerated export of sediment and carbon from a land-scape under intensive agriculture. Sci. Total Environ. 476–477, 643–656.

Glendell, M., McShane, G., Farrow, L., James, M., Quinton, J., Anderson, K., Evans, M., Benaud, P., Rawlins, B., Morgan, D., Jones, L., Kirkham, M., DeBell, L., Quine, T., Lark, M., Rickson, J., Brazier, R., 2017. Testing the utility of structure from motion photogrammetry reconstructions using small unmanned aerial vehicles and ground photography to estimate the extent of upland soil erosion. Earth Surf. Process. Landf. 42, 1860–1871.

Goetz, J., Brenning, A., Marcer, M., Bodin, X., 2018. Modeling the precision of structure-from-motion multi-view stereo digital elevation models from repeated close-range aerial surveys. Remote Sens. Environ. 210, 208–216.

Gómez-Gutiérrez A, Schnabel S, Berenguer-Sempere F, Lavado- Contador F, Rubio-Delgado J. 2014. Using 3D photo-reconstruction methods to estimate gully headcut erosion. Catena 120, 91–101.

Govers G, Giménez R, Van Oost K. 2007. Rill erosion: exploring the relationship between experiments, modelling and field observations. Earth-Sci. Rev. 84, 87–102.

Guo, Q., Hao, Y., Liu, B., 2015. Rates of soil erosion in China: A study based on runoff plot data. Catena 2015, 68–76.

Guo, Z.L., Ma, M.J., Cai, C.F., Wu, Y.W., 2017. Combined effects of simulated rainfall and overland flow on sediment and solute transport in hillslope erosion. J. Soils Sediments 4, 1–13.

Guo, M., Shi, H., Zhao, J., Liu, P., Welbourne, D., Lin, Q., 2016. Digital close range photogrammetry for the study of rill development at flume scale. Catena 143, 265–274.

Hancock, G.R., Loughran, R.J., Evans, K.G., Balog, R.M., 2008. Estimation of soil erosion using field and modelling approaches in an undisturbed Arnhem Land catchment, Northern Territory, Australia. Geogr. Res. 46, 333–349.

Hänsel, P., Schindewolf, M., Eltner, A., Kaiser, A., Schmidt, J., 2016. Feasibility of high-resolution soil erosion measurements by means of rainfall simulations and SfM photogrammetry. Hydrology 3 (38).

Hao, H., Wang, J., Guo, Z., Hua, L., 2019. Water erosion processes and dynamic changes of sediment size distribution under the combined effects of rainfall and overland flow. Catena, 173, 494–504.

Harvey, A.M., 1992. Process interactions, temporal scales and the development of hillslope gully systems: Howgill Fells, northwest England. Geomorphology 5, 323–344.

Harwin, S., Lucieer, A., 2012. Assessing the accuracy of georeferenced point clouds produced via multi-view stereopsis from unmanned aerial vehicle (UAV) imagery. Remote Sens. 4, 1573–1599.

He, J.J., Sun, L.Y., Gong, H.L., Cai, Q.G., Jia, L.J., 2016. The characteristics of rill development and their effects on runoff and sediment yield under different slope gradients. J. Mt. Sci. 13, 397–404.

Heng, B.C.P., Chandler, J.H., Armstrong, A., 2010. Applying close-range digital photogrammetry and soil erosion studies. The Photogrammetric Record 25, 240–265.

Heras, M.M., Espigares, T., Merino-Martín, L., Nicolau, J.M., 2011. Water-related ecological impacts of rill erosion processes in Mediterranean-dry reclaimed slopes. Catena 84, 114–124.

Höfle, B., Rutzinger, M., 2011. Topographic airborne LiDAR in geomorphology: a technological perspective. Z. Geomorphol. 55, 1–29.

Hohenthal, J., Alho, P., Hyyppa, J., Hyyppa, H., 2011. Laser scanning applications in fluvial studies. Prog. Phys. Geogr. 35, 782–809.

Horton, R.E., 1945. Erosional development of streams and their drainage basins; hydrophysical approach to quantitative morphology. Geol. Soc. Am. Bull. 56, 275–370.

Hosseinalizadeh, M., Kariminejad, N., Chen, W., Pourghasemi, H.R., Alinejad, M., Behbahani, A.M., Tiefenbacher, J.P., 2019. Spatial modelling of gully headcuts using UAV data and four best-first decision classifier ensembles (BFTree, Bag-BFTree, RS-BFTree, and RF-BFTree). Geomorphology 329, 184–193.

Hugenholtz, C.H., Walker, J., Brown, O., Myshak, S., 2015. Earthwork volumetrics with an unmanned aerial vehicle and softcopy photogrammetry, J. Surv. Eng. 141, 06014003

Ibáñez, J., Lavado Contador, J.F., Schnabel, S., Martínez, V.J., 2016. Evaluating the influence of physical, economic and managerial factors on sheet erosion in rangelands of SW Spain by performing a sensitivity analysis on an integrated dynamic model. Sci. Total Environ. 544, 439–449.

Immerzeel, W.W., Kraaijenbrink, P.D.A., Shea, J.M., Shrestha, A.B., Pellicciotti, F., Bierkens, M.F.P., de Jong, S.M., 2014. High-resolution monitoring of Himalayan glacier dynamics using unmanned aerial vehicles. Remote Sens. Environ. 150, 93–103.

Ionita, I., Fullen, M.A., Zgłobicki, W., Poesen, J., 2015. Gully erosion as a natural and human-induced hazard. Nat. Hazards 79, 1–5.

James, M.R., Quinton, J.N., 2014. Ultra-rapid topographic surveying for complex environments: the hand-held mobile laser scanner (HMLS). Earth Surf. Process. Landf. 39, 138–142.

James, M.R., Robson, S., 2012. Straightforward reconstruction of 3D surfaces and topography with a camera: Accuracy and geoscience application. J. Geophys. Res. 117, F03017.

James, M.R., Robson, S., 2014. Mitigating systematic error in topographic models derived from UAV and ground-based image networks. Earth Surf. Process. Landf. 39, 1413–1420.

Jester, W., Klik, A., 2005. Soil surface roughness measurement – methods, applicability, and surface representation. Catena 64, 174–192.

Jiang, F., Zhan, Z., Chen, J., Lin, J., Wang, M.K., Ge, H., 2018. Rill erosion processes on a steep colluvial deposit slope under heavy rainfall in flume experiments with artificial rain. Catena 169, 46–58.

Kaiser, A., Neugirg, F., Rock, G., Müller, C., Haas, F., Ries, J., Schmidt, J., 2014. Small-scale surface reconstruction and volume calculation of soil erosion in complex Moroccan gully morphology using structure from motion. Remote Sens. 6, 7050–7080.

Kinnell, P.I.A., 2006. Simulations demonstrating interaction between coarse and fine sediment loads in rain-impacted flow. Earth Surf. Process. Landf. 31, 355–367.

Kinnell, P.I.A., 2013. Modeling of the effect of flood depth on sediment discharged by rain-impacted flows from sheet and interrill erosion areas: a review. Hydrol. Process. 27, 2567–2578.

Kirkby, M.J., Bracken, L.J., 2009. Gully processes and gully dynamics. Earth Surf. Process. Landf. 34, 1841–1851.

Kronvang, B., Audet, J., Baattrup-Pedersen, A., Jensen, H.S., Larsen, S.E., 2012. Phosphorus load to surface water from bank erosion in a Danish lowland river basin. J. Environ. Qual. 41, 304–313.

Lal, R., 2001. Soil degradation by erosion. Land Degrad. Dev. 12, 519–529.

Lal, R., 2003. Soil erosion and the global carbon budget. Environ. Int. 29, 437–450.

Lal, R. 2013. Climate-strategic agriculture and the water-soil-waste nexus. J. Plant Nutr. Soil Sci. 176, 479-493.

Laliberte, A., Herrick, J., Rango, A., Winters, C., 2010. Acquisition, orthorectification, and object-based classification of unmanned aerial vehicle (UAV) imagery for rangeland monitoring. Photogramm. Eng. Remote. Sens. 76, 661–672.

Lane, S.N., 2000. The measurement of river channel morphology using digital photogrammetry. Photogramm. Rec. 16, 937–957.

Le Bissonnais, Y., 1996. Aggregate stability and assessment of soil crustibility: I. Theory and methodology. Eur. J. Soil Sci. 47, 425–437.

Le Bissonnais, Y., Benkhadra, H., Chaplot, V., Fox, D., King, D., Daroussin, J., 1998. Crusting, runoff and sheet erosion on silty loamy soils at various scales and upscaling from m2 to small catchments. Soil Tillage Res. 46, 69–80.

Le Bissonnais, Y., Cerdan, O., Lecomte, V., Benkhadra, H., Souchère, V., Martin, P., 2005. Variability of soil surface characteristics influencing runoff and interrill erosion. Catena 62, 111–124.

Lu, X., Li, Y., Washington-Allen, R.A., Li, Y., Li, H., Hu, Q., 2017. The effect of grid size on the quantification of erosion, deposition, and rill network. Int. Soil Water Cons. Res. 5, 241–251.

Lucieer, A., Jong, S.M.d., Turner, D., 2014. Mapping landslide displacements using Structure from Motion (SfM) and image correlation of multi-temporal UAV photography. Prog. Phys. Geogr. 38, 97–116.

Luffman, I.E., Nandi, A., Spiegel, T., 2015. Gully morphology, hillslope erosion, and precipitation characteristics in the Appalachian Valley and Ridge province, southeastern USA. Catena 133, 221–232.

Mahmoodabadi, M., Sajjadi, S.A., 2016. Effects of rain intensity, slope gradient and particle size distribution on the relative contributions of splash and wash loads to rain-induced erosion. Geomorphology 253, 159–167.

Maïga-Yaleu, S.B., Chivenge, P., Yacoub, H., Guiguemde, I., Karambiri, H., Ribolzi, O., Bary, A., Chaplot, V., 2015. Impact of sheet erosion mechanisms on organic carbon losses from crusted soils in the Sahel. Catena 126, 60–67.

Makanzu Imwangana, F., Dewitte, O., Ntombi, M., Moeyersons, J., 2014. Topographic and road control of mega-gullies in Kinshasa (DR Congo). Geomorphology 217, 131–139.

Mancilla, G.A., Chen, S., Mccool, D.K., 2005. Rill density prediction and flow velocity distributions on agricultural areas in the Pacific Northwest. Soil Tillage Res. 84, 54–66.

Marzolff, I., Poesen, J., 2009. The potential of 3D gully monitoring with GIS using high resolution aerial photography and a digital photogrammetry system. Geomorphology 111, 48–60.

Mitas, L., Mitasova, H., 1998. Distributed soil erosion simulation for effective erosion prevention. Water Resour. Res. 34, 505–516.

Mlambo, R., Woodhouse, I., Gerard, F., Anderson, K., 2017. Structure from motion (SfM) Photogrammetry with drone data: a low cost method for monitoring greenhouse gas emissions from forests in developing countries. Forests 8, 68.

Morgan, R.P.C., 1977. Soil Erosion in the United Kingdom: Field studies in the Silsoe area, 1973–1975. Occasional Paper. 4 Nat. Coll. Agr. Eng. Silsoe, UK.

Morgan, J.A., Brogan, D.J., Nelson, P.A., 2017. Application of Structure-from-Motion photogrammetry in laboratory flume. Geomorphology 276, 125–143.

Mosbrucker, A.R., Major, J.J., Spicer, K.R., Pitlick, J., 2017. Camera system considerations for geomorphic applications of SfM photogrammetry. Earth Surf. Process. Landf. 42, 969–986.

Moser, K., Ahn, C., Noe, G., 2007. Characterization of microtopography and its influence on vegetation patterns in created wetlands. Wetlands, 27, 1081–1097.

Müller-Nedebock, D., Chivenge, P., Chaplot, V., 2016. Selective organic carbon losses from soils by sheet erosion and main controls. Earth Surf. Process. Landf. 41, 1399–1408.

Nachtergaele, J., Poesen, J., 2002. Spatial and temporal variations in resistance of loess-derived soils to ephemeral gully erosion. Eur. J. Soil Sci. 53, 449–463.

Neugirg, F., Stark, M., Kaiser, A., Vlacilova, M., Della Seta, M., Vergari, F., Schmidt, J., Becht, M., Haas, F., 2016. Erosion processes in calanchi in the upper Orcia Valley, southern Tuscany, Italy based on multitemporal high-resolution terrestrial LiDAR and UAV surveys. Geomorphology 269, 8–22.

Nex, F., Remondino, F., 2014. UAV for 3D mapping applications: a review. Appl. Geomatics 6, 1–15.

Nouwakpo, S.K., Huang, C.-H., 2012. A simplified close-range photogrammetric technique for soil erosion assessment. Soil Sci. Soc. Am. J. 76, 70–84.

Nouwakpo, S.K., James, M.R., Weltz, M.A., Huang, C.-H., Chagas, I., Lima, L., 2014. Evaluation of structure from motion for soil microtopography measurement. Photogramm. Rec. 29, 297–316.

Nouwakpo, S., Weltz, M., McGwire, K., 2015. Assessing the performance of structure-from-motion photogrammetry and terrestrial lidar for reconstructing soil surface microtopography of naturally vegetated plots. Earth Surf. Process. Landf. 41, 308–322.

O'Connor, J., Smith, M.J., James, M.R., 2017. Cameras and settings for aerial surveys in the geosciences: Optimising image data. Prog. Phys. Geogr. 41, 325–344.

Pagán, J.I., Bañon, L., López, I., Bañon, C., Aragonés, L., 2019. Monitoring the dune-beach system of Guardamar del Segura (Spain)using UAV, SfM and GIS techniques. Sci. Total Environ. 687, 1034–1045.

Paul Obade, V., Lal, R., 2016. Towards a standard technique for soil quality assessment. Geoderma 265, 96-102.

Perroy, R.L., Bookhagen, B., Asner, G.P., Chadwick, O.A., 2010. Comparison of gully erosion estimates using airborne and ground-based LIDAR on Santa Cruz Island, California. Geomorphology 118, 288–300.

Pimentel, D., 2006. Soil erosion: a food and environmental threat. Environ. Dev. Sustain. 8, 119-137.

Poesen, J., Nachtergaele, J., Verstraeten, G., Valentin, C., 2003. Gully erosion and environmental change: importance and research needs. Catena 50, 91–133.

Poesen, J., Vanwalleghem, T., Deckers, J., 2018. Gullies and closed depressions in the Loess Belt: scars of human–environment interactions. Landscapes and Landforms of Belgium and Luxembourg. Springer, Cham, pp. 253–267.

Polyakov, V.O., Nearing, M.A., 2003. Sediment transport in rill flow under deposition and detachment conditions. Catena 51, 33–43.

Rauws, G., 1987. The initiation of fills on plane beds of non-cohesive sediments. Catena Supplement 8, 107–118.

Renard, K.G., Foster, G.R., Weesies, G.A., McCool, D.K., Yoder, D.C., 1997. Predicting soil erosion by water: a guide to conservation planning with the revised universal soil loss equation (RUSLE). Agriculture Handbook 703US Department of Agriculture, Washington, DC.

Rieke-Zapp, D.H., Nearing, M.A., 2005. Digital close range photogrammetry for measurement of soil erosion. Photogramm. Rec. 20, 69–87.

Rodrigo Comino, J., Brings, C., Lassu, T., Iserloh, T., Senciales, J.M., Martínez Murillo, J.F., Ruiz Sinoga, J.D., Seeger, M., Ries, J.B., 2015. Rainfall and human activity impacts on soil losses and rill erosion in vineyards (Ruwer Valley, Germany). Solid Earth 6, 823–837

Rickson, R.J., 2014. Can control of soil erosion mitigate water pollution by sediments? Sci. Total Environ. 468–469, 1187–1197.

Sankey, J.B., Draut, A.E., 2014. Gully annealing by aeolian sediment: field and remote-sensing investigation of aeolian–hillslope–fluvial interactions, Colorado River corridor, Arizona, USA. Geomorphology 220, 68–80.

Seitz, S.M., Curless, B., Diebel, J., Scharstein, D., Szeliski, R., 2006. A comparison and evaluation of multi-view stereo reconstruction algorithms. Computer Vision and Pattern Recognition, 2006 IEEE Computer Society Conference on, pp. 519–528.

Shi, Z.H., Yan, F.L., Li, L., Li, Z.X., Cai, C.F., 2010. Interrill erosion from disturbed and undisturbed samples in relation to topsoil aggregate stability in red soils from subtropical China. Catena 81, 240–248.

Sidorchuk, A., Marker, M., Moretti, S., Rodolfi, G., 2003. Gully erosion modelling and landscape response in the Mbuluzi River catchment of Swaziland. Catena 50, 507–525.

Sirjani, E., Mahoodabadi, M., 2014. Effects of sheet flow rate and slope gradient on sediment load. Arab. J. Geosci. 7, 203–210.

Sirvent, J., Desir, G., Gutierrez, M., Sancho, C., Benito, G., 1997. Erosion rates in badland areas recorded by collectors, erosion pins and profilometer techniques (Ebro Basin, NE-Spain). Geomorphology 18, 61–75.

Snavely, N., Seitz, S., Szeliski, R., 2008. Modeling the world from internet photo collections. Int. J. Comput. Vis. 80, 189–210.

Sofia, G., Di Stefano, C., Ferro, V., Tarolli, P., 2017. Morphological similarity of channels: from linear erosional features (rill, gully) to alpine rivers. Land Degrad. Dev. 28, 1717–1728.

Stöcker, C., Eltner, A., Karrasch, P., 2015. Measuring gullies by synergetic application of UAV and close range photogrammetry – A case study from Andalusia, Spain. Catena 132,1–11.

Thorburn, P.J., Wilkinson, S.N., 2013. Conceptual frameworks for estimating the water quality benefits of improved agricultural management practices in large catchments. Agric. Ecosyst. Environ. 180, 192–209.

Turner, D., Lucieer, A., de Jong, S., 2015. Time Series Analysis of Landslide Dynamics Using an Unmanned Aerial Vehicle (UAV), Remote Sens. 7, 1736–1757.

Ullman, S., 1979. The interpretation of visual motion. MIT Press Series in Artificial Intelligence. MIT Press, Cambridge, Massachusetts, and London, England.

Valentin, C., Poesen, J., Yong, L., 2005. Gully erosion: impacts, factors and control. Catena 63, 132–153.

Vandekerckhove, L., Poesen, J., Wijdenes, D.O., de Figueiredo, T., 1998. Topographical thresholds for ephemeral gully initiation in intensively cultivated areas of the Mediterranean. Catena 33, 271–292.

Vanwalleghem, T., Poesen, J., Van Den Eeckhaut, M., Nachtergaele, J., Deckers, J., 2005. Reconstructing rainfall and land-use conditions leading to the development of old gullies. The Holocene 15, 378–386.

Vinci, A., Brigante, R., Todisco, F., Mannocchi, F., Radicioni, F., 2015. Measuring rill erosion by laser scanning. Catena 124, 97–108.

Wang, B., Steiner, J., Zheng, F., Gowda, P., 2017. Impact of rainfall pattern on interrill erosion process. Earth Surf. Process. Landf. 42, 1833–1846.

Westoby, M.J., Brasington, J., Glasser, N.F., Hambrey, M.J., Reynolds, J.M., 2012. ‘Structure-from-Motion’ photogrammetry: a low-cost, effective tool for geoscience applications. Geomorphology 179, 300–314.

Wirtz, S., Seeger, M., Ries, J.B., 2010. The rill experiment as a method to approach a quantification of rill erosion process activity. Z. Geomorphol. 54, 47–64.

Wirtz, S., Seeger, M., Ries, J.B., 2012. Field experiments for understanding and quantification of rill erosion processes. Catena 91, 21–34.

Wirtz, S., Seeger, M., Zell, A., Wagner, C., Wagner, J.F., Ries, J.B., 2013. Applicability of different hydraulic parameters to describe soil detachment in eroding rills. PLoS One 8 (5), e64861.

World Health Organization, UNICEF., 2015. Progress on Sanitation and Drinking Water: 2015 Update and Millennium Development Goals Assessment. World Health Organization, UNICEF, Division of Communication, 3 United Nations Plaza, New York 10017, USA.

Wu, X., Wei, Y., Wang, J., Xia, J., Cai, C., Wei, Z., 2018. Effects of soil type and rainfall intensity on sheet erosion processes and sediment characteristics along the climatic gradient in central-south China. Sci. Total Environ. 621, 54–66.

Xu, M., Li, Q., Wilson, G., 2016. Degradation of soil physicochemical quality by ephemeral gully erosion on sloping cropland of the hilly Loess Plateau, China. Soil Tillage Res. 155, 9–18.

Zabihi, M., Mirchooli, F., Motevalli, A., Darvishan, A.K., Pourghasemi, H.R., Zakeri, M.A., Sadighi, F., 2018. Spatial modelling of gully erosion in Mazandaran Province, northern Iran. Catena 161, 1–13.

Zhang, J., Yang, M., Deng, X., Liu, Z., Zhang, F., 2019. The effects of tillage on sheet erosion on sloping fields in the wind-water erosion crisscross region of the Chinese Loess Plateau. Soil Tillage Res. 187, 235–245.

Zhang, X.C., Wang, Z.L., 2017. Interrill soil erosion processes on steep slopes. J. Hydrol. 548, 652–664.Zhang,

Zhao, J., Yang, Z., Govers, G., 2019. Soil and water conservation measures reduce soil and water losses in China but not down to background levels: Evidence from erosion plot data. Geoderma 337, 729–741.

Zhang, J., Zheng, F., Wen, L., 2011. Methodology of dynamic monitoring gully erosion process using 3D laser scanning technology. Bull. Soil Water Conserv. 31, 89–94.

Zheng, F.L., Tang, K.L., 1997. Rill erosion process of steep slope land of the Loess Plateau. International Journal of Sediment Research 12, 52–59.

Zimmer, B., Liutkus-Pierce, C., Marshall, S.T., Hatala, KG., Metallo, A., Rossi, V., 2018. Using differential structure-from-motion photogrammetry to quantify erosion at the Engare Sero footprint site, Tanzania. Quat. Sci. Rev. 198, 226–241.

2. Rill erosion and morphology development in response to changing discharge and slope profiles

2.1 Introduction

Rill erosion is the removal of soil by concentrating water flow into a narrow channel and, hence, increasing the sediment transport capacity of the flow (Chen et al., 2016). It represents an intermediate process between sheet and gully erosion (Jackson, 1997). The presence of rills in runoff plots can increase sediment yield by 40 times (Morgan, 1977). It can lead to large soil losses, water pollution, and damage to drainage networks (Morgan, 2005; Bewket and Sterk, 2003; Poesen et al., 2003). In agricultural lands, rill erosion can be easy to observe, but it is difficult to measure due to its stochastic nature (He et al., 2016). During an erosive event, the soil surface is in continuous transformation, which can result in substantial topography variation at scales of few millimetres to as much as a metre, depending on the volume of transported soil (Gessesse et al., 2010; Heng et al., 2010).

Several studies have focused on rill erosion processes (Favis-Mortlock et al., 2000; Wirtz et al., 2012), but research on rill network development remains limited. Most study only the main rills, ignoring the important role of the secondary channels on the rill network development (Mancilla et al., 2005; Shen et al., 2015).

The amount of soil loss in sloping croplands and rangelands is affected significantly by the rill morphology since water flow within rills has the capacity to transport large volumes of sediment (Favis-Mortlock et al., 2000; Gatto, 2000). Considering that rills change morphologically in time and space, it is necessary to consider temporal and spatial variations in their development (Lei and Nearing, 1998; Shen et al., 2015).

As rills are micro-relief channels that are generally less than 0·3 m deep and wide (Nearing et al., 1997), a detailed spatial study requires high-resolution digital elevation models (DEMs). Digital close-range photogrammetry has been widely used within soil erosion studies to generate high-resolution DEMs (Abd Elbasit et al., 2009; Aguilar et al., 2009; Guo et al., 2016; Nouwakpo and Huang, 2012; Rieke-Zapp and Nearing, 2005). This method is based on images of the soil surface taken from multiple positions at relatively low height (Abd Elbasit et al., 2009), enabling 3D analysis of the rill erosion development at millimetre resolution, with instantaneous data acquisition using high-resolution consumer-grade cameras.

However, the presence of vegetation in the study area affects the 3D reconstruction of the soil surface by aerial images. In these cases, there are mathematical algorithms that filter the vegetation present in the 3D point cloud, for example CANUPO (Brodu and Lague, 2012) and CSF (Zhang et al., 2016), allowing to estimate the soil surface with compromised accuracy. Thus, soil surface DEMs obtained by digital close-range photogrammetry enable the volumetric change detection and the assessment of microtopography change over the time (Eltner et al., 2018).

Since conducting experiments on rill erosion processes and microtopography change are challenging in field environments, studies that simulate surface runoff in laboratory erosion plots are necessary to understand the basic processes and mechanisms of rill formation, rill density, rill network and distribution, as well as the magnitude of water flow associated with transport and development of rill erosion.

To date, rill erosion studies have focus on rill formation over slopes of constant gradient (Armstrong et al., 2011; Favis-Mortlock, 1998; Gessesse et al., 2010; Shen et al., 2016). However, rill development and morphology in regions where the gradient changes along the slope, have yet to be assessed. This works intends to address this research gap by evaluating the influence of gradient change and runoff volumes on rill erosion process, using a soil flume (3·9 × 1·4 m). In addition, morphological rill parameters will be estimated to allow a better understanding of the rill erosion behaviour under different treatments.

2.2 Materials and Methods

2.2.1 Experimental design

All experiments were conducted in the soil erosion laboratory of the Lancaster Environment Centre, Lancaster University, UK. A soil flume (3·9 m ×

1·4 m) was used to evaluate the relationship between slope and water flow in rill formation. The flume was divided into two regions of different slope in order to assess sedimentation and rill formation under varying gradients and surface runoff. In the region A (see Figure 1), located 0 m to 1·5 m from the top of the slope, the slope was either 6% or 9%, while in region B, the slope had a constant value of 2% for both slopes (Figure 1). Whilst forming the surface, the slope gradient was measured using a handheld clinometer (Suunto PM-5, accuracy ± 0·44%).

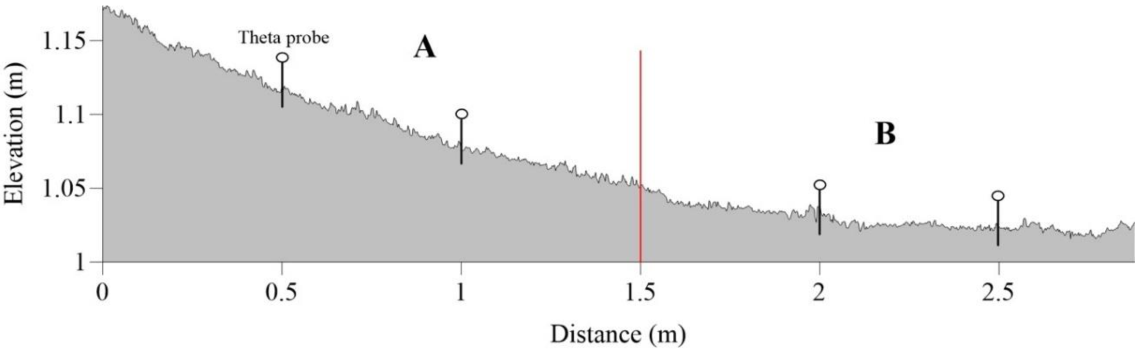

Fig. 1. Representative soil profile of the experimental plot determined from the DEM (see section 2.2.4) showing the changing slope gradient and the position of theta probe sensors along the ramp length for the 9% slope treatment. Area A: variable slope gradient (6% or 9%); Area B: constant slope gradient.

Water was supplied to the top of the flume using a weir maintained at a constant head. Two water flow rates were used (either 7 L min^{-1} or 12 L min^{-1}) for 30 minutes. This gave four slope-discharge treatments (Table 1) which were replicated in triplicate. To avoid edge effects, data from within 20 cm of the flume edges were ignored.

Table 1. Combinations between water flow rates and slope gradient used on experimental design.

Water flow rate (L min^{-1})	Variable slope (%)
7	6
	9
12	6
	9

2.2.2 Soil flume set-up

The plot was filled with a 40 cm layer of sand underneath 30 cm of soil (Fig. 2). The soil had 2.9% organic matter, a sandy loam texture with 5.1% clay, 43.6% silt and 51.3% sand. Soil aggregate size was standardized by sieving to 10 mm. The soil was added to the flume incrementally and compacted to a soil density of 1·3 g cm^{-3}. To maintain the same conditions for every experiment, the soil surface was moistened until it reached field capacity. To measure soil moisture, theta probe sensors were installed at depths of 0.07 m and 0.12 m, and at distances of 0·5 m, 1·0 m, 2·0 m and 2·5 m from the top of the plot (Figure 1). After each repetition, 5 cm of soil was removed from the surface layer and replaced with new soil compacted to the same initial density. To ensure the same subsurface conditions between slope angles, after each experimental run the subsoil was turned over, raked and replaced.

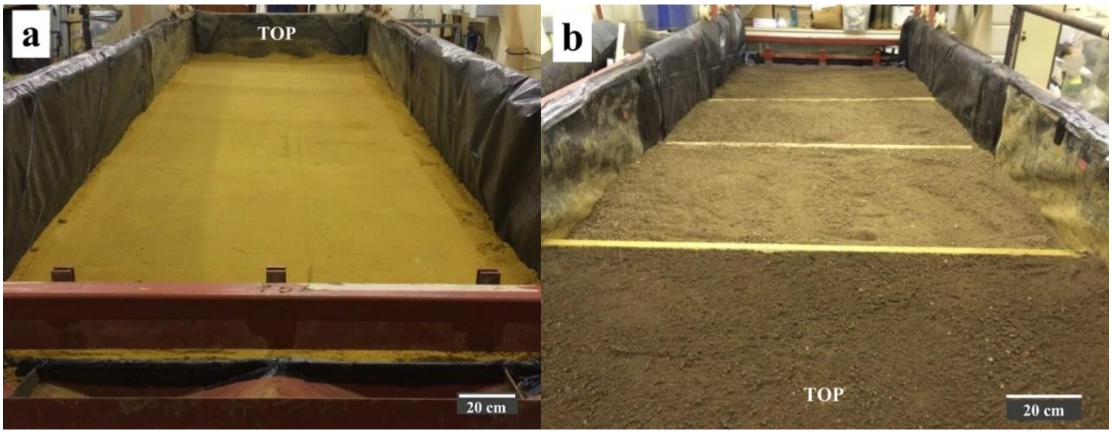

Fig. 2. Soil flume filled with layers of sand (a) followed by soil (b).

2.2.3 Design of image acquisition system

Time-lapse photography was used to study the development of rill erosion during runoff. Photographs were obtained before the water flow, during flow at time intervals of one minute between each image, and 30 minutes after the end of the experiment, which was the time required for drainage of excess water at the soil surface. The images were captured using six synchronised Canon digital SLR cameras (five EOS 450D and one Canon EOS 600D), with 28 mm fixed-focal lenses, located approximately 2·5 m above the soil surface. The EOS 450D features a 12 mega-pixel CMOS sensor of 22·2 × 14·8 mm (a pixel size of 5·2 μm) and delivered images of 4272 × 2848 pixels with a nominal ground sampling distance of 0.5 mm. The EOS 600D features an 18 mega-pixel CMOS sensor of 22·3 × 14·9 mm (a pixel size of 4·3 μm) and produced images of 5184 × 3456 pixels with a nominal ground sampling distance of 0.4 mm. Lens apertures were set to f/5·6 and, to maintain a fixed geometry during the experiment after focussing, focus control was set to manual and adhesive tape was used to lock the mechanisms. The cameras were arranged to produce three overlapping convergent stereo-pairs over the plot (Fig. 3) with synchronous image acquisition controlled by an intervalometer.

Fig. 3. Convergent stereo-pair cameras directed to the central portion of the plot for time-lapse monitoring of rill erosion during runoff.

2.2.3.1 Flow velocity

To calculate the flow velocity, after each experimental run, red dye was injected into the flow and photographs taken using an extra camera (Canon 500D, 15 mega-pixel, 22·3 × 14·9 mm CMOS sensor with 4·7 µm of pixel size, 4752 × 3168 pixels, and a zoom lens set to 18 mm, with aperture of f/5·6) at one image per second for 10 seconds: the time required for the runoff to reach the end of the plot (Figure 4).

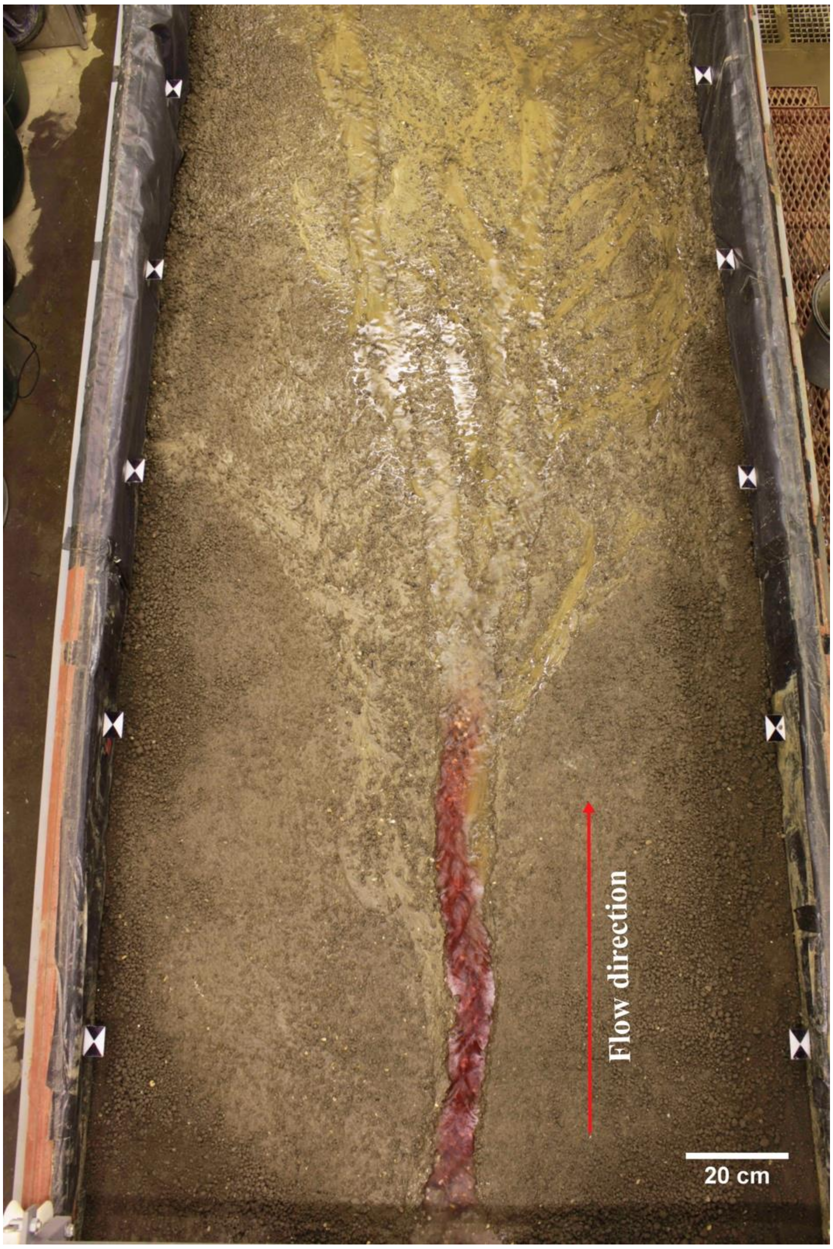

Fig. 4. Dye-pigmented water flow used as tracer for flow velocity calculations. At the sides of the experimental slope, photogrammetric control points for georeferencing the cloud of points can be seen.

2.2.4 Photogrammetric workflow

The structure-from-motion (SfM) photogrammetry technique was used to generate the three-dimensional (3D) point clouds. The images were processed using Agisoft Photoscan® v1·4 software, as already used in many studies (Nouwakpo et al., 2014; Piermattei et al., 2016; Di Stefano et al., 2017; Prosdocimi et al., 2017).

To generate the dense point cloud and then the digital elevation models, the first step was image alignment. In this step, all images were processed in order to detect the 2D location of matching tie point features in the images. For this process, Photoscan uses custom algorithms that are similar to the Lowe's (2004) Scale Invariant Feature Transform (SIFT). The next step calculates camera position and 3D location (X, Y and Z) of tie points by means of a bundle-adjustment algorithm. As a result of these first two steps, a sparse 3D point cloud was generated and then manually cleaned through removal of outliers to reduce reconstruction errors.

For georeferencing, 14 ground control points (GCP) were located around the plot (Fig. 4), with eight points used for control, and six as check points to estimate precision and accuracy of the 3D models through the computation of root-mean-square-error (RMSE). Also, the control points were used in the bundle adjustment, 'optimization' in Photoscan. This process removes non-linear distortions and minimises the total residual error on image observations by simultaneously adjusting camera parameters and orientations, and the 3D point positions (Granshaw, 1980). The point coordinates were established by total station (Trimble C3, accuracy 2 mm), within an arbitrary local coordinate system.

The third step uses the camera locations estimated previously, to produce a dense point cloud using multi-view reconstruction. The dense point clouds were exported into Surfer® software, converted to raster DEMs of 1-mm grid size using the Kriging interpolation method, and cropped to remove the flume edges. The photogrammetric parameters applied on Photoscan in the above-mentioned steps are listed in Table 2.

Table 2. Photoscan parameters settings used during the point cloud generation.

Point cloud: alignment parameters	Setting
Accuracy	Highest
Generic preselection	No
Reference preselection	No
Key point limit	0
Tie point limit	0
Filter point by mask	No
Dense point cloud: reconstruction parameters	
Quality	Ultra-high
Depth filtering	Mild

2.2.5 DEM of difference

DEMs of difference (DoD) were calculated to detect changes in the soil surface topography over time and to spatially quantify the volumes of sediment that were eroded and deposited. Georeferenced DEMs from different time periods were subtracted from each other to produce a raster of morphological change:

$$\mathrm{DoD} = \mathrm{DEM}_{t2} - \mathrm{DEM}_{t1} \qquad (1)$$

where *t1* is the initial time and *t2* is the consecutive time of DEM acquisition. Positive and negative values in the DoDs show deposition and erosion respectively.

2.2.6 DEM uncertainty

DEM uncertainty was assessed through the generation of precision estimates based on a Monte Carlo approach (James et al., 2017) with post-processing tools in sfm_georef software (James and Robson, 2012). This method consists of repeated bundle adjustments in Photoscan, in which different pseudo-random offsets are applied to the image observations and the control measurements to simulate observation measurement precision. Precision estimates for each optimised model parameter were then derived by characterising the variance for each particular parameter in the outputs from the large number of adjustments. In this study, 4,000 bundle adjustments were carried out, as used by James et al. (2017).

Precision maps were generated through the interpolation (1-mm grid size) of the vertical standard deviation (σ_Z) derived by the precision estimates, to enable precision estimates for both DEMs to be propagated into the DoD as vertical uncertainties (Taylor, 1997; Brasington et al., 2003; Lane et al., 2003; Wheaton et al., 2010). A spatially varying 'level of detection' (LoD) of significant elevation change was calculated for each DoD cell, according to the equation:

$$\mathrm{LoD} = t(\sigma_{Z1}^2 + \sigma_{Z2}^2)^{1/2} \qquad (2)$$

where σ_{Z1} and σ_{Z2} are the vertical precision estimates for each cell in the two DEMs and t is the t-distribution value defined by a specific confidence level (this study 95%, giving t = 1·96). Thus, changes smaller than the LoD can be disregarded, and Surfer was used to generate the LoD-thresholded DoD maps.

2.2.7 Rill development morphological indicators

The rills were classified manually in the DEMs. The morphological indicators chosen were total rill length (*RL*, m), mean rill width ($\overline{W}$, cm), mean rill depth ($\overline{D}$, cm), rill width-depth ratio (*WD*) and rill density (*RD*, m m^{-2}). The indicators were calculated according to the equations:

$$RL = \sum_{i=1}^{n} RLi \quad (3)$$

where RL_i is the i rill length (m), and n is the number of rills,

$$\overline{W} = \frac{\sum_{i=1}^{n} w_i}{n} \quad (4)$$

where w_i is the i rill width (cm),

$$\overline{D} = \frac{\sum_{i=1}^{n} D_i}{n} \quad (5)$$

where D_i is the i rill depth (cm), and

$$WD = \frac{\overline{W}}{\overline{D}} \quad (6).$$

Rill density is a measure of the rill erosion coverage in the area, being directly proportional to soil erosion and bifurcation ratio, and also reflect the degree of rill fragmentation (Shen et al., 2015).

$$RD = \frac{\sum_{i=1}^{n} RL}{A} \tag{7}$$

where A is the study area (m^2).

The erosion measurements were performed using the Simpson's rule method (see Easa, 1988), which assumes nonlinearity in the profile between grid points. This technique shows greater precision in the determination of volume compared to linear methods, such as the trapezoidal rule (Fawzy, 2015). The soil volume was converted to mass (kg) through soil bulk density.

Principal component analysis (PCA) was used to assess the relationship between morphological and quantitative indicators of rill erosion. Each variable was standardized to have mean zero and unity variance, to avoid the effects of differences in scales or magnitudes of the variables. The first two principal components were visualized in a PCA biplot to represent how the variables relate to one another and how the observations differ regarding to those variables.

2.3 Results

2.3.1 Precision results

The photogrammetric errors (RMSE) calculated by the Photoscan on x,y and z-axes for the control, check and tie points of each SfM point cloud are listed in Table 3. The point clouds show average errors of order ~1 mm on *xyz* on control and check points, whereas the tie points image residual RMS was ~ 0·3 pix.

Table 3. Root mean square error (RMSE) of check points, control points and tie points image residuals.

Water flow (L min^{-1})	Slope (%)	RMS tie points image residuals (pix)	RMSE of control points (mm)			RMSE of check points (mm)		
			X	Y	Z	X	Y	Z
7	6	0·35	0·872	0·468	1·323	0·775	1·742	0·592
		0·32	0·619	0·505	0·918	0·536	1·721	1·372
		0·28	0·651	0·832	0·876	0·291	0·301	0·419
	Average	**0·32**	**0·714**	**0·602**	**1·039**	**0·534**	**1·255**	**0·794**
	9	0·31	0·49	0·719	0·722	0·789	0·022	0·825
		0·27	0·668	0·624	0·572	0·378	0·084	0·424
	Average	**0·29**	**0·579**	**0·672**	**0·647**	**0·584**	**0·053**	**0·625**
12	6	0·32	0·604	0·981	0·616	0·408	0·841	0·752
		0·28	0·33	0·565	0·681	0·517	0·386	0·389
		0·31	1	0·887	0·77	1·052	0·533	0·89
	Average	**0·30**	**0·645**	**0·811**	**0·689**	**0·659**	**0·587**	**0·677**
	9	0·47	0·777	0·674	1·456	0·597	0·241	0·237
		0·36	0·804	0·728	0·673	0·679	0·092	0·682
		0·35	0·641	0·485	0·742	0·052	1·197	0·578
	Average	**0·39**	**0·741**	**0·629**	**0·957**	**0·443**	**0·510**	**0·499**

The precision maps show the spatial variation of precision along the flume (Fig. 5), with LoD values ranging from 1 mm to 2·8 mm. The smaller values were concentrated in the area around the centroid of control.

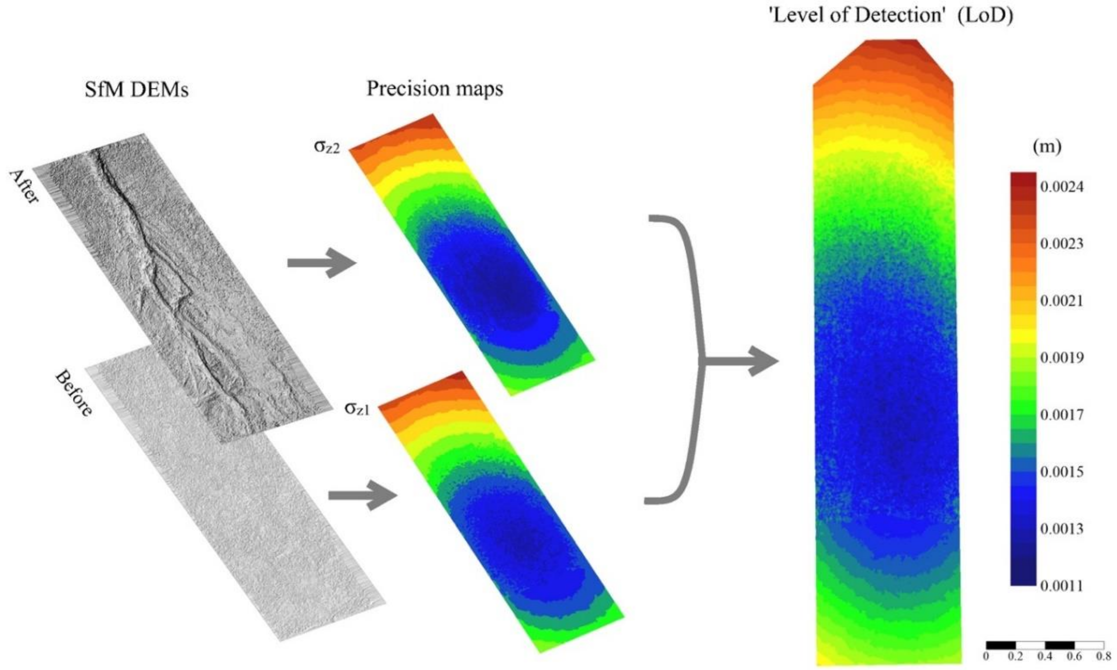

Fig. 5. Digital elevation models, precision maps and LoD showing the spatial distribution of the error along the flume. Changes with magnitudes smaller than the LoD can be disregarded.

2.3.2 DEM of Difference (DoD)

The DoD maps obtained for the flume (Figs. 6 and 7) show the different spatial behaviour of rill erosion due to changes in the slope and water flow rate. Both erosion (red), and deposition (blue) were detected. The treatments with 7 L min^{-1} of flow rate (Fig. 6) showed short and shallow rills, whereas the rills from 12 L min^{-1} of water flow rate were longer and deeper (Fig. 7).

The sediment depositional area corresponded with the gradient change for 7 L min^{-1} treatments, with rills on the steeper section of the flume and the depositional areas on the shallower section (Fig. 6). However, at 12 L min^{-1}, the water flow was able to transport the soil further past the gradient change, causing deposition at the bottom of the flume and higher rates of rill erosion.

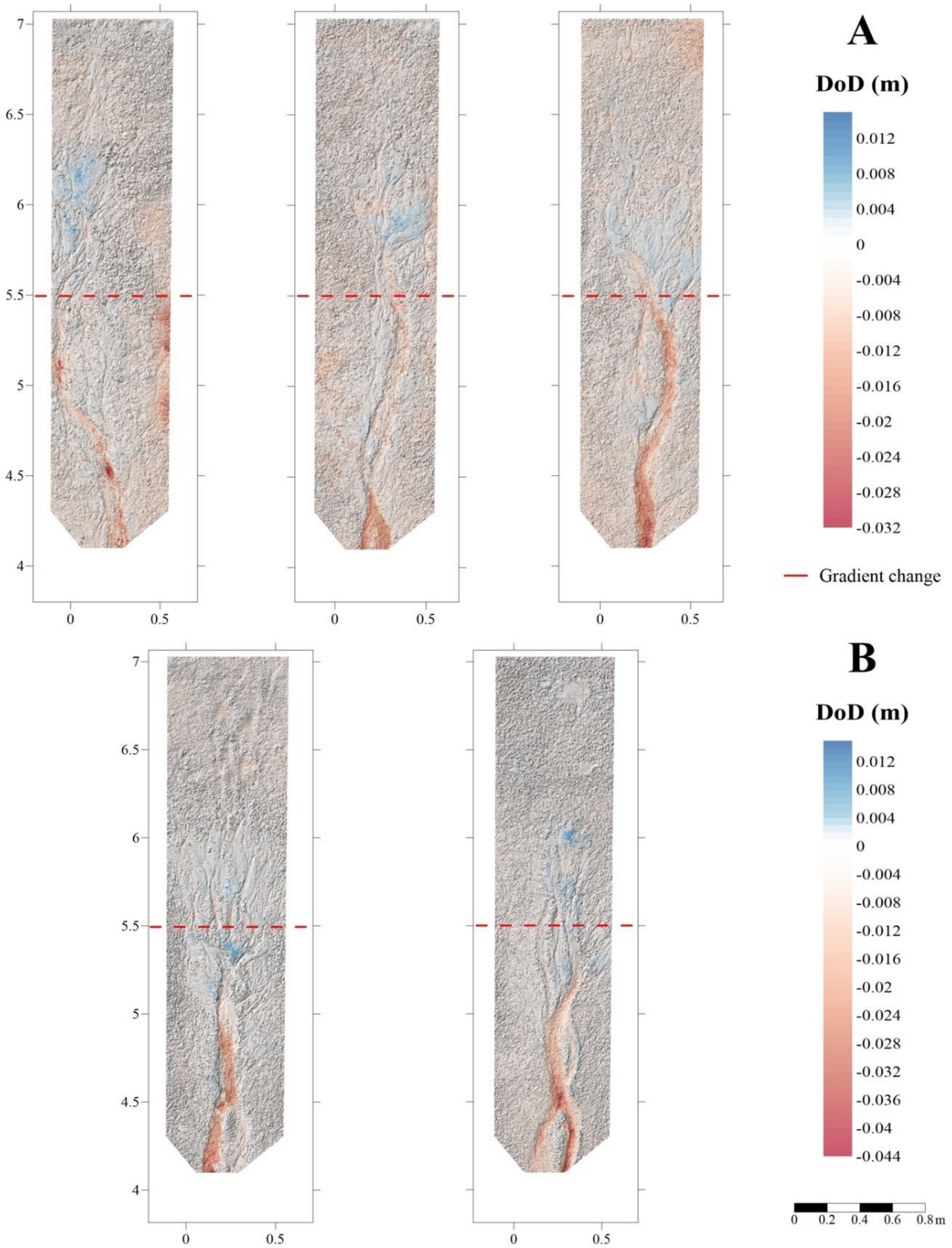

Fig. 6. DEM of difference (DoD) maps, overlain over hillshaded topography, showing rill erosion over runoff at 7 L min^{-1} of flow rate in two slopes, 6 % (A) and 9 % (B). Colour scale ranges from red (erosion) to blue (deposition).

Transparent regions mean no significant changes (DoD is less than the level of detection).

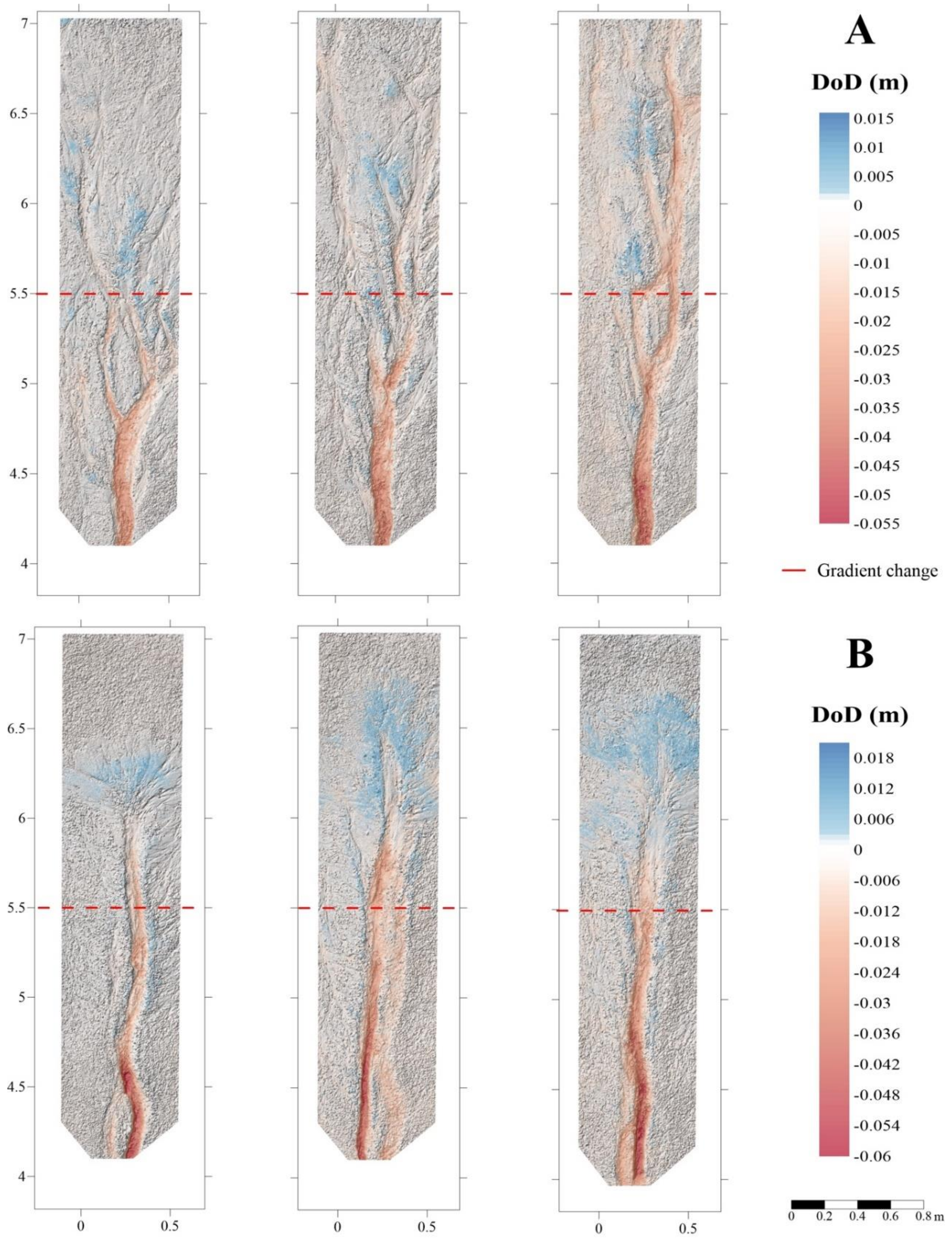

Fig. 7. DEM of difference (DoD) maps, overlain over hillshaded topography, showing rill erosion over runoff at 12 L min^{-1} of flow rate in two slopes, 6% (A)

and 9% (B). Colour scale ranges from red (erosion) to blue (deposition). Transparent regions mean no significant changes (DoD is less than the level of detection).

2.3.3 Rill erosion and soil loss

The rates of soil loss and rill erosion were greater at 12 L min^{-1} than at 7 L min^{-1} of water flow, regardless the slopes (Table 4). Increasing the water flow rate from 7 L min^{-1} to 12 L m^{-1} increased the amount of soil removed by rill erosion by about three times, on both slopes assessed. For the water flow rate of 7 L min^{-1}, the steeper-slope experiments showed greater values of soil erosion than the shallower-slope experiments, whereas for 12 L min^{-1} the amount of soil loss was about 1 kg m^{-2} greater at 6% than at 9% of slope. The proportion of rill erosion as a fraction of the total soil loss increased with the water flow and slope. However, the water flow rate contributed the most to the formation of rill erosion. In the treatments with 12 L min^{-1}, the rill erosion accounted for more than a half of the soil loss in the study area.

Table 4. Rill erosion and soil loss in different water flows and slopes.

Water flow (L min^{-1})	Slope (%)	Rill erosion (kg m^{-2})	Soil loss (kg m^{-2})	Proportion of soil loss due to rill erosion (%)
7	6	0·58 d	2·32 d	25·1
	9	0·94 c	2·77 c	33·9
12	6	2·42 b	4·12 a	58·8
	9	3·05 a	3·72 b	82·0

Means in a column followed by the same letter are not significantly different from one another ($\alpha = 0{\cdot}05$) according to the Tukey test.

2.3.4 Rill morphology

Total rill length increased with an increase slope at 7 L min^{-1}, but at 12 L min^{-1}, the slope had an opposite effect on rill length (Fig. 8). The total rill length on 12 L min^{-1} at 6% of slope was 2.1 times longer than the 9% slope. Otherwise, the main rill length was longer on low slopes for both water flow rates (Fig. 8).

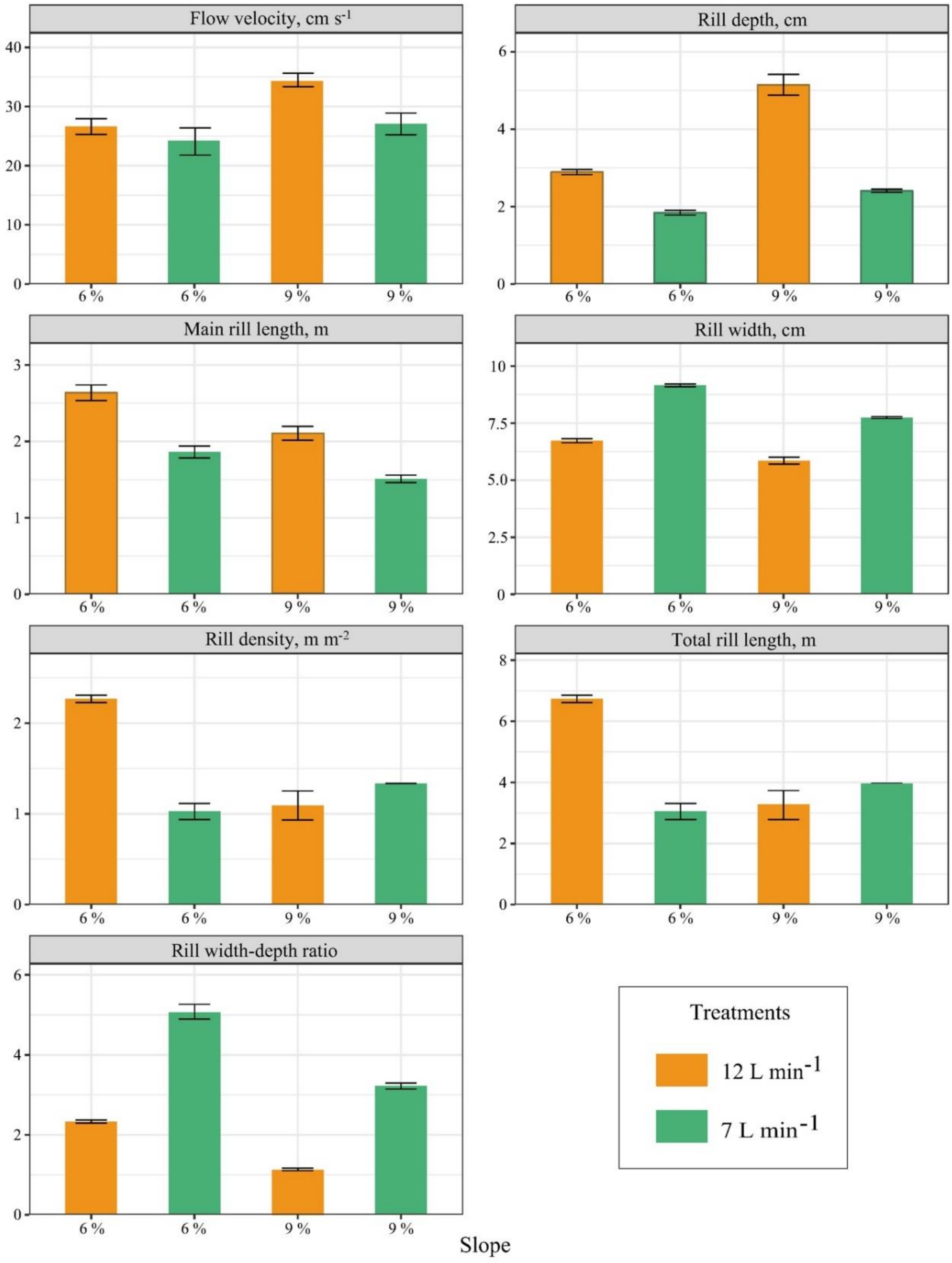

Fig. 8. Rill erosion characteristics and morphological parameters under different water flow and slope gradients. Error bars represent the standard error of the mean (*n* = 3).

The mean rill depth showed a positive relationship with the water flow rate and slope. On the other hand, the rills were wider on low flow rates and slopes, with the 7 L min^{-1} at 6% slope showing the widest rill among the treatments studied (Fig. 9). This is reflected in the behaviour of the rill width-depth ratio (WD). Taking the WD ratio value for 12 L min^{-1} flow rate as the example, at 9% slope the WD ratio was approximately four times lower than the 7 L min^{-1} flow rate at 6% slope.

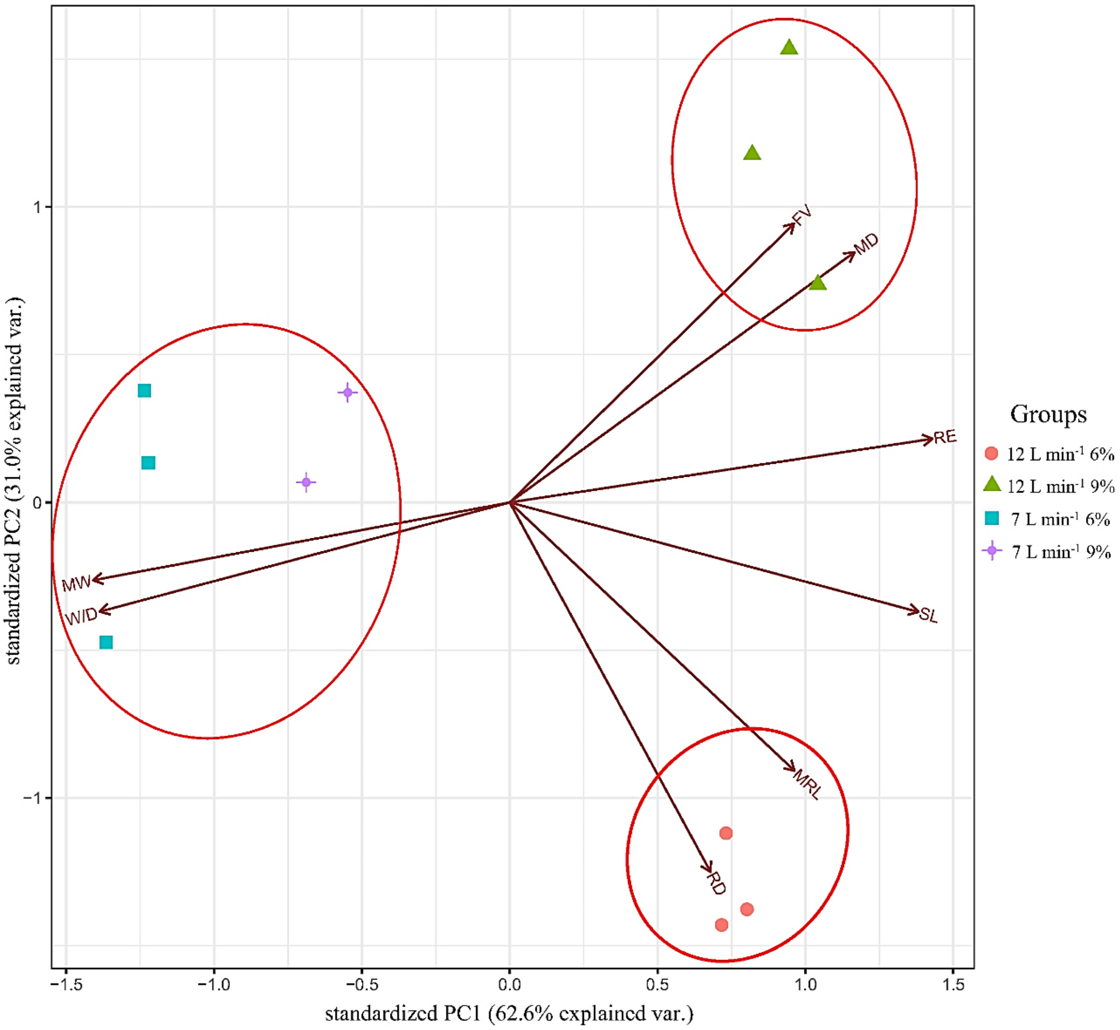

Fig. 9. Principal component analysis (PCA) for the morphological and quantitative indicators of rill erosion in flows of 7 and 12 L m^{-1} and slopes of 6% and 9%. FV: flow velocity; RD: rill density; MD: mean rill depth; MRL: main rill length; MW: mean rill width; WD: width-depth ratio; RE: rill erosion; SL: soil loss.

The flow velocity (FV) for 7 L min^{-1} flow rate did not show a significant difference between slopes of 6% and 9%. On the other hand, the FV increased by 1·28 times with the increase of slope for 12 L min^{-1} flow rate. At 6% the change in water flow rate did not affect the FV, whereas, when considering 9 % slope, the increase from 7 L min^{-1} to 12 L min^{-1} increased the FV by 1·32 times.

The rill density showed a different behaviour according to the rate of the water flow. For 7 L min^{-1}, the rill density increased with the increase of slope. However, for 12 L min^{-1}, the density of rills in the area decreased when the slope increased, being 2·08 times higher in 12 L min^{-1} at 6% than at 9% slope.

2.4 Discussion

2.4.1 Rill network development

In this study we introduce the use of close-range photogrammetry to study the rill network development with millimetric accuracy, allowing the extraction of rills and parameter calculations (i.e. rill width, depth, length) by applying image processing methods. The spatial distribution of the rills (Figs. 6 and 7) shows that the highest rates of soil erosion were at the top of the plot, with erosion decreasing down-slope. This occurs mainly because of the gradient change, with slope decreasing and becoming constant at the bottom of the soil flume. In addition, the clean water at the top of the rills has the maximum soil detachment potential (Nearing et al., 1989; Chen et al., 2014). Also, as the concentration of the sediments on the water flow increases along the rills, the soil detachment capability continues to decrease, due to the energy being used by the transportation of soil particles (Chen et al., 2016).

Table 4 shows that the amount of soil eroded by rill erosion increased with flow rates and slope gradients. The increase in the slope gradient also promotes an increase of the velocity and energy of concentrated flow (Li et al., 2005). Similar results were founded by Chen et al. (2016) and Kinnell (2000).

Furthermore, another parameter that influenced rill erosion was FV, which has an important role in rill development and soil erosion. When the flow rate was at its highest level (12 L min^{-1}) the increase in slope gradient increased the FV, leading to a greater eroding force. Thus, higher FV values imply the generation of deeper rills, because it is easier for the water to erode an existing rill than create another one (Mancilla et al., 2005). Then, the rill erosion intensity was closely associated with the FV in the area.

The slope gradient change along the plot showed clearly that the sediment transport capacity was directly related to changes in flow velocity (Lei et al., 1998). For the two different discharges, sediment deposition was different in the 2% slope area. For the 7 L min^{-1}, the transported sediments were deposited in thin layers at the boundary between the area of the higher and shallower slope. However, for the 12 L min^{-1} flow rate, deposition was concentrated towards the bottom of the rills, further into the lower slope area. This reflects the greater distance required for the flow energy to fall to the point at which deposition occurs.

2.4.2 Soil loss due to rill erosion

The proportion of soil loss due to rill erosion was directly affected by the increase of slope and water flow rate. Studies show that the increase of slope gradient also increase the collapse of rill heads and sidewalls, accounting for > 90 % of rill erosion (Xiao et al., 2016), which can lead to a greater contribution to total soil loss (Jiang et al., 2018; Wang and Shi, 2015). Zheng et al. (1987) and Shen et al. (2015), also observed that rill erosion accounted for up to 74·2 % and 86·7 % of soil losses, respectively.

Contrary to expectations, for the 12 L min^{-1} flow rate experiments, the increase of slope gradient did not coincide with an increase in soil loss. This can be explained by the higher bifurcation showed for 6% slopes in contrast with for 9% slopes (Fig. 7). On steeper slopes, the rill network pattern comprises deep rills with fewer secondary channels, whereas at 6% slope, the rills were shallower and with high values of rill density, producing greater total soil losses but smaller rill erosion rates (Fig. 9).

When comparing different types of soil erosion, rill erosion generates greater soil losses than other types of soil erosion (sheet and splash erosion) (Shen et al., 2015). Thus, once rill erosion is initiated and became the main erosion pattern, the rate of soil loss increases very rapidly (Kimaro et al., 2008; He et al., 2016).

2.4.3 Rill network morphology

As the flow velocity increase, the rills became deeper and narrow (Fig. 9). Mean rill width decreased when the slope gradient increased, regardless of the water flow rate, while the mean rill depth increased with increasing slope. Similar results were founded by Lei and Nearing (2000) and He et al. (2016). This behaviour can be explained by the increase in eroding force and erosion intensity promoted by the high stream power on high slopes (Chen et al., 2016).

Rill density values reflected the rill fragmentation (Figs. 6 and 7) and were related to the main rill length (Fig. 9). The highest values of rill density were for 12 L min^{-1} at 6 % of slope. On the other hand, the rill density was statistically the same for 7 L min^{-1} at 6% and 12 L min^{-1} at 9% of slope. This means that high water flow, combined with high slope gradient can generate substantial amounts of soil loss in non-complex rill network. Thus, the amount of rill erosion is primarily related to the depth and flow velocity than the rill network density.

2.5 Conclusions

In this study, a runoff simulator was used to investigate the influence of different slopes and water flow on the behaviour of soil erosion and sediment transport. The gradient change had a great influence on the rill erosion behaviour along the slope, with the highest soil erosion rates being concentrated in the upper part of the plot. The gradient change also resulted in different patterns of rill network, reducing depth and promoting soil sedimentation. The flow velocity in rills increased with water flow and slope, showing a strong correlation with the amount of rill erosion. The rills produced at a lower water flow rate (7 L min^{-1}) were wider, with width-depth ratio almost 5 times greater at 6% slope than at 12 L min^{-1} at 9% of slope.

The greatest amount of soil loss and rill density was found for 12 L min^{-1} on a 6% slope, whereas the greatest rill erosion was on 12 L min^{-1} at 9% of slope. These results demonstrate that on steep slopes the soil erosion is dominated by the rill erosion with less rill network density while, on low slopes, there are other types of soil erosion occurring together with rill erosion, causing the reduction of soil loss due to rill erosion.

Despite the known effects of vegetation cover on erosion reduction and sediment production, this work did not evaluate treatments with vegetation on the surface. Obtaining high-resolution DEMs through SfM in vegetated areas requires further processing, using mathematical algorithms to classify and filter the point cloud in vegetated and non-vegetated areas. Thus, the accuracy of DEMs obtained by SfM in areas with vegetation cover is compromised, as well as volumetric measurements in these regions. The use of SfM to study the morphology and development of the furrow network in vegetated areas is still a challenge.

2.6 References

Abd Elbasit, M.A.M., Anyoji, H., Yasuda, H., Yanamoto, S., 2009. Potential of low cost close-range photogrammetry system in soil microtopography quantification. Hydrol. Process. 23, 1408–1417.

Aguilar, M.A., Aguilar, F.J., Negreiros, J., 2009. Off-the-shelf laser scanning and close-range digital photogrammetry for measuring agricultural soils microrelief. Biosyst. Eng. 103, 504–517.

Armstrong, A., Quinton, J.N., Heng, B.C.P., Chadler, J.H., 2011. Variability of interrill erosion at low slopes. Earth Surf. Process. Landforms 36, 97-106.

Bewket, W., Sterk, G., 2003. Assessment of soil erosion in cultivated fields using a survey methodology for rills in the Chemoga watershed, Ethiopia. Agric. Ecosyst. Environ. 97, 81–93.

Brasington, J., Langham, J., Rumsby, B., 2003. Methodological sensitivity of morphometric estimates of coarse fluvial sediment transport. Geomorphology 53, 299–316.

Brodu, N., Lague, D., 2012. 3D terrestrial Lidar data classification of complex natural scenes using a multi-scale dimensionality criterion: applications in geomorphology. ISPRS J. Photogramm. Remote Sens. 68, 121–134

Chen, X.Y., Zhao, Y., Mo, B., Mi, H.X., 2014. An improved experimental method for simulating erosion processes by concentrated channel flow. Plos One 9 (6), e99660.

Chen, X.Y., Zhao, Y., Mi, H., Mo, B., 2016. Estimating rill erosion process from eroded morphology in flume experiments by volume replacement method. Catena 136, 135-140.

Di Stefano, C., Ferro, V., Palmeri, V., Pampalone, V., 2017. Measuring rill erosion using structure from motion: A plot experiment. Catena 156, 383-392.

Easa, S.M., 1988. Estimating pit excavation volume using nonlinear ground profile. J. Surv. Eng. 114, 71–83.

Eltner, A., Maas, H-G., Faust, D., 2018. Soil micro-topography change detection at hillslopes in fragile Mediterranean landscapes. Geoderma 313, 217-232.

Favis-Mortlock, D.T., Boardman, J., Parsons, A.J., Lascelles, B., 2000. Emergence and erosion: a model for rill initiation and development. Hydrol. Process. 14, 2173–2205.

Fawzy, H.E-D., 2015. The accuracy of determining the volumes using close range photogrammetry. J. Mech. Civ. Eng. 12, 10–15.

Gatto, L.W., 2000. Soil freeze–thaw-induced changes to a simulated rill: potential impacts on soil erosion. Geomorphology 32, 147–160.

Gessesse, G.D., Fuchs, H., Mansberger, R., Klik, A., Rieke-Zapp, D.H., 2010. Assessment of erosion, deposition and rill development on irregular soil surfaces using close range digital photogrammetry. Photogramm. Rec. 25, 299–318.

Govers, G., Poesen, J., 1988. Assessment of the interrill and rill contributions to total soil loss form an upland field plot. Geomorphology 1, 343–354.

Guo, M., Shi, H., Zhao, J., Liu, P., Welbourne, D., Lin, Q., 2016. Digital close range photogrammetry for the study of rill development at flume scale. Catena 143, 265–274.

Granshaw, S.I., 1980. Bundle adjustment methods in engineering photogrammetry. Photogramm. Rec. 10 (56), 181–207.

He, J.J., Sun, L.Y., Gong, H.L., Cai, Q.G., Jia, L.J., 2016. The characteristics of rill development and their effects on runoff and sediment yield under different slope gradients. J. Mt. Sci. 13, 397–404.

Heng, B.C.P., Chandler, J.H., Armstrong, A., 2010. Applying close-range digital photogrammetry and soil erosion studies. The Photogrammetric Record 25, 240–265.

Jackson, J.A., 1997. Glossary of Geology. American Geological Institute, Alexandria.

James, M.R., Robson, S., 2012. Straightforward reconstruction of 3D surfaces and topography with a camera: Accuracy and geoscience application. J. Geophys. Res. 117, F03017.

James, M.R., Robson, S., Smith, M.W., 2017. 3-D uncertainty-based topographic change detection with structure-from-motion photogrammetry: precision maps for ground control and directly georeferenced surveys. Earth Surf. Process. Landforms 42, 1769-1788.

Jiang, F., Zhan, Z., Chen, J., Lin, J., Wang, M.K., Ge, H., Huang, Y., 2018. Rill erosion processes on a steep colluvial deposit slope under heavy rainfall in flume experiments with artificial rain. Catena 169, 46-58.

Kimaro, D.N., Poesen, J., Msanya, B.M., Deckers, J.A., 2008. Magnitude of soil erosion on the northern slope of the Uluguru Mountains, Tanzania: interrill and rill erosion. Catena 75, 38–44.

Kinnell, P.I.A., 2000. The effect of slope length on sediment concentrations associated with side-slope erosion. Soil Sci. Soc. Am. J. 64, 1004–1008.

Lane, S., Westaway, R., Murray Hicks, D., 2003. Estimation of erosion and deposition volumes in a large, gravel-bed, Braided River using synoptic remote sensing. Earth Surf. Process. Landf. 28, 249–271.

Lei, T.W., Nearing, M.A., 1998. Rill erosion and morphological evolution: a simulation model. Water Resour. Res. 34, 3157–3168.

Lei T.W., Nearing, M.A., 2000. Flume experiments for determining rill hydraulic characteristic erosion and rill patterns. J. Hydraul. Eng. 31, 49-55.

Lei, T.W., Nearing, M.A., Haghighi, K., 1998. Rill erosion and morphological evolution: a simulation model. Water Resour. Res. 34, 3157–3168.

Li, P., Li, Z.B., Zheng, L.Y., Lu, K.X., 2005. Comparisons of dynamic mechanics of soil erosion and sediment yield by runoff on loess slope. Soil Water Conserv. 19, 66–69.

Lisein, J., Linchant, J., Lejeune, P., Bouché, P., Vermeulen, C., 2013. Aerial surveys using an unmanned aerial system (UAS): comparison of different methods for estimating the surface area of sampling strips. Trop. Conserv. Sci. 6, 506–520.

Lowe D.G., 2004. Distinctive image features from scale-invariant keypoints. Int. J. Comput. Vis. 60, 91–110.

Mancilla, G.A., Chen, S., McCool, D.K., 2005. Rill density prediction and flow velocity distributions on agricultural areas in the Pacific Northwest. Soil Tillage Res. 84, 54–66.

distributions on agricultural areas in the Pacific Northwest. Soil Tillage Res. 84, 54–66

Morgan, R.P.C., 1977. Soil Erosion in the United Kingdom: Field studies in the Silsoe area, 1973–1975. Occasional Paper. 4 Nat. Coll. Agr. Eng. Silsoe, UK.

Morgan, R.P.C., 2005. Soil Erosion and Conservation. third ed. Blackwell Publishing Ltd., Cornwall.

Nearing, M.A., Foster, G.R., Lane, L.J., 1989. A process based soil erosion model for USDA Water Erosion Prediction Project Technology. Trans. ASAE 32, 1587–1593.

Nearing, M.A., Norton, L.D., Bulgakov, D.A., Larionov, G.A., West, L.T., Dontsova, K.M., 1997. Hydraulics and erosion in eroding rill. Water Resour. Res. 33, 865–876.

Nouwakpo, S.K., Huang, C.-H., 2012. A simplified close-range photogrammetric technique for soil erosion assessment. Soil Sci. Soc. Am. J. 76, 70–84.

Nouwakpo, S.K., James, M.R., Weltz, M.A., Huang, C.-H., Chagas, I., Lima, L., 2014. Evaluation of structure from motion for soil microtopography measurement. Photogramm. Rec. 29, 297–316.

Piermattei, L., Carturan, L., de Blasi, F., Tarolli, P., Dalla Fontana, G., Vettore, A., Pfeifer, N., 2016. Suitability of ground-based SfM–MVS for monitoring glacial and periglacial processes. Earth Surf. Dyn. 4, 425–443.

Poesen, J., Nachtergaele, J., Verstraeten, G., Valentin, C., 2003. Gully erosion and environmental change: importance and research needs. Catena 50, 91–133.

Prosdocimi, M., Burguet, M., Di Prima, S., Sofia, G., Terol, E., Rodrigo Comino, J., Cerdá, A., Tarolli, P., 2017. Rainfall simulation and structure-from-motion photogrammetry for the analysis of soil water erosion in Mediterranean vineyards. Sci. Total Environ. 574, 204–215.

Rieke-Zapp, D.H., Nearing, M.A., 2005. Digital close range photogrammetry for measurement of soil erosion. Photogramm. Rec. 20, 69–87.

Robertson, D.P., Cipolla, R., 2009. Structure from motion. In: Varga, M. (Ed.), Practical Image Processing and Computer Vision. John Wiley & Sons, Chichester.

Shen, H., Zheng, F., Wen, L., Han, Y., Hu, W., 2016. Impacts of rainfall intensity and slope gradient on rill erosion processes at loessial hillslope. Soil Tillage Res. 155, 429-436.

Shen, H.O., Zheng, F.L., Wen, L.L., Lu, J., Jiang, Y.L., 2015. An experimental study of rill erosion and morphology. Geomorphology 231, 193–201.

Taylor, J.R., 1997. An Introduction to Error Analysis: the Study of Uncertainties in Physical Measurements, second edition. University Science Books: Sausalito, California.

Wang, L., Shi, Z.H., 2015. Size selectivity of eroded sediment associated with soil texture on steep slopes. Soil Sci. Soc. Am. J. 79, 917–929.

Wheaton, J., Brasington, J., Darby, S., Sear, D., 2010. Accounting for uncertainty in DEMs from repeat topographic surveys: improved sediment budgets. Earth Surf. Process. Landf. 35, 136–156.

Wirtz, S., Seeger, M., Ries, J.B., 2012. Field experiments for understanding and quantification of rill erosion processes. Catena 91, 21–34.

Xiao, H., Liu, G., Liu, P.L., 2016. Response of detachment rate of loess slope to hydrodynamic characteristics under concentrate flow condition. Trans. CSAE 32, 106–111 (in Chinese with English abstract).

Zhang, W., Qi, J., Wan, P., Wang, H., Xie, D., Wang, X., Yan, G., 2016. An Easy-to-Use Airborne LiDAR Data Filtering Method Based on Cloth Simulation. Remote Sens. 8, 501.

Zheng, F.L., Tang, K.L., Zhou, P.H., 1987. Approach to the genesis and development of rill erosion on slope land and the way to control. J. Soil Water Conserv. 1, 36–48 (in Chinese, with English Abstract).

3. High resolution monitoring of sheet (interrill) erosion using structure-from-motion

3.1 Introduction

Soil erosion is one of the main factors that lead to the degradation of agricultural land worldwide (Boardman et al., 2003; Bakker et al., 2004; Zhao et al., 2019). It threats agricultural sustainability by reducing the water retention capacity, the nutrient content, and total organic carbon of the soil (Quinton et al., 2010; Zhao et al., 2016), causing pollution of water bodies (Lal, 1998). Thus, the accurate measurement of erosion rates becomes a key factor for better understanding the erosive process in different scenarios and to promote efficient recovery strategies aiming to reduce soil loss in sloping areas (Cerdan et al., 2010; Di Stefano and Ferro, 2017).

In the last decades, soil erosion has been studied primarily from plots of soil loss under natural and artificial rainfall conditions (Araya et al., 2011; García-Ruiz et al., 2015; Guo et al., 2015; Fang et al., 2017; Zhao et al., 2019). However, soil erosion data acquired from traditional methods is considered a time-consuming and costly process (Cerdan et al., 2010). Recently, with the technological advances, digital elevation models (DEM) produced from high-resolution surveying techniques have played an important role in the understanding of geomorphological processes. These advances have been facilitated by the development of Structure-from-Motion (SfM; Ullman, 1979), a technique that combines well-established photogrammetric principles with modern computational methods (Westoby et al., 2012).

SfM photogrammetry, using images acquired from unmanned aerial vehicle (UAV), is being adopted for the generation of high-resolution DEMs in studies of surface processes (Colomina and Molina, 2014). The use of UAVs have made the acquisition of aerial photographs cheap and easy, allowing surveys at high temporal and spatial resolution. This makes it possible to monitor and quantify rapidly changing landscapes (Cook, 2017).

In geosciences, the application of photogrammetry using SfM is now considered an established method to describe high-resolution topography (Cook, 2017; Eltner et al., 2018). This technique has been used in several Earth surface surveys, in studies of fluvial, glacial, and coastal geomorphological processes (Dietrich, 2016; Westoby et al., 2016; Warrick et al., 2017), as well as in the monitoring and quantification of soil erosion volumes in gullies (Castillo et al., 2012; Gómez- Gutiérrez et al., 2014; Stöcker et al., 2015, Glendell et al., 2017).

However, photogrammetry applications from SfM with the use of UAVs in studies of soil erosion where there are no large mass movements and gullies are still scarce. This is due to difficulties in defining a stable coordinate reference system, which is important for quantifying changes of small magnitudes that are typical of laminar erosion processes. There are studies involving SfM and UAVs that quantify erosion at large magnitudes (Bazzoffi, 2015, Neugirg et al., 2016); however, the evaluation of sheet erosion under natural rainfall is still limited

(Eltner et al., 2015; Nouwakpo et al., 2015, Hänsel et al., 2016, Morgan et al., 2017; Prosdocimi et al., 2017).

The assessment of the accuracy of data derived from SfM has been carried out by several studies (James and Robson, 2012; Westoby et al., 2012; Gómez-Gutiérrez et al., 2014; Eltner et al., 2015; Cook et al., 2017; James et al., 2017a; Morgan et al., 2017) using aerial and terrestrial laser scanning or control points with high precision as a reference. The reported accuracies vary widely from sub-decimetre to more than 1 m, reflecting the dependence of SfM accuracy on the image quality, distortion and orientation, vegetation presence, soil surface characteristics, number and precision of the ground control points and scale.

The SfM relative precision ratio (measurement precision: observation distance) is limited by the model used for camera calibration in software, but generally exceed 1:1000, which implies the accuracy of centimetres over distances of 10s of metres. (James and Robson, 2012). Comparative studies have shown that SfM generates topographic data with quality, resolution and accuracy similar to those obtained by laser scanning and classical photogrammetry surveys (Westoby et al., 2012; Fonstad et al., 2013; Mancini et al., 2013; Stumpf et al., 2013; White et al., 2013; James and Quinton, 2014; Ouédraogo et al., 2014; Cook, 2017).

Repeated topographic surveys of the same area are often carried out in order to establish spatial patterns of erosion, deposition, and changes in volume. Therefore, when successive DEMs are subtracted from each other, the DEM of difference (DoD) can be generated, highlighting areas of erosion and deposition (Lane et al., 2003). However, there are no studies that validate such volume measurements conducted by UAVs through SfM and DoD through comparison with measurements of sediment collected in standard erosion plots.

The speed of data acquisition from UAVs, coupled with the high precision of the DEMs generated by the SfM can be important tools in obtaining soil loss values that are used in modelling water erosion. Thus, this study aims to evaluate the efficacy of SfM in obtaining sub-centimetre level precision measurements of soil loss in areas of sheet erosion under natural rainfall in standard plots of soil loss where there are no large furrows or gullies.

3.2 Materials and Methods

3.2.1 Experimental area

All the experiments were conducted on the campus of the Federal University of Lavras, Lavras, Brazil (21º13'20'' S and 44º58'17'' W), during two hydrological years. The area presents a typical humid subtropical climate, with an annual average rainfall of 1,530 mm. The soil is classified as an Inceptisol, according to the US Soil Taxonomy, with 47·8% sand, 15·8% silt and 36·4% clay, presenting a density of 1,400 kg m^{-3}. Three plots (12 m × 4 m) were installed in the area to monitor soil erosion on a 23% slope, under bare soil and natural rainfall (Fig. 1). The longest dimension of the plot followed the direction of the slope.

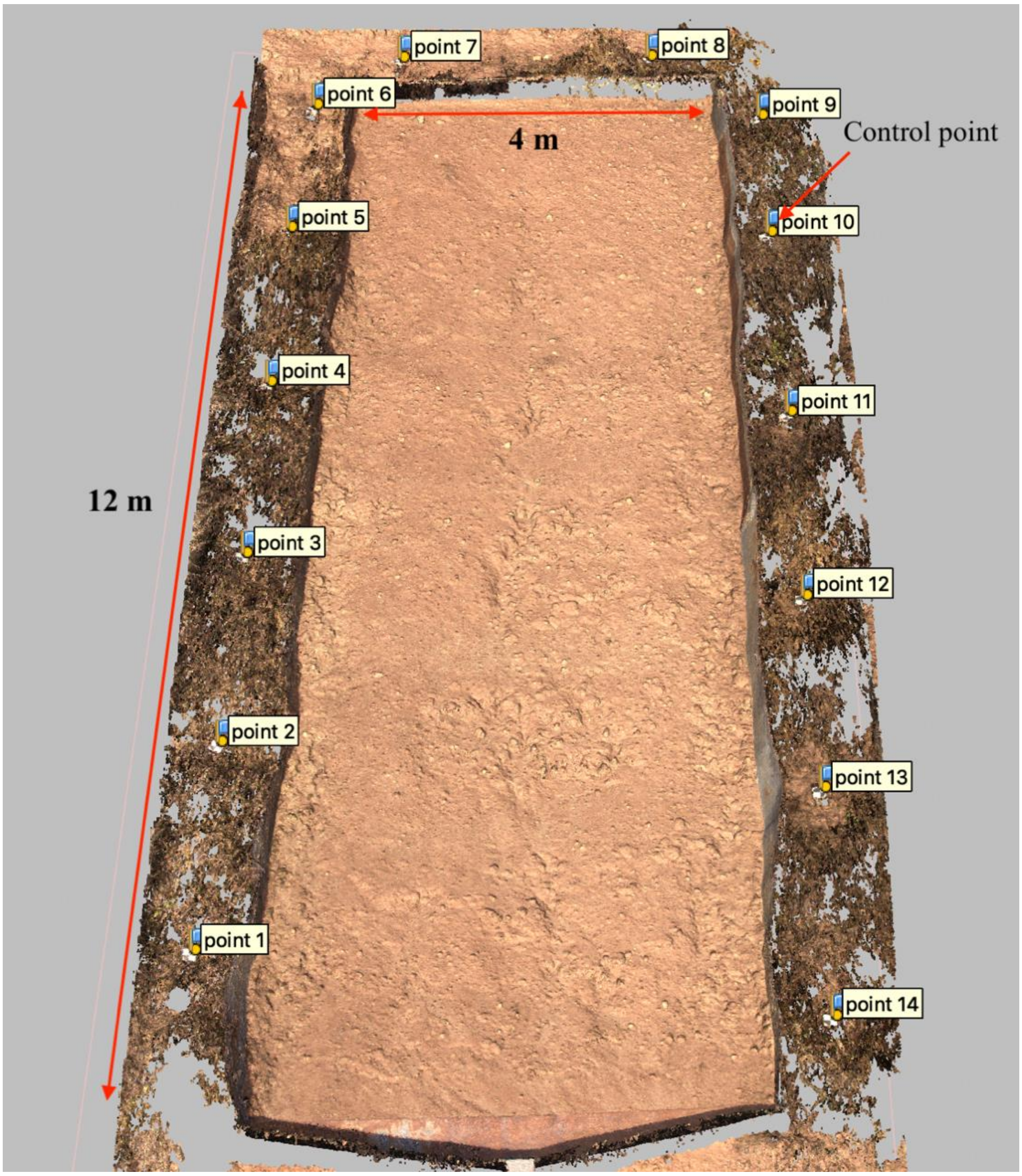

Fig. 1. Typical erosion plot showing dimensions and control point layout.

3.2.2 Sediments measurements on erosion plots

The collector system comprised two tanks installed in sequence, the first with 500 L capacity and the second 250 L (Fig. 2). Among the sedimentation tanks there was a Geib divisor system with 15 windows so that after filling the first tank, only 1/15 of the runoff was conducted to the second tank.

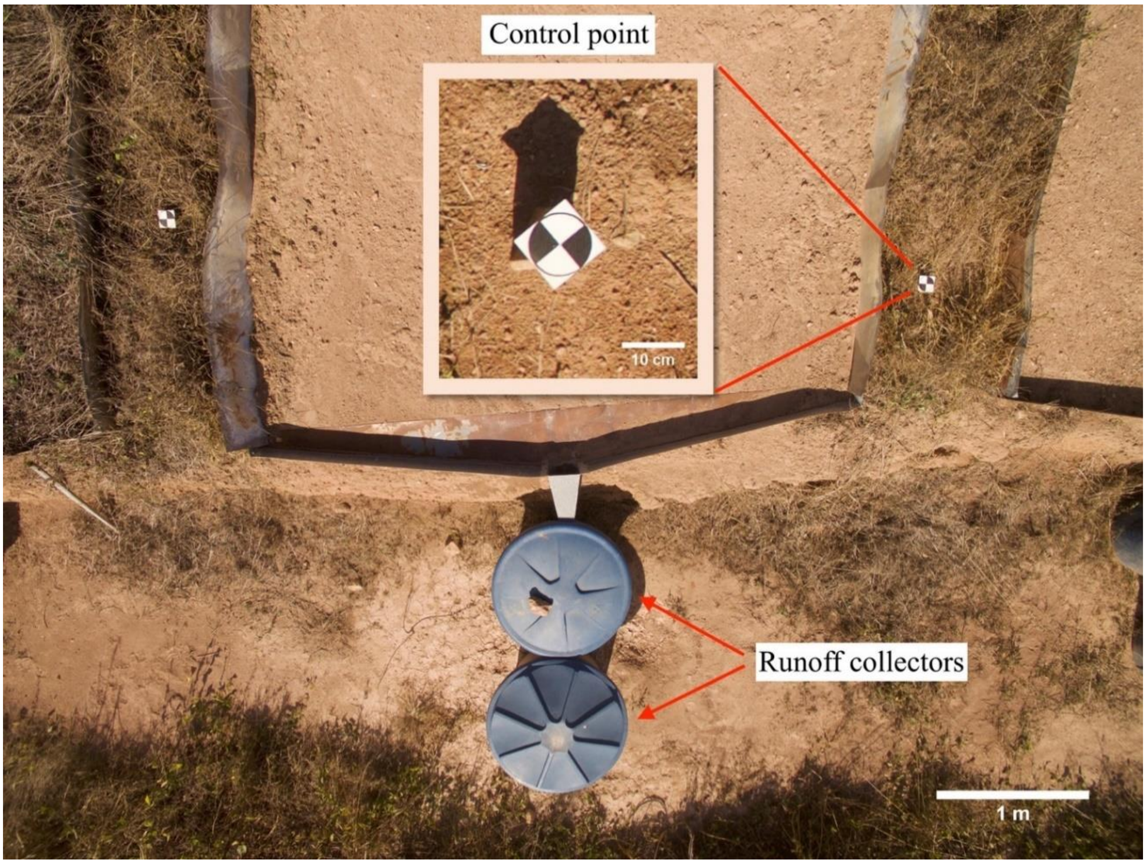

Fig. 2. Runoff collection system used on soil loss plots. Inset shows the detail of a ground control point.

To quantify soil losses, runoff samples and sediments were collected from the collection tanks. After stirring, three aliquots of predetermined volume were collected, transferred to the laboratory, the supernatant decanted and the remaining sediment dried at 105°C before weighing.

3.2.3 Image acquisition

A UAV, DJI Phantom 3 Professional, was used for data acquisition. The UAV features integrated a gimbal-stabilized FC300X camera with 12-megapixel (4000 × 3000) Sony EXMOR 1/2·3 sensor, 94º field of view (FOV) and 20-mm focal length. The lens aperture was set to f/2·8 and images acquired in RAW format.

Seven flights were performed on each erosion plot, from June 2016 to April 2018. The flights were conducted manually using a combination of orthogonal and oblique photos to provide convergent image geometries between the lines (James et al., 2014). In order to reduce the influence of direct sunlight at noon, flights were conducted either in the morning or in the afternoon on cloudy days. Flight heights were over 4 m with a nominal ground sampling distance of 1·5 mm. A total of 35 photos were taken in each survey, with 70% of forward and side overlap.

For georeferencing, 14 ground control points (GCP) were installed around the plots (Fig. 1), with ten points used for control and four as check points to estimate the precision and the accuracy of the 3D models by calculating the root mean square error (RMSE). The coordinates of the points were established by total station (Geodetic GD2i, accuracy 2 mm), within an arbitrary local coordinate system.

3.2.4 Structure from motion (SfM) point cloud generation

The generation of three-dimensional point clouds (3D) was performed using the SfM photogrammetry technique, which allows the reconstruction of the topography from randomly distributed and oriented images from uncalibrated cameras (James and Robson, 2012; Fonstad et al., 2013; Agüera-Vega et al. 2018). The images were processed using the commercially available SfM software Agisoft Photoscan Professional® v1.4, which have been used for several studies

(Brunier et al., 2016; Di Stefano et al., 2017; Prosdocimi et al., 2017). All processing was done through cloud computing using a virtual machine (24 Intel Xeon Platinum 3.7 GHz CPUs, two NVIDIA Tesla K80 GPUs and 128 GB RAM).

Firstly, image alignment was done to generate the dense point cloud and then the DEMs. In this step, all images were processed in order to detect the 2D location of matching tie point features in the images. For this process, Photoscan uses custom algorithms that are similar to the Lowe's (2004) Scale Invariant Feature Transform (SIFT). The next step calculates camera position and 3D location (*X*, *Y* and *Z*) of tie points by means of a bundle-adjustment algorithm.

The control points were used in the bundle adjustment, 'optimization' in Photoscan. This process reduces non-linear distortions and minimises the total residual error on image observations by simultaneously adjusting camera parameters and orientations, and the 3D point positions (Granshaw, 1980). As a result of these first two steps, a sparse 3D point cloud was generated.

The third step uses the camera locations estimated previously, to produce a dense point cloud using multi-view reconstruction. The dense point clouds were exported into Surfer® 16 software, converted to raster DEMs of 4-mm grid size using the nearest neighbour interpolation method, and cropped to remove the plot edges. The photogrammetric parameters applied on Photoscan in the above-mentioned steps are listed in Table 1.

Table 1. Photoscan parameters settings used during the point cloud generation.

Point cloud: alignment parameters	Setting
Accuracy	Highest
Generic preselection	Yes
Reference preselection	Yes
Key point limit	120,000
Tie point limit	0
Filter point by mask	No
Dense point cloud: reconstruction parameters	
Quality	Medium
Depth filtering	Mild

3.2.5 Erosion measurements using SfM

The erosion measurements in each plot were performed using the Simpson's rule method (see Easa, 1988), which assumes nonlinearity in the profile between grid points. This technique shows greater precision in the determination of volume compared to linear methods, such as the trapezoidal rule (Fawzy, 2015). The soil volume was converted to mass (kg) through soil bulk density, to correlate with the sediment collected from each runoff tank in the interval between the two drone flights.

DEMs of difference (DoD) were calculated to detect changes in the soil surface topography over time and to spatially quantify the volumes of sediment that were eroded and deposited. This technique consists of subtracting georeferenced DEMs from different periods to generate a raster of morphological change:

$$\mathrm{DoD} = \mathrm{DEM}_{t2} - \mathrm{DEM}_{t1} \qquad (1)$$

where *t1* is the initial time and *t2* is the consecutive time of DEM acquisition. Positive and negative values in the DoDs show deposition and erosion respectively.

3.2.6 DEM uncertainty and Level of Detection (LoD)

DEM uncertainty was assessed through the generation of precision estimates based on a Monte Carlo approach (James et al., 2017a) with post-processing tools in sfm_georef software (James and Robson, 2012). This method consists of repeated bundle adjustments in Photoscan, in which different pseudo-random offsets are applied to the image observations and the control measurements to simulate observation measurement precision. Precision estimates for each optimised model parameter were then derived by characterising the variance for each particular parameter in the outputs from the large number of adjustments. In this study, 4,000 bundle adjustments were carried out, as used by James et al. (2017a).

Precision maps were generated through the interpolation (4-mm grid size) of the vertical standard deviation (σ_Z) derived by the precision estimates, to enable precision estimates for both DEMs to be propagated into the DoD as vertical uncertainties (Taylor, 1997; Wheaton et al., 2010). A spatially varying 'level of detection' (LoD) of significant elevation change was calculated for each DoD cell, according to the equation:

$$\mathrm{LoD} = t({\sigma_{Z1}}^2 + {\sigma_{Z2}}^2)^{1/2} \tag{2}$$

where σ_{Z1} and σ_{Z2} are the vertical precision estimates for each cell in the two DEMs and t is the t-distribution value defined by a specific confidence level (this study 95%, giving $t = 1{\cdot}96$). Thus, changes smaller than the LoD can be disregarded, and Surfer was used to generate the LoD-thresholded DoD maps.

3.2.7 Statistical analysis

For assessing the agreement between measurements obtained by sediment collection (response variable) and by SfM (explanatory variable) a linear regression model was fit to the data. Because the same plots were repeatedly used through time for data collection, we investigated whether measurements from the same plot were statistically dependent by introducing a random intercept for each plot in the linear regression model, following a mixed modelling approach (Gelman and Hill, 2007; Zuur et al., 2009).

However, after fitting the model, we observed that the variance associated with the random intercept was null, indicating no evidence of statistical dependence caused by the plot effect. A drawback of that approach is the low number (three) of groups available for estimating the variance associated with the random effect of plots.

As an alternative approach to further investigate whether a statistical dependence among observations could be attributed to a plot effect, an analysis of covariance was performed, with both plot and SfM as explanatory variables, and amount of collected sediments as response variable. In agreement with the results from the previous approach, no significant effect of plots was observed ($F_{2,14} = 0.4$, $P = 0.68$). For the above reasons, the final model was simplified by omitting the plot effect and an ordinary linear regression approach was used, assuming statistical independence of the model residuals.

3.3 Results

3.3.1 Precision results

The photogrammetric errors (RMSE) calculated by the Photoscan on x,y and z-axes for the control, check and tie points of each SfM point cloud are listed in Table 2. The point clouds show average errors of order ~3 mm on *xyz* on control and check points, whereas the tie points image residual RMS was ~ 0·3 pix.

Table 2. Root mean square error (RMSE) of check points, control points and tie points image residuals.

Plot	Date	RMS tie points image residuals (pix)	RMSE of control points (mm)			RMSE of check points (mm)		
			X	Y	Z	X	Y	Z
1	06/06/16	0·264	2·464	2·987	2·154	2·387	3·690	1·196
	22/08/16	0·236	2·164	1·626	1·901	1·135	1·583	2·690
	30/11/16	0·305	2·106	2·968	1·071	1·253	2·694	1·214
	22/02/17	0·295	1·572	1·450	2·477	2·100	1·613	4·850
	25/05/17	0·323	2·743	3·520	1·639	1·379	3·307	2·329
	28/09/17	0·271	2·755	2·431	1·540	2·605	2·742	1·472
	26/04/18	0·290	1·169	0·802	0·570	1·015	1·133	1·953
2	06/06/16	0·307	3·682	2·511	2·140	2·254	3·219	3·211
	22/08/16	0·292	3·752	1·827	1·120	3·328	2·255	2·765
	30/11/16	0·27	3·047	1·704	1·516	3·468	1·308	3·176
	22/02/17	0·275	2·864	1·907	2·299	2·905	2·427	1·803
	25/05/17	0·318	3·754	2·182	2·553	1·011	1·173	1·864

	28/09/17	0·255	2·720	1·540	1·098	2·312	1·437	2·829
	26/04/18	0·388	2·421	2·013	2·274	3·080	2·066	1·834
3	06/06/16	0·363	3·507	2·015	1·964	3·017	3·797	5·500
	22/08/16	0·332	3·133	2·695	1·277	3·506	1·709	0·737
	30/11/16	0·277	3·068	3·563	1·261	3·441	3·826	1·399
	22/02/17	0·269	2·500	2·599	1·237	1·981	2·218	2·221
	25/05/17	0·331	1·721	2·193	0·999	0·943	2·298	2·658
	28/09/17	0·273	2·880	1·579	1·380	2·776	2·274	1·138
	26/04/18	0·292	1·544	2·280	1·172	1·463	2·701	1·646

The LoD maps show the spatial variation of precision along the plot (Fig. 3), with values ranging from 1·4 mm to 7·4 mm. The larger values were concentrated in the area with less image overlap.

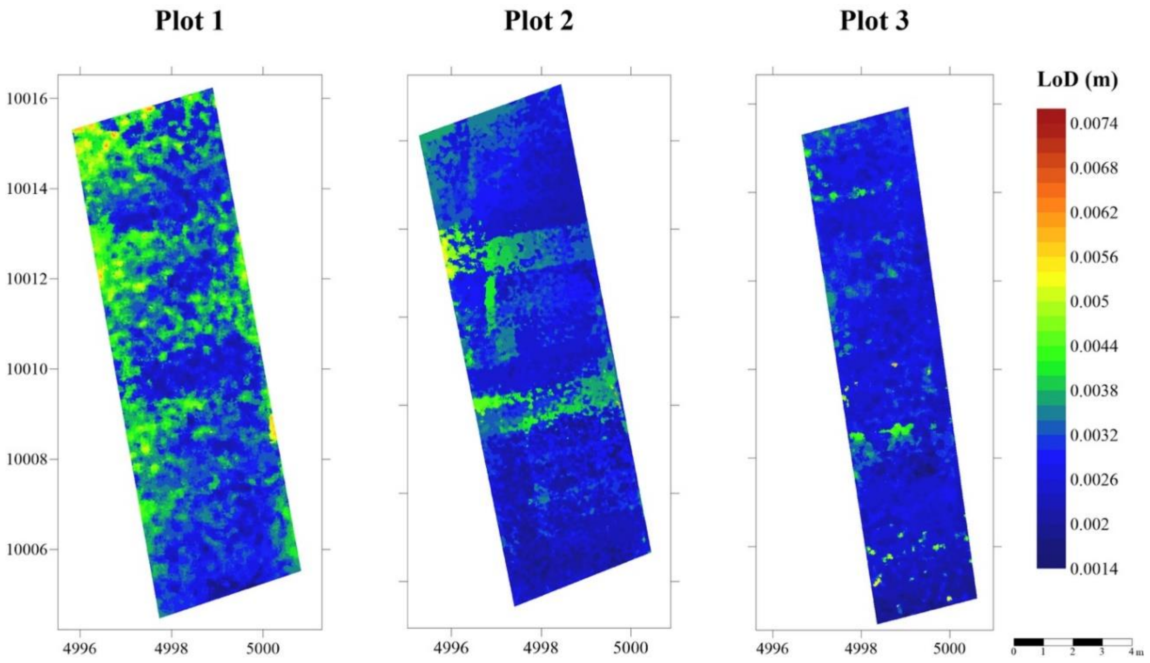

Fig. 3. Level of detection (LoD) maps showing the spatial distribution of potential error along the flume. Changes with magnitudes smaller than the LoD can be disregarded.

3.3.2 DEM of Difference (DoD)

The DoD maps obtained from the erosion plots (Fig. 4) showed remarkable variations in relation to soil movement over the studied period, with 95% of the area showing significant changes in soil surface (i.e. larger than LoD). Although erosion was predominant, it was also possible to detect soil deposition, mainly in the lower part of the plots near the sediment collectors. The periods where there were major soil movements were between November 2016 - February 2017 and September 2017 - April 2018 (Fig. 4), which match with the rainy season in the Southwest of Brazil. The dry season, which corresponds to the period between May and September, was also represented by the DoD maps, by less soil movement along the plot.

Sheet erosion was the predominant type of soil erosion over the study period. However, between September 2017 - April 2018, it was possible to observe the formation of rill erosion, where the highest rates of water erosion were concentrated.

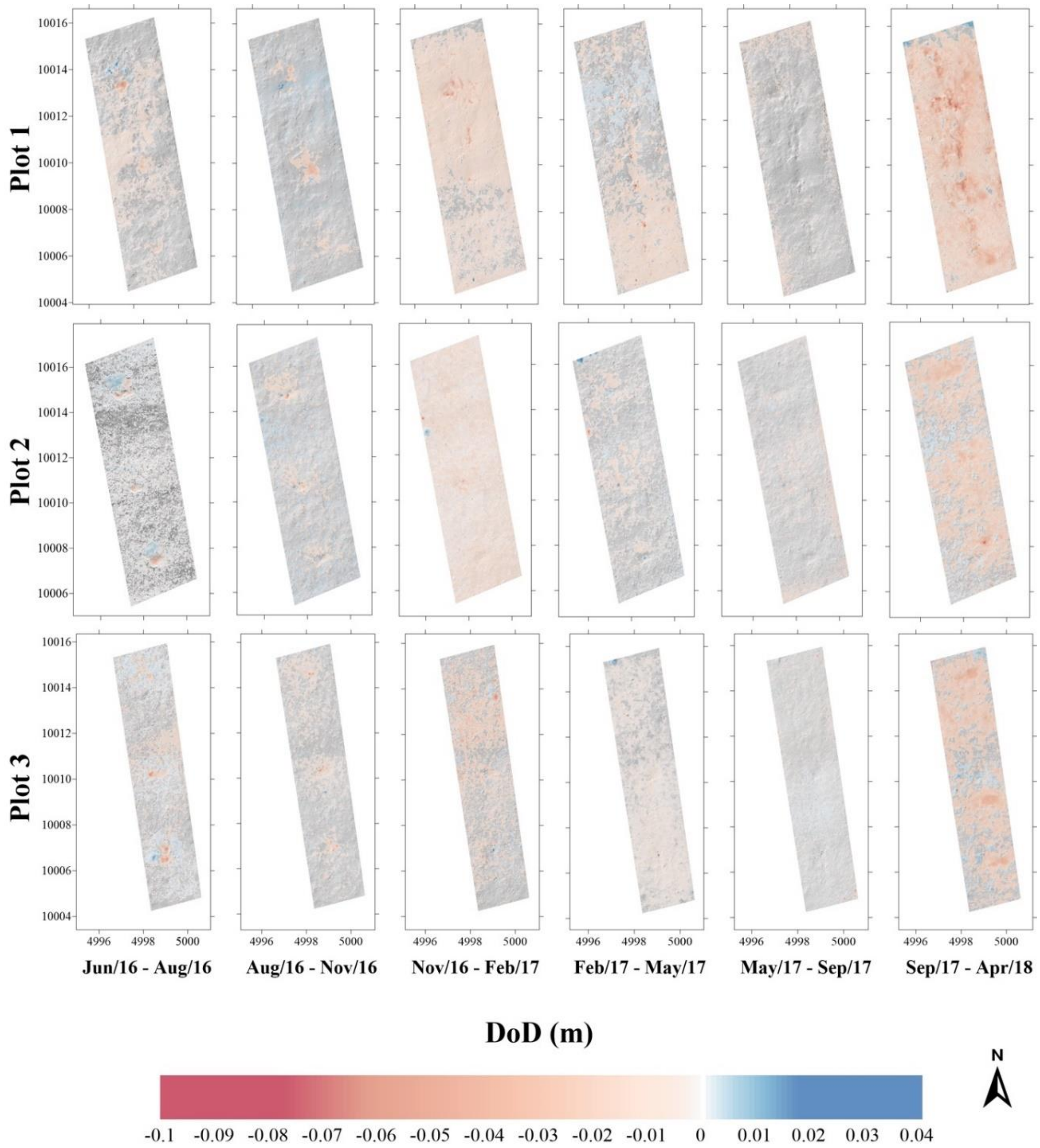

Fig. 4. DEM of difference (DoD) maps, overlain over hillshaded topography, showing soil erosion over natural runoff. Colour scale ranges from red (erosion) to blue (deposition). Transparent regions mean no significant changes (DoD is less than the level of detection).

3.3.3 Erosion measurements

The soil loss values obtained by SfM showed a high correlation (R^2 = 95·55%) with the traditional sediment collection method (Fig. 5). Considering the measurements performed by both methods, it was observed that the values of soil losses obtained through the sediment collection tended to present values slightly higher than those found by the SfM (Table 3). However, the soil loss measurements made by the SfM were closely related to the amount of sediments collected in all seasons of the year, both in summer (rainy season) and winter (dry season).

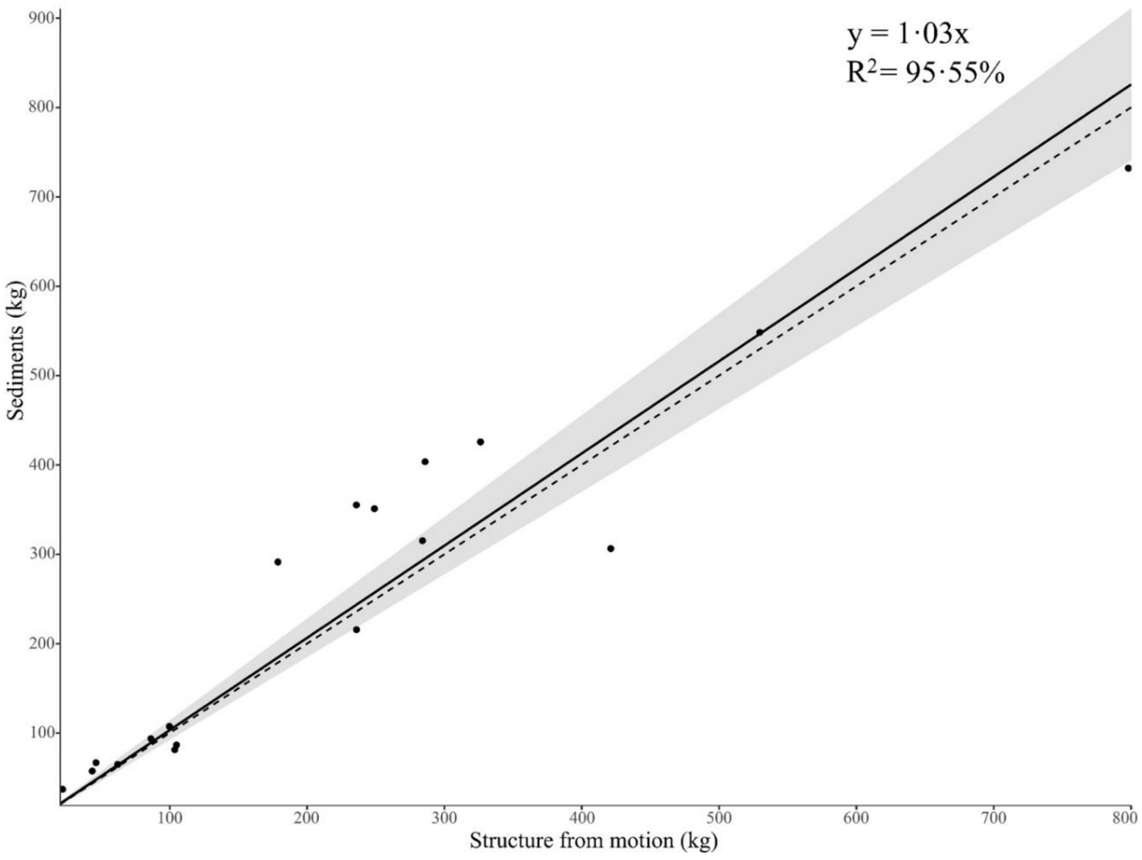

Fig. 5. The relationship between the soil loss from sediments collection and structure from motion method. The dashed line represents the 1:1 relation. The grey zone is the confidence interval for the mean.

Table 3. Averaged soil loss calculated from sediment collection and structure from motion (SfM), and natural rainfall rates during each studied period.

Date	Sediments (kg)	SfM (kg)	Rainfall (mm)
Jun/2016 – Aug/2016	53.04	42.57	92
Aug/2016 – Nov/2016	129.93	127.40	194
Nov/2016 – Feb/2017	418.20	338.20	661
Feb/2017 – May/2017	304.33	294.67	149
May/2017 – Sep/2017	87.13	98.33	115
Sep/2017 – Apr/2018	520.45	470.11	1121

Measurements using the SfM followed the sediment data for the three studied plots. However, in plot 1 the magnitude of the water erosion values in rainy periods was higher than the other two monitored plots (Fig.6).

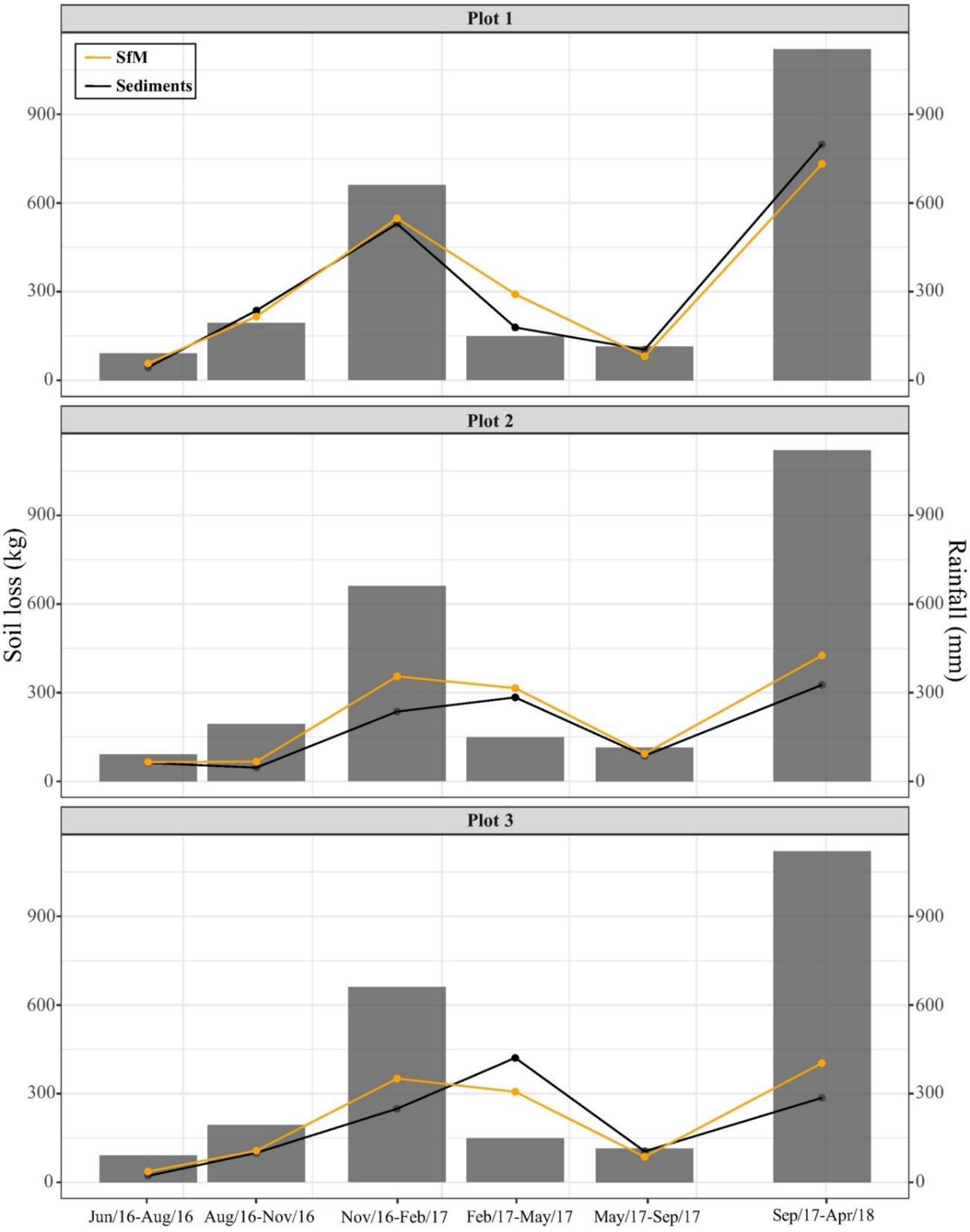

Fig. 6. Soil loss measurements calculated from structure from motion (SfM) and sediment collection for three erosion plots. Lines are to illustrate trend and do not imply a relationship between the points. The grey bars show the amount of rainfall during each studied period.

3.4 Discussion

3.4.1 Erosion measurements from SfM

This was the first time the use of SfM to determine 'sheet' flow has been evaluated independently using sediment collection. The high correlation between the soil loss from SfM and collected on runoff tanks opens up the possibility to use SfM for erosion studies where channelized erosion is not the principal mechanism. This represents a great step forward on soil erosion assessment around the world. Also, due to the limitations related to erosion plots, such as high operational costs, measurements variability, due to human disturbance in collecting data (Zobisch et al., 1996) and plots of different sizes (Bagarello and Ferro, 2004), the SfM can potentially increase the quality of the global soil erosion database.

Soil erosion is a process composed of three sub-processes: erosion, transport, and deposition (Morgan, 2005). Sediment and surface runoff collections are restricted to the evaluation of the amount of soil lost rather than the soil erosion volume, since the traditional method does not allow the determination of the mass of soil moved during erosion-transport-deposition processes. Through SfM, it is possible to generate erosion and deposition maps that allow the volume of soil moved at different times and positions to be determined (Fig. 4). In addition, this method can distinguish the differences between soil eroded volume and soil lost volume. Also, it can be used to investigate the sediment delivery rate (Guo et al., 2016).

However, SfM does rely on images of the soil surface, meaning that it is not suitable for areas with significant vegetation cover. Thus, applying the SfM technique to measure erosion in cultivated areas, where the highest soil loss values occur, is still a major challenge. To overcome this limitation and allow soil surface 3-D reconstruction in vegetation cover areas, vegetation filtering algorithms are being developed (e.g. CANUPO (Brodu and Lague, 2012) or CSF (Zhang et al., 2016)). However, the accuracy of DEMs obtained from these techniques is not yet enough to measure laminar erosion accurately.

In periods with high precipitation values, the highest soil loss values found by SfM, compared to the collected sediments, in plots 2 and 3 (Fig. 6), occurred because the SfM soil loss calculations considered the variation in microtopography and high rainfall can change the soil surface, promoting its consolidation. Soil consolidation occurs because of gravity causing particles to collapse due to their own weight and the impact of raindrops (Eltner et al., 2015). SfM will also capture changes to the soil surface that are not due to erosion, for example the consolidation of the soil following tillage (Eltner et al., 2015), crusting and degradation of the soil structure are expected due to wetting and drying cycles, causing reduction of soil roughness, or its disturbance by soil animals.

3.4.2 Evaluation of SfM accuracy

The accuracy of the 3D point coordinates acquired from SfM can be affected by photogrammetric factors such as image geometry and georeferencing (James et al., 2017a). In this study, the spatial variation of LoD was related to photogrammetry, more precisely to the image overlap along the flight. This occurred due to the manual navigation of the UAV used in this study, which requires operator care to achieve the necessary coverage of the monitored area. In addition, flight speed must be adjusted to achieve the required overlap among photographs and reduce risks of blurred images at high speeds.

Other factors that influence the accuracy of SfM models are surface types (mainly vegetation), soil roughness, and the presence of water (Eltner et al., 2015; James et al., 2017b). In the present study, considering only the bare soil, the SfM results showed a strong correlation with the values obtained by the sediment collection (Fig. 5). However, it is important to note that areas with vegetation present a complication for the interpretation of erosion measured using UAV. This is of great importance for regions where soil loss changes from vegetated to a non-vegetated surface.

SfM point clouds tend to smooth the soil surface in smaller scale roughness. This can be controlled by the quality parameters in Photoscan during dense cloud generation; but cloud noise might increase when “ultra-high quality” is used (Cook, 2017). Thus, care should be taken when analysing roughness surface data by choosing flight heights, overlapping, and image resolution to ensure accurate representation of the soil surface texture at the desired scale. The smoothing of photogrammetric data has been observed (Smith et al., 2004; Jester and Klik, 2005); however, the effect of the measurement technique has been combined with the interpolation effect during the generation of DEM or meshing (Lane et al., 2000).

3.5 Conclusions

This work evaluated for the first time the capacity of SfM in measuring soil erosion comparing with independent data collected from runoff tanks. The high correlation between the soil loss from SfM and collected on runoff tanks opens up the possibility to use SfM for erosion studies where channelized erosion is not the principal mechanism, enabling new insights into sheet, and interrill, erosion processes.

The use of UAV associated with the SfM technique generates a cheap, portable, and easy way to obtain erosion measurements on a smaller scale with high accuracy, in contrast to the traditional standard plot methods of erosion monitoring worldwide. The results of SfM allows not only the quantification of soil loss, for later use in models such as USLE, but also represents the spatial and temporal dimensions of the soil erosion process, which is of great importance in understanding the mechanisms of the water erosion.

3.6 References

Agüera-Vega, F., Carvajal-Ramírez, F., Martínez-Carricondo, P., López, J.S-H., Mesas-Carrascosa, F.J., García-Ferrer, A., Pérez-Porras, F.J., 2018.

Araya, T., Cornelis, W.M., Nyssen, J., Govaerts, B., Bauer, H., Gebreegziabher, T., Oicha, T., Raes, D., Sayre, K.D., Haile, M., Decker, J., 2011. Effects of conservation agriculture on runoff, soil loss and crop yield under rainfed conditions in Tigray, Northern Ethiopia. Soil Use Manage. 27, 404–414.

Bagarello, V., Ferro, V., 2004. Plot-scale measurement of soil erosion at the experimental area of Sparacia (southern Italy). Hydrol. Process. 18, 141–157.

Bakker, M.M., Govers, G., Rounsevell, M.D., 2004. The crop productivity–erosion relationship: an analysis based on experimental work. Catena 57, 55–76.

Bazoffi, P., 2015. Measurement of rill erosion through a new UAV-GIS methodology. Ital. J. Agron. 10, s1:708.

Boardman, J., Evans, R., Ford, J., 2003. Muddy floods on the South Downs, southern England: problem and responses. Environ. Sci. Pol. 6, 69–83.

Brunier, G., Fleury, J., Anthony, E.J., Gardel, A., Dussouillez, P., 2016. Close-range airborne structure-from-motion photogrammetry for high-resolution beach morphometric surveys: examples from an embayed rotating beach. Geomorphology 261, 76–88.

Castillo, C., Pérez, R., James, M.R., Quinton, J.N., Taguas, E.V., Gómez, J.A., 2012. Comparing the accuracy of several field methods for measuring gully erosion. Soil Sci. Soc. Am. J. 76, 1319–1332.

Cerdan, O., Govers, G., Le Bissonnais, Y., Van Oost, K., Poesen, J., Saby, N., Gobin, A., Vacca, A., Quinton, J., Auerswald, K., Klik, A., Kwaad, F., Raclot, D., Ionita, I., Rejman, J., Rousseva, S., Muxart, T., Roxo, M., Dostal, T., 2010. Rates and spatial variations of soil erosion in Europe: A study based on erosion plot data. Geomorphology 122, 167–177.

Cook, K.L., 2017. An evaluation of the effectiveness of low-cost UAVs and structure from motion for geomorphic change detection. Geomorphology 278, 195–208.

Colomina, I., Molina, P., 2014. Unmanned aerial systems for photogrammetry and remote sensing: a review. ISPRS J. Photogramm. Remote Sens. 92, 79–97.

Di Stefano, C., Ferro, V., 2017. Testing sediment connectivity at the experimental SPA2 basin, Sicily (Italy). Land Degrad. Dev. 28, 1992–2000.

Dietrich, J.T., 2016. Riverscape mapping with helicopter-based Structure-from-Motion photogrammetry. Geomorphology 252, 144–157.

Easa, S.M., 1988. Estimating pit excavation volume using nonlinear ground profile. J. Surv. Eng. 114, 71–83.

Eltner, A., Baumgart, P., Maas, H.G., Faust, D., 2015. Multi-temporal UAV data for automatic measurement of rill and interrill erosion on loess soil. Earth Surf. Process. Landf. 40, 741–755.

Eltner, A., Maas, H-G., Faust, D., 2018. Soil micro-topography change detection at hillslopes in fragile Mediterranean landscapes. Geoderma 313, 217–232.

Fang, N.F., Wang, L., Shi, Z.H. Runoff and soil erosion of field plots in a subtropical mountainous region of China. J. Hydrol. 552, 387–395.

Fawzy, H.E-D., 2015. The accuracy of determining the volumes using close range photogrammetry. J. Mech. Civ. Eng. 12, 10–15.

Fonstad, M.A., Dietrich, J.T., Courville, B.C., Jensen, J.L., Carbonneau, P.E., 2013. Topographic structure from motion: a new development in photogrammetric measurement. Earth Surf. Process. Landf. 38, 421–430.

García-Ruiz, J.M., Beguería, S., Nadal-Romero, E., González-Hidalgo, J.C., Lana-Renault, N., Sanjuán, Y. A meta-analysis of soil erosion rates across the world. Geomorphology, 239, 160–173.

Gelman, A., Hill, J., 2007. Data analysis using regression and multilevel/hierarchical models. Cambridge University Press, New York.

Gómez-Gutiérrez, A., Schnabel, S., Berenguer-Sempere, F., 2014. Using 3D photo-reconstruction methods to estimate gully headcut erosion. Catena 120, 91–101.

Glendell, M., McShane, G., Farrow, L., James, M., Quinton, J., Anderson, K., Evans, M., Benaud, P., Rawlins, B., Morgan, D., Jones, L., Kirkham, M., DeBell, L., Quine, T., Lark, M., Rickson, J., Brazier, R., 2017. Testing the utility of structure from motion photogrammetry reconstructions using small unmanned aerial vehicles and ground photography to estimate the extent of upland soil erosion. Earth Surf. Process. Landf. 42, 1860–1871.

Granshaw, S.I., 1980. Bundle adjustment methods in engineering photogrammetry. Photogramm. Rec. 10, 181–207.

Guo, M., Shi, H., Zhao, J., Liu, P., Welbourne, D., Lin, Q., 2016. Digital close range photogrammetry for the study of rill development at flume scale. Catena 143, 265–274.

Guo, Q., Hao, Y., Liu, B., 2015. Rates of soil erosion in China: a study based on runoff plot data. Catena, 124, 68–76.

Hänsel, P., Schindewolf, M., Eltner, A., Kaiser, A., Schmidt, J., 2016. Feasibility of high-resolution soil erosion measurements by means of rainfall simulations and SfM photogrammetry. Hydrology 3 (38).

James, M.R., Quinton, J.N., 2014. Ultra-rapid topographic surveying for complex environments: the hand-held mobile laser scanner (HMLS). Earth Surf. Process. Landf. 39, 138–142.

James, M.R., Robson, S., 2012. Straightforward reconstruction of 3D surfaces and topography with a camera: accuracy and geoscience application. J. Geophys. Res. 117, F03017.

James, M.R., Robson, S., 2014. Mitigating systematic error in topographic models derived from UAV and ground-based image networks. Earth Surf. Process. Landf. 39, 1413–1420.

James, M.R., Robson, S., Smith, M.W., 2017a. 3-D uncertainty-based topographic change detection with structure-from-motion photogrammetry: precision maps for ground control and directly georeferenced surveys. Earth Surf. Process. Landf. 42, 1769–1788.

James, M.R., Robson, S., d'Oleire-Oltmanns, S., Niethammer, U., 2017b. Optimising UAV topographic surveys processed with structure-from-motion: Ground control quality, quantity and bundle adjustment. Geomorphology 280, 51–66.

Jester, W., Klik, A., 2005. Soil surface roughness measurement—methods, applicability, and surface representation. Catena 64, 174–192.

Lal, R., 1998. Soil erosion impact on agronomic productivity and environment quality. CRC Crit. Rev. Plant Sci. 17, 319–464.

Lane, S.N., James, T.D., Crowell, M.D., 2000. Application ofdigital photogrammetry to com- plex topography for geomorphological research. Photogramm. Rec. 16, 793–821.

Lane, S.N., Westaway, R.M., Hicks, D.M., 2003. Estimation of erosion and deposition volumes in a large, gravel-bed, braided river using synoptic remote sensing. Earth Surf. Process. Landf. 28, 249–271.

Lowe, D., 2004. Distinctive image features from scale-invariant keypoints. Int. J. Comput. Vis. 60, 91–110.

Mancini, F., Dubbini, M., Gattelli, M., Stecchi, F., Fabbri, S., Gabbianelli, G., 2013. Using unmanned aerial vehicles (UAV) for high-resolution reconstruction of topography: The structure from motion approach on coastal environments. Remote Sens. 5, 6880–6898.

Morgan, R.P.C., 2005. Soil Erosion and Conservation. third ed. Blackwell Publishing Ltd., Cornwall.

Morgan, J.A., Brogan, D.J., Nelson, P.A., 2017. Application of Structure-from-Motion photogrammetry in laboratory flume. Geomorphology 276, 125–143.

Neugirg, F., Stark, M., Kaiser, A., Vlacilova, M., Della Seta, M., Vergari, F., Schmidt, J., Becht, M., Haas, F., 2016. Erosion processes in calanchi in the upper Orcia Valley, southern Tuscany, Italy based on multitemporal high-resolution terrestrial LiDAR and UAV surveys. Geomorphology 269, 8–22.

Nouwakpo, S., Weltz, M., McGwire, K., 2015. Assessing the performance of structure-from-motion photogrammetry and terrestrial lidar for reconstructing soil surface microtopography of naturally vegetated plots. Earth Surf. Process. Landf. 41, 308–322.

Ouédraogo, M.M., Degré, A., Debouche, C., Lisein, J., 2014. The evaluation of unmanned aerial system-based photogrammetry and terrestrial laser scanning to generate DEMs of agricultural watersheds. Geomorphology 214, 339–355.

Papiernick, S.K., Schumacher, T.E., Lobb, D.A., Lindstrom, M.J., Lieser, M.L., Eynard, A., Schumacher, J.A., 2009. Soil properties and productivity as affected by topsoil movement within an eroded landform. Soil Tillage Res. 102, 67–77.

Phan Ha, H.A.P., Huon, S., Henry des Tureaux, T.H., Orange, D., Jouquet, P., Valentin, C., De Rouw, A., Tran Duc, T.T., 2012. Impact of fodder cover on runoff and soil erosion at plot scale in a cultivated catchment of North Vietnam. Geoderma 177, 8–17.

Prosdocimi, M., Burguet, M., Di Prima, S., Sofia, G., Terol, E., Rodrigo Comino, J., Cerdá, A., Tarolli, P., 2017. Rainfall simulation and structure-from-motion photogrammetry for the analysis of soil water erosion in Mediterranean vineyards. Sci. Total Environ. 574, 204–215.

Quinton, J.N., Govers, G., Van Oost, K., Bardgett, R.D., 2010. The impact of agricultural soil erosion on biogeochemical cycling-s2. Nat. Geosci. 3, 1–6.

Seitz, S.M., Curless, B., Diebel, J., Scharstein, D., Szeliski, R., 2006. A comparison and evaluation of multi-view stereo reconstruction algorithms. IEEE Conference on Computer Vision and Pattern Recognition. IEEE Computer Society, New York.

Smith, M.J., Asal, F.F.F., Priestnall, G., 2004. The use of photogrammetry and lidar for landscape roughness estimation in hydrodynamic studies. Int. Arch. Photogramm. Remote. Sens. Spat. Inf. Sci. 35 (B3), 714–719.

Stöcker, C., Eltner, A., Karrasch, P., 2015. Measuring gullies by synergetic application of UAV and close range photogrammetry — a case study from Andalusia, Spain. Catena 132, 1–11.

Stumpf, A., Malet, J.P., Kerle, N., Niethammer, U., Rothmund, S., 2013. Image-based mapping of surface fissures for the investigation of landslide dynamics. Geomorphology 186, 12–27.

Taylor, J.R., 1997. An Introduction to Error Analysis: the Study of Uncertainties in Physical Measurements, second edition. University Science Books: Sausalito, California.

Ullman, S., 1979. The interpretation ofstructure from motion. Proc. R. Soc. Lond. B Biol. Sci. 203, 405–426.

Warrick, J., Ritchie, A., Adelman, G., Adelman, K., Limber, P., 2017. New techniques to measure cliff change from historical oblique aerial photographs and structure-from-motion photogrammetry. J. Coast. Res. 33, 39 – 55.

Westoby, M., Brasington, J., Glasser, N., Hambrey, M., Reynolds, J., 2012. 'Structure-from-motion' photogrammetry: a low-cost, effective tool for geoscience applications. Geomorphology 179, 300–314.

Westoby, M., Dunning, S., Woodward, J., Hein, A., Marrero, S., Winter, K., Sugden, D., 2016. Interannual surface evolution of an Antarctic blue-ice moraine using multi-temporal DEMs. Earth Surf. Dyn. 4, 515–529.

Wheaton, J., Brasington, J., Darby, S., Sear, D., 2010. Accounting for uncertainty in DEMs from repeat topographic surveys: improved sediment budgets. Earth Surf. Process. Landf. 35, 136–156.

White, J., Wulder, M., Vastaranta, M., Coops, N., Pitt, D., Woods, M., 2013. The utility of image-based point clouds for forest inventory: a comparison with airborne laser scanning. Forests 4, 518–536.

Zhao, J., Van Oost, K., Chen, L., Govers, G., 2016. Moderate topsoil erosion rates constrain the magnitude of the erosion-induced carbon sink and agricultural productivity losses on the Chinese Loess Plateau. Biogeosciences 13, 4735–4750.

Zhao, J., Yang, Z., Govers, G. Soil and water conservation measures reduce soil and water losses in China but not down to background levels: Evidence from erosion plot data. Catena 337, 729–741.

Zobisch, M.A., Klingspor, P., Oduor, A.R., 1996. The accuracy of manual runoff and sediment sampling from erosion plots. J. Soil Water Conserv. 51, 231–1233.

Zuur, A.F., Ieno, E.N., Walker, N.J., Saveliev, A.A., Smith, G.M., 2009. Mixed effects models and extensions in ecology with R. Springer, New York, New York, USA.

4. Evaluation of sediment source and volume of soil erosion in a gully system using structure-from-motion and UAV data: A case study from Minas Gerais, Brazil

4.1 Introduction

Gullies represent a significant source of sediments, especially in tropical environments (Poesen, 2011), reaching areas of about 3·5 ha for a single gully (Lin et al., 2015). Gully erosion can be defined as being an erosive process where the water concentrates in the landscape, being affected by the presence of tracks and the lack of conservation measurements in the area (Poesen et al., 2002; Valentin et al., 2005; Lin et al., 2015). The concentrated flow reduces top soil by the gully initiation, causing severe impacts in farmland productivity and waterways sedimentation (Allen et al., 2018; Bastola et al., 2018; Zabihi et al., 2018).

Long-term studies report that gullies develop randomly and are linked with the natural mass movements associated with the removal of vegetation cover (Harvey, 1997; Lin et al., 2015). However, gully development involves several sub-processes related to water erosion and mass movements, such as detachment, transport and deposition of sediments, gully bank retreat, piping and fluting (Harvey, 1992). The complex interaction between these sub-processes, with erosion and deposition occurring simultaneously in the area (Gómez-Gutiérrez et al., 2012), coupled with the three-dimensional nature of the gullies, make it difficult to measure and quantify directly in the field (De Rose et al., 1998; Poesen et al., 2003).

Thus, traditional methods such as pins (Desir and Marín, 2007), microtopographic profiles (Casalí et al., 2006), surveys with total stations (Ehirobo and Audu, 2012) and poles are being replaced by techniques based on high-resolution photogrammetry (Castillo et al. 2012). Several studies have quantified gully erosion through photogrammetry associated with three-dimensional soil surface reconstruction methods, such as Structure from Motion (SfM) (Castillo et al., 2012; Gómez-Gutiérrez et al., 2014; Kaiser et al., 2014, Di Stefano et al., 2017; Ben Slimane et al., 2018). However, few studies used the SfM for detailed study of sediment sources and their movement over time in the gully environment. Considering that gullies have a complex growth dynamics, the study of spatial and temporal evolution through aerial images are important for the development of control strategies and mitigation of degraded areas.

Through SfM photogrammetry it is possible to elucidate better the erosive processes that occur in the gully system, by obtaining DEMs with high spatial and temporal resolution. With recent advances in the use and availability of unmanned aerial vehicles (UAVs), the use of SfM photogrammetry to produce high-resolution DEMs has become popular in geosciences (d'Oleire-Oltmanns et al., 2012; Carollo et al., 2015; Di Stefano et al., 2017), because it is cheap, less time-consuming, requires little knowledge due to the automation of processes and has similar accuracy to the most accurate methods currently available (such as laser scanning) (Castillo et al., 2012; James and Robson, 2012; Fonstad et al., 2013).

The knowledge of the contribution rates of rills and gully sidewalls, as well as the quantification of sediments stored in the channels and lost from the gully system is important for the development of effective strategies to control soil erosion in gullies (Hosseinalizadeh et al., 2019). This spatial and temporal variation of sediments in gully development are indicators used by land managers to identify the stage of development and stabilization of the gully system (Betts et al., 2003). When the amount of lost sediment becomes smaller than that stored in the channels, it indicates a stabilization of the erosive process in the gully (Kasai et al., 2001).

Although many studies have described the formation and development processes of gullies (Harvey, 1992; Vandekerckhove et al., 1998; Sidorchuk et al., 2003; Conoscenti et al., 2014), few papers have evaluated the high spatial resolution of the dynamics of soil movement along the gully system. Using high-resolution DEMs it is possible to elucidate the complex erosion processes that occur simultaneously in gullies, visualize the dynamics of soil movement in the system over time and devise effective strategies to mitigate sediment delivery in watercourses.

The changes in the macro and micro topography of the gully system requires the understanding of the continuous process of source-transport-deposition of sediments (Valentin et al., 2005). Thus, the objectives of this study were to use SfM (1) to determine the relative contribution of rills and gully sidewalls to sediment generation, (2) to quantify the sediment volumes stored in channels and lost from the gully, and (3) to quantify the total volume of sediments produced by the gully.

4.2 Materials and Methods

4.2.1 Study area

The studied gully is located in a degraded area (Fig. 1) on the campus of the Federal University of Lavras, Southeastern Brazil (21°13'37.3" S and 44°59'11.9" W). The study area has a humid subtropical climate and an average annual rainfall of 1,530 mm. The gully has a total catchment area of 530 m^2.

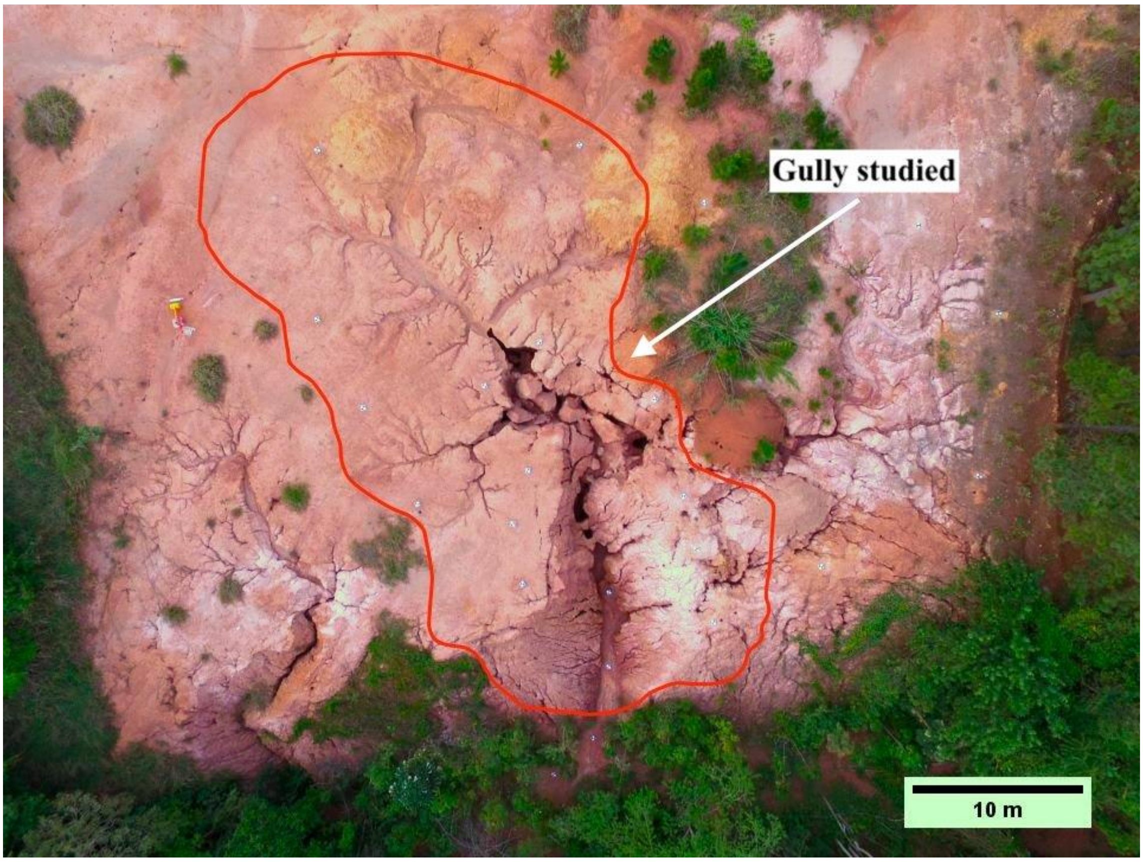

Fig. 1. Location of the study area.

4.2.2 Image acquisition for SfM

Images were acquired using the UAV DJI Phantom 3 Professional integrated with a gimbal-stabilized FC300X camera with 12-megapixel (4000 × 3000) Sony EXMOR 1/2·3 sensor, 94º field of view (FOV) and 20-mm focal length. The lens aperture was set to f/2·8 and images acquired in RAW format. Two flights were performed in the gully area, the first in October 2017 and the second in May 2018.

In order to cover the complex 3-D area of the gully it was acquired oblique images, which also added to the strength of the network geometry (James et al., 2017a). However, as a result of the multiple camera angles, the overlap percentage between the images was highly variable (Fig. 2a). Thus, the number of images in which some point is present was used as the metric to describe the image overlap. In this study, most areas were captured by more than 30 overlapping images, because of the oblique angles. Surveys comprised about 300 images, which reflects the complex nature of the gully morphology. The flying altitudes ranged between 5 and 15 m, resulting in a nominal ground sampling distance between 2 and 6 mm.

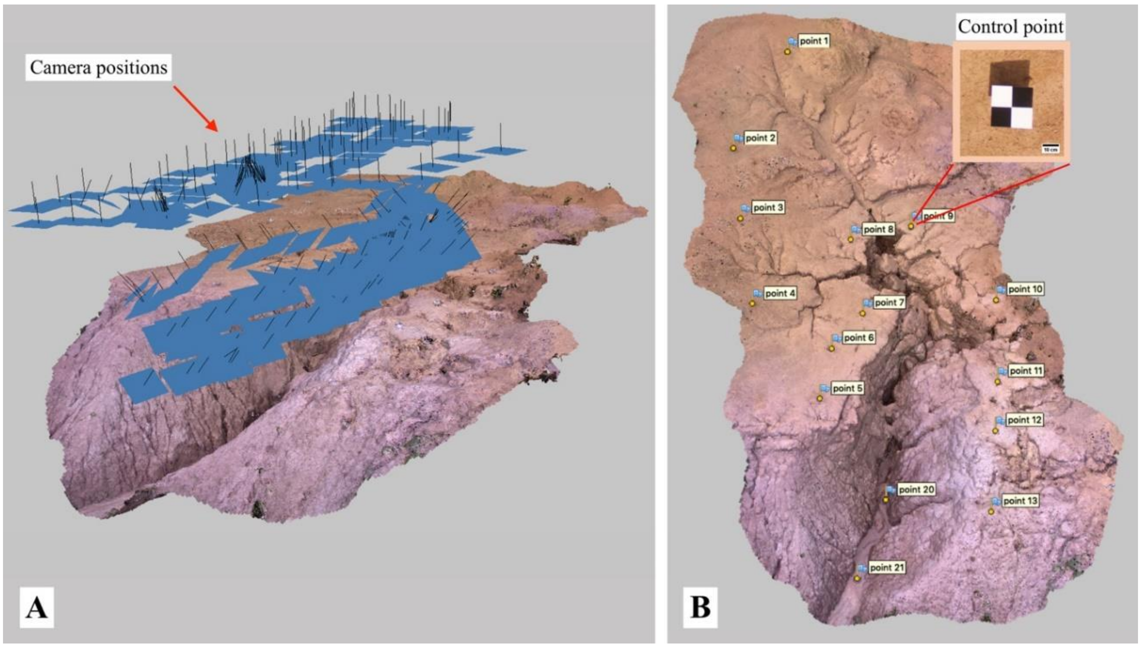

Fig. 2. Annotated computer screenshot of Photoscan showing (a) camera positions and orientations, and (b) control point layout.

To compare the SfM results at different times, both surveys must be in the same coordinate system. Thus, for the georeferencing, 15 permanent ground control points (GCP) were installed in the area (Fig. 2b). The GCP coordinates were determined by a total station (Geodetic GD2i, accuracy 2 mm), within an arbitrary local coordinate system.

4.2.3 SfM point cloud generation

The three-dimensional point clouds (3D) were generated from the sets of photographs using the SfM commercial software Agisoft Photoscan version 1.4.5 (Agisoft, 2018) (see Chapter 1). The photogrammetric parameters used on Photoscan are listed in Table 1. All surface reconstructions were done through cloud computing using a virtual machine with 24 cores, 128 GB RAM and two NVIDIA Tesla K80 GPUs.

Table 1. Photoscan parameters settings used during the point cloud generation.

Point cloud: alignment parameters	Setting
Accuracy	Highest
Generic preselection	Yes
Reference preselection	Yes
Key point limit	120,000
Tie point limit	0
Filter point by mask	No
Dense point cloud: reconstruction parameters	
Quality	High
Depth filtering	Mild

4.2.4 Change detection and 3D precision maps

To evaluate the soil surface changes in the different surveys, it was used the precision maps (PM) variant of the Multiscale Model to Model Cloud Compare algorithm (M3C2; Lague et al., 2013), an analytical tool implemented in CloudCompare. M3C2-PM is a more appropriate technique for analysing complex 3D environments than DEM of Difference (DoD) (Lague et al., 2013). Comparisons using DEMs can overestimate errors on steep terrain since small lateral shifts can produce large vertical differences (Cook, 2017).

The M3C2-PM algorithm finds the most appropriate normal direction for each point and calculates the distance between the two point clouds along a cylinder of a given radius projected along the normal. The comparisons used core points with 1 cm spacing, a cylinder with a 30 cm diameter, and multiscale normals with radii from 0.2 m to 1 m with a step of 0.2 m.

The native M3C2 uses a roughness-based metric to estimate precision, but this is not appropriate for photogrammetric point clouds (James et al., 2017b). Thus, in this study the PM it was used to obtain the confidence intervals in the detection of changes between the surveys. M3C2-PM approach has a greater capacity to detect changes in areas of complex topography, such as gullies, considering the spatial and 3D variation of survey accuracy (James et al., 2017b). A detailed explanation of M3C2-PM is given by James et al. (2017b).

However, in this study, the precision estimates were derived by reprocessing the Photoscan using DBAT bundle adjustment (Murtiyoso et al., 2018), integrated into SfM_georef (James and Robson, 2012). All these data were provided to me by Michael James. The precision maps were generated through the interpolation (5-mm grid size) of the vertical standard deviation (σ_Z) derived by the precision estimates. It was used median as interpolation method to minimise the influence of outliers (James et al., 2017b).

To calculate the gully erosion volume, as well as the relative contribution of rill erosion and mass movements, the dense point clouds were interpolated (5-mm grid size) using the Kriging method. The zones related to each type of erosion were delimited considering as rills channels with more than 0.01 m in width and depth (Foster, 2005) and as gullies channels of at least 0.3 m in width and depth (Blanco and Lal, 2010). The volumes of sediments stored and lost from the gully system were calculated using the Simpson's rule method (Easa, 1988), which assumed non-linearity in the profile between the grid points. The volume calculations and maps were performed using Surfer (Golden Software Inc., Golden, CO).

4.3 Results

4.3.1 Accuracy of SfM point clouds

Both surveys had similar magnitudes of photogrammetric error (Table 2). The point clouds showed average errors of order ~ 4 mm on *xyz* on control and check points, whereas the tie points image residual RMS was ~ 0·6 pix. It was used five check points and ten control points in the area (Fig. 3).

Table 2. Root mean square error (RMSE) of check points, control points and tie points image residuals.

Date	Number of Images	Dense Cloud Points	RMS tie points image residuals (pix)	RMSE of control points (mm)			RMSE of check points (mm)		
				X	Y	Z	X	Y	Z
27/10/17	277	51,002,599	0·568	4·2	2·5	1·3	4·2	4·5	2·0
26/05/18	325	65,475,214	0·561	2·8	3·3	4·5	3·2	3·5	2·6

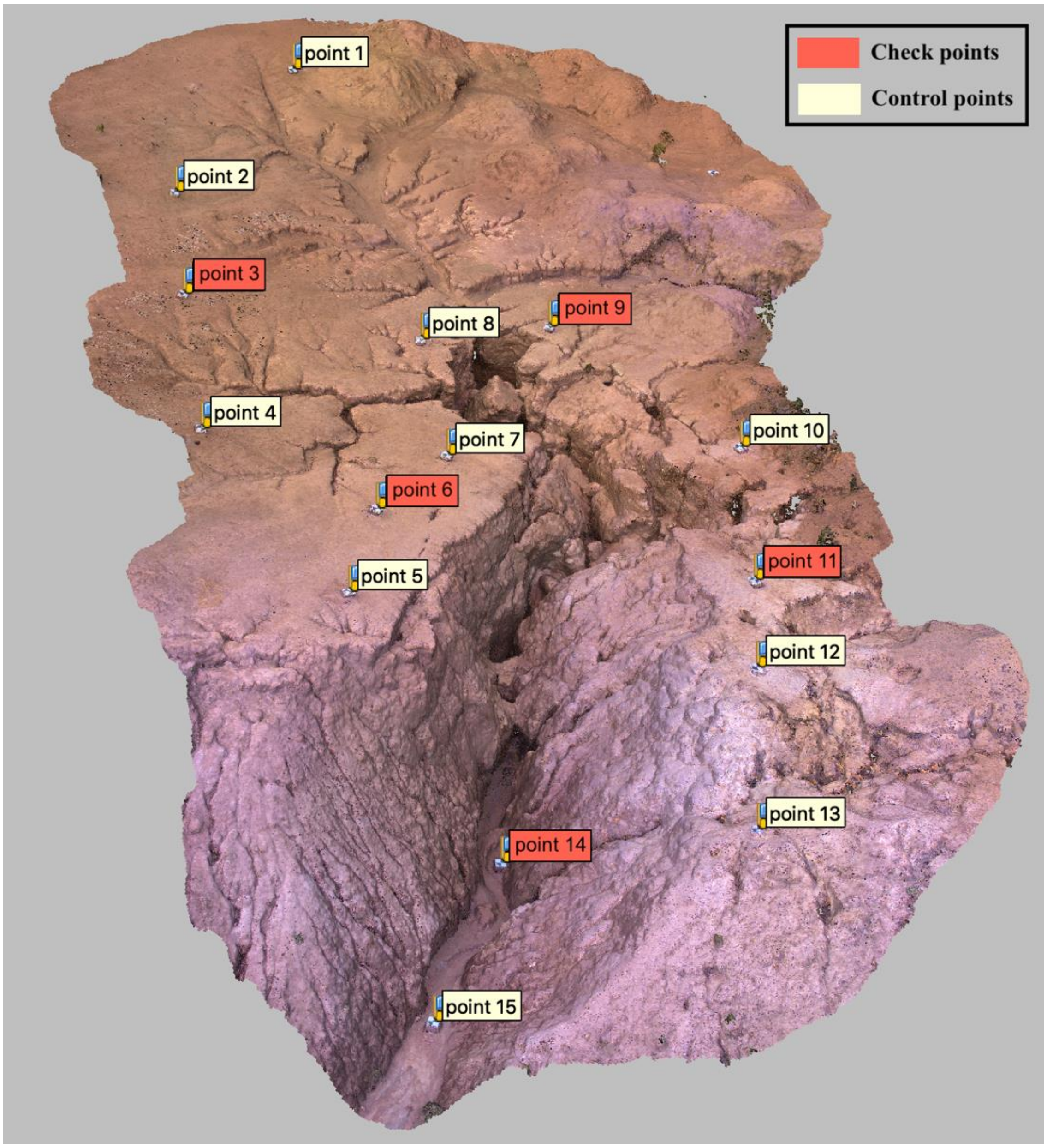

Fig. 3. Location of the control and check points in the study area.

The precision maps show the spatial variation of precision on each survey along the gully, with M3C2-PM uncertainty values ranging from 0·006 m to 0·276 m (Fig. 4). The highest values were concentrated in shaded areas and at the bottom of the gully. The first survey was less accurate than the second one, especially in the more complex areas.

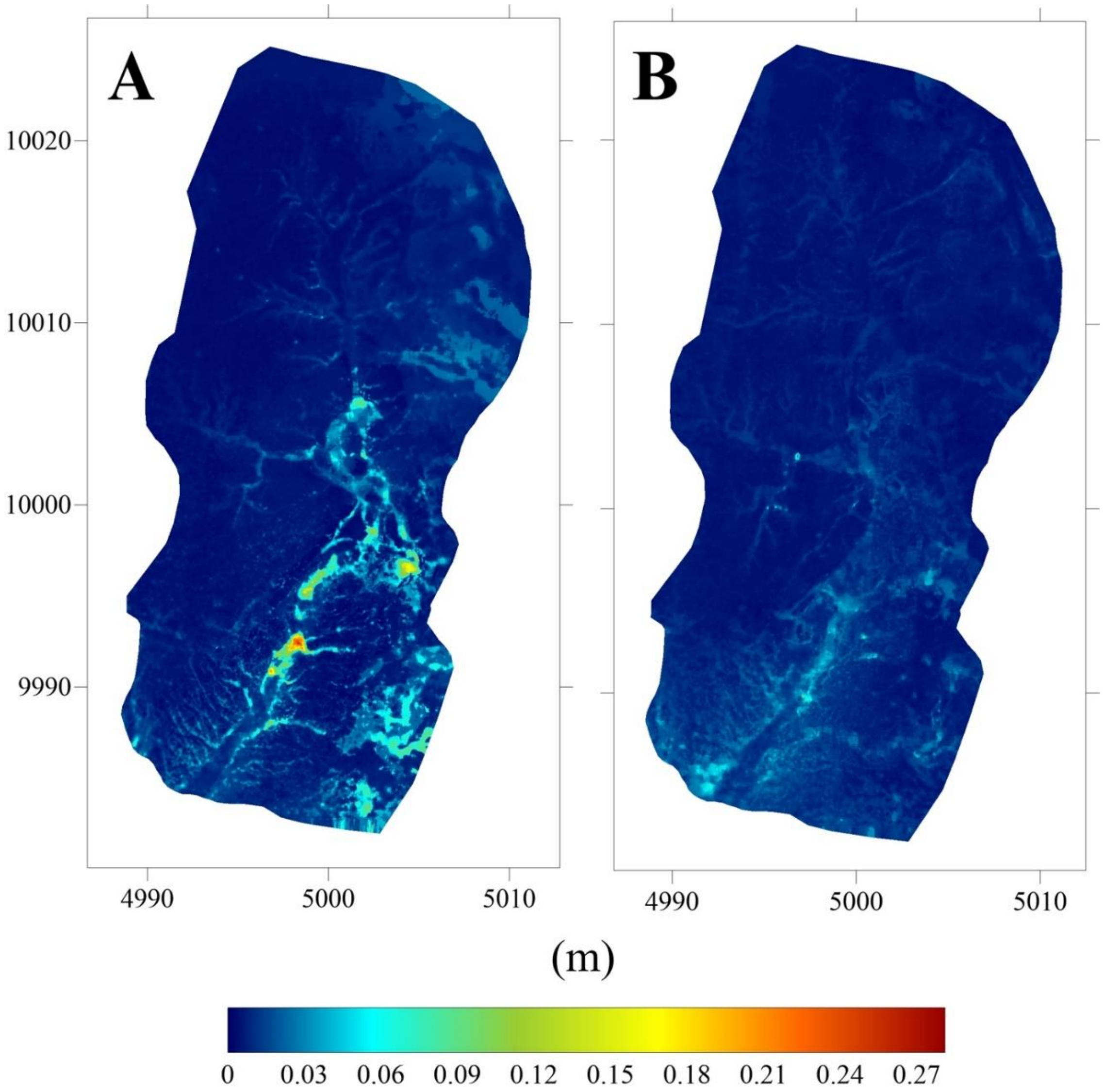

Fig. 4. Precision maps for both October 2017 (A) and May 2018 (B) surveys.

The image overlap, as well as the number of images, were sufficient to produce a distribution of the points in the clouds without large holes. For gully erosion studies, it could be considered a large hole an empty place in the cloud with about 10-cm spacing between the points. The 3D reconstruction of the topography of the most complex areas of the gully was done adequately, reproducing with fidelity the terrain morphology (Fig. 5).

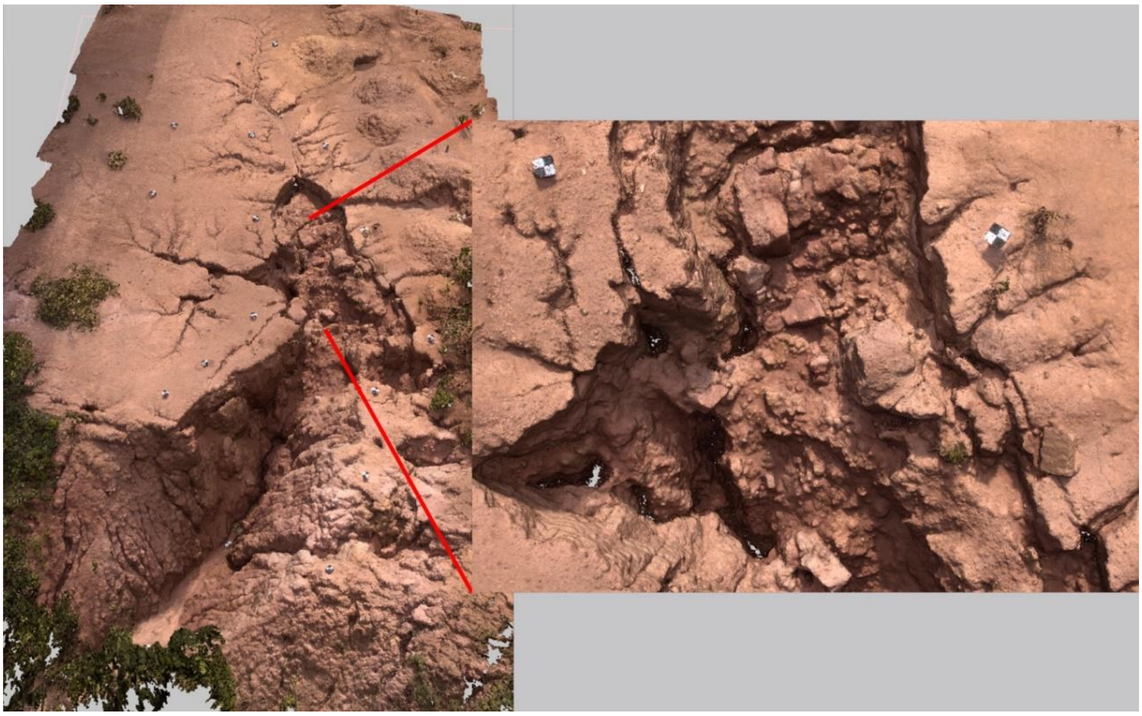

Fig. 5. Dense point cloud showing the 3D reconstruction of complex topographic areas inside the gully.

4.3.2 Sediment source dynamics

The significant changes found by the M3C2-PM method showed a high visual correlation with the observed differences between both DEMs in the area (Fig 6). Significant changes were detected in the topsoil, rill erosion and in the mass movements, such as gully sidewalls, inside the gully.

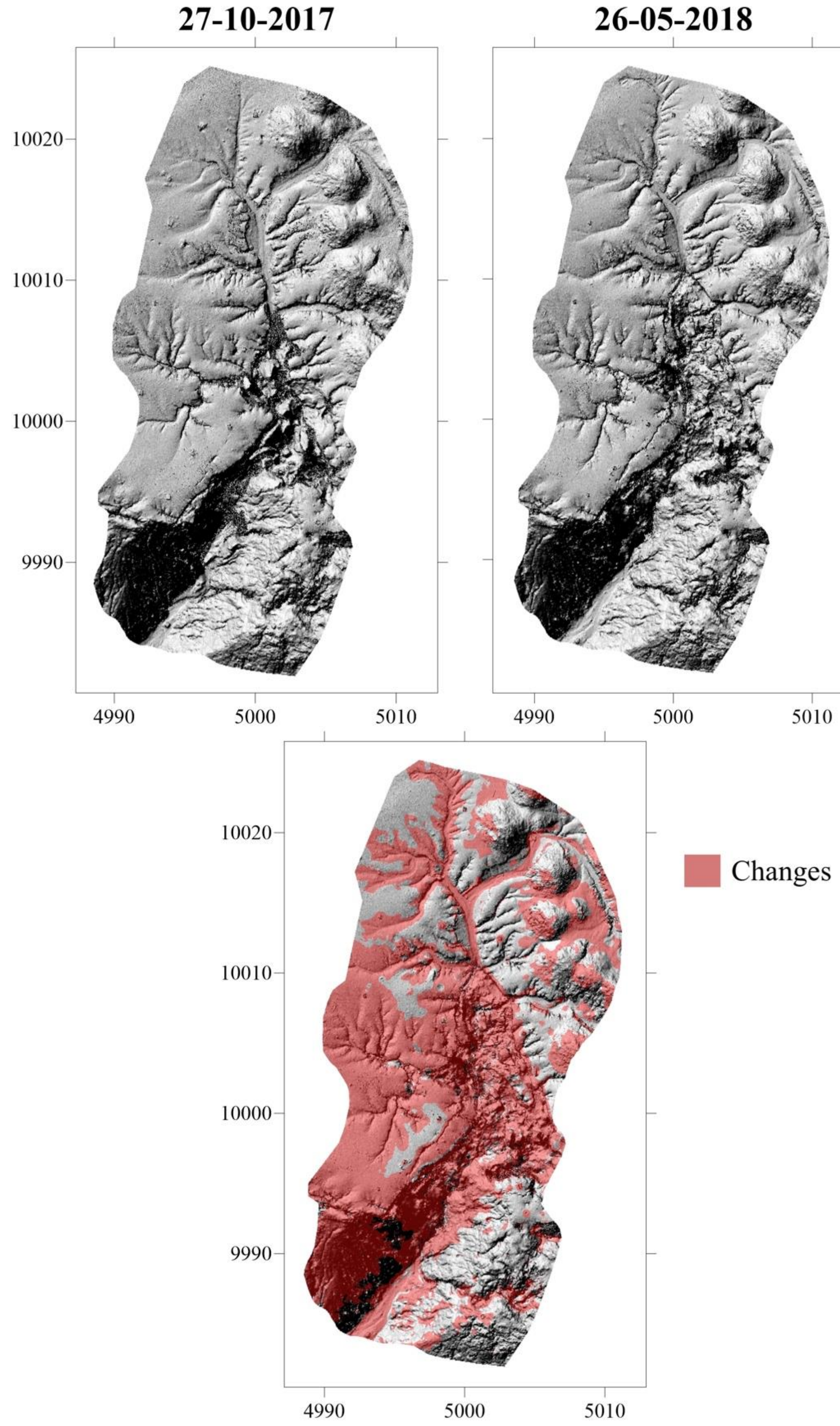

Fig. 6. DEMs for the two surveys and the map showing the significant change, in red, over the studied period.

During the study period, a total of 71 m^3 of sediments were generated (Table 3), and 76% of this volume was lost from the gully system. Almost all sheet erosion was stored in the area, contributing with less than 1% to the output of sediments from the gully. Rill erosion contributed 8% of the sediment yield in the gully, in large part being lost in the erosion process and only 0·76 m^3 stored in the channels.

Table 3. The relative contribution of each erosion process in the gully system between October 2017 and May 2018.

Erosion process	Sediments generation	Sediments stored	Sediments lost
	------------------------------	m^3	------------------------------
Sheet erosion	2·12	1·83	0·28
Rill	5·69	0·76	4·93
Gully sidewall	63·39	14·38	49·01
Total	71·20	16·97	54·22

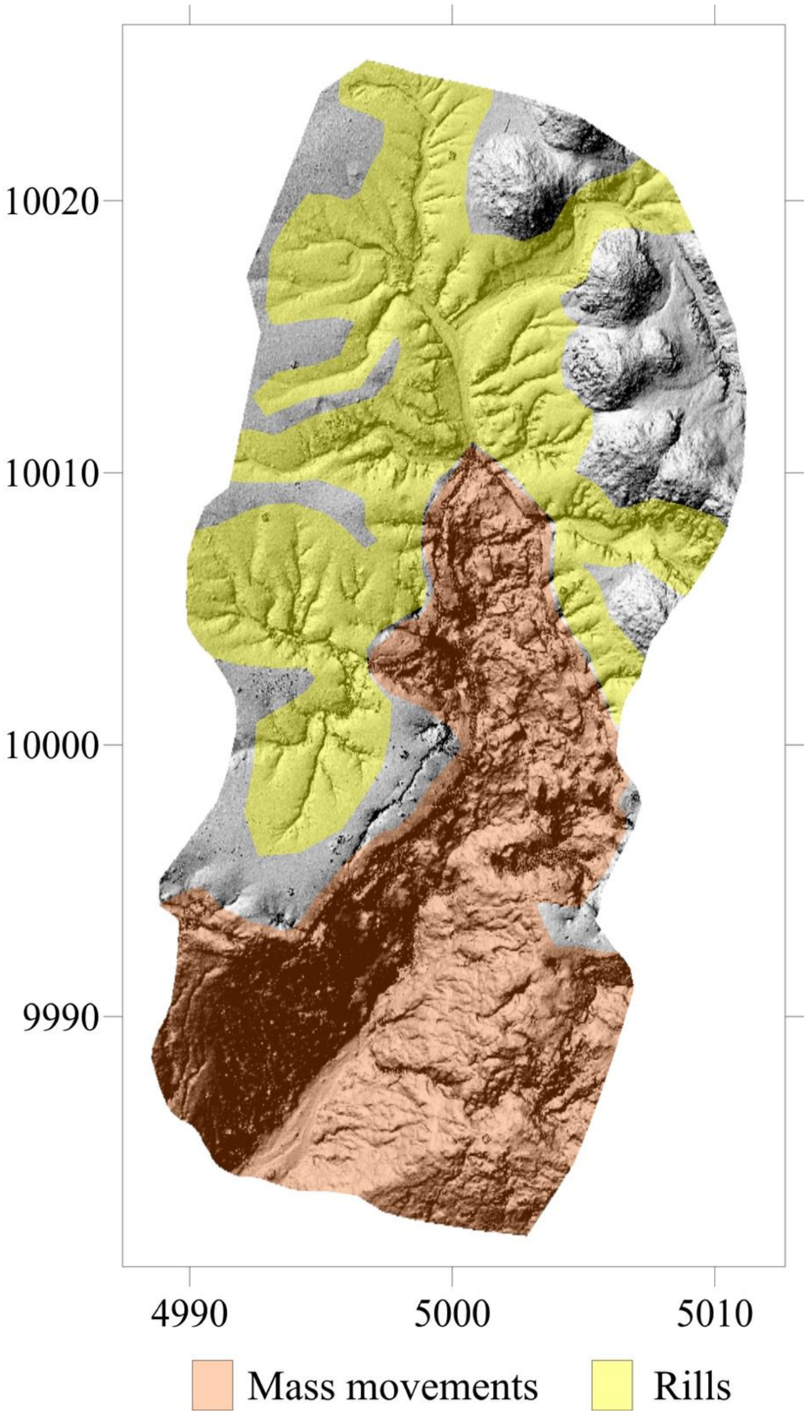

Fig. 7. Erosive processes (rills and mass movements) in the gully system.

The mass movements, including gully sidewall erosion, corresponded to 89% of the total sediments produced. However, 23% of that volume was deposited and stored in the gully bed. Nevertheless, of the total soil loss from the system, more than 90% was originated from the mass displacements promoted by the gully sidewall, while rill erosion accounted for approximately 9% of the sediment lost. The dynamics of the gully development, as well as the contribution of gully side wall retreat, are well represented by the difference between the two point clouds obtained by M3C2-PM (Fig. 7).

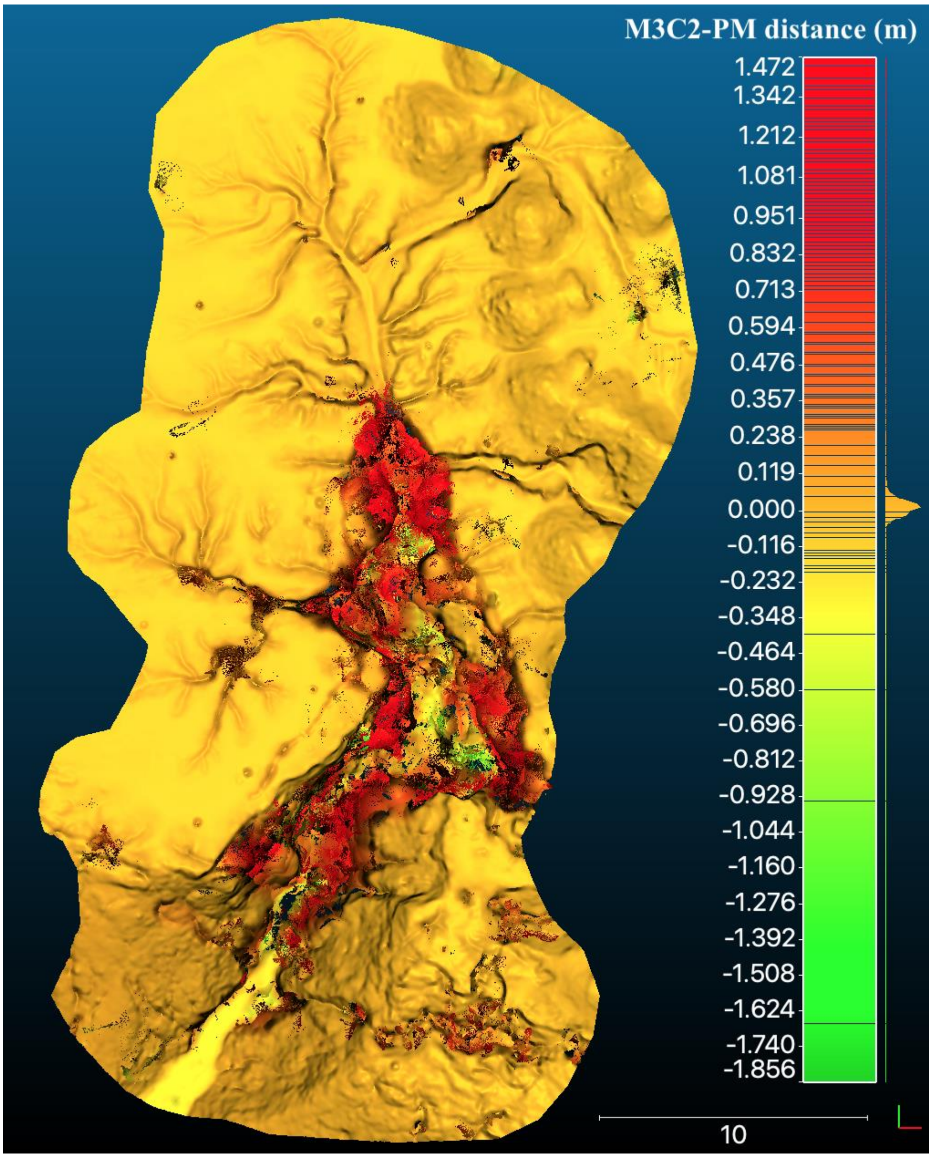

Fig. 8. Point cloud showing the difference (M3C2-PM distance) between the October 2017 and May 2018 gully surveys. Colour intensity shows relative amounts of erosion (red) and deposition (green).

4.4 Discussion

4.4.1 SfM measurements errors

For the study of active and dynamic environments, such as gullies, where the variations in the soil surface are in the order of centimetres and metres, RMSE values in the order of 4 mm for *xyz*, as found in this study, are acceptable. These values are lower than those founded by Agüera-Vega et al. (2018), who also studied topography reconstruction in complex areas using UAV. A millimetric precision on this kind of survey is very important, because allow the assessment of all erosion types occurring in the area, from laminar erosion to large mass movements.

The largest photogrammetric errors, obtained in the regions of the most complex and shaded topography (Fig. 4), can be reduced by performing flights on cloudy days with indirect light, increasing the number of oblique images and adding images taken in different height (Castillo et al., 2012, Gómez-Gutiérrez et al., 2014, Stöcker et al., 2015; Carbonneau and Dietrich, 2017, James et al., 2017b). Moreover, in areas where there is large soil movement, such as the gully environment, it is advisable to use dGPS rather than total station (with an arbitrary local coordinate system) to collect GCPs locations. This is to avoid repeatable GCPs surveys due to the soil movements, especially in points located in the bed and near the gully sidewalls.

4.4.2 Source of sediments in the gully

The present study showed that the gully growth occurred towards the main erosion channels present in the area (Figs. 6 and 7). The runoff concentrated in rills or depressions has the capacity to remove soil particles from the gully through sluicing (Lin et al., 2015). The gully side walls usually retreat due to three processes: mass displacement, the detachment of soil particles by splashes, or water running along gully banks (Chaplot et al., 2011). In the studied gully, the gully side wall retreated primarily due to the mass displacement, as showed by the M3C2-PM distance map (Fig. 8). These results correspond to those of Vandekerckhove et al. (2003) and Hosseinalizadeh et al. (2019).

In contrast to previous gully erosion studies (Prosser and Slade, 1994; Inoubli et al., 2017; Ben Slimane et al., 2018), sediment generation in the studied gully was predominantly by the mass displacement process due to the erosion of the gully side walls. These results are similar to those found by De Rose et al. (1998) and Betts et al. (2003). Mass movements of gully side walls are also recognized by Harvey (2001) as an important process in the absence of extreme rainfall events and have been related to reactivation of gullies.

Studies indicate that in stabilized gullies it is expected that the amount of sediment stored in the channels will exceed the volume of soil lost in the gully system (Kasai et al., 2001; Betts et al., 2003). In the present study, 54·22 m^3 was lost from the gully system in only 8 months of monitoring, a value similar to that was found by Ben Slimane et al. (2018) for annual production of sediment in gullies. While just 16·97m^3 of sediments generated were stored on the system.

These results showed that the studied gully is not stabilized yet. In that way, a detailed knowledge of the complex dynamics of gully evolution has implications for the correct management and application of stabilization practices of gully prone areas. The accelerated evolution of this gully demonstrates that conservation strategies should be applied in the early stages of the gully formation before the channels deepen and the mass movement processes accelerate the evolution of the gully erosion. Attempts to reduce the expansion of the gullies complex become less efficient in these advanced stages.

4.5 Conclusions

This study evaluated the relative contribution of the different erosive processes that occur simultaneously in a gully. For the first time, the sediment sources of a gully were quantified remotely and with millimetric precision. Through the SfM, it was generated high resolution measurements, allowing to evaluate even the contribution of sheet erosion in the generation of sediment of the gully. This opens up new possibilities in the studies involving the dynamics of gullies, since the understanding of the spatial and temporal behaviour of the erosive processes are important in the development of control strategies and monitoring of the evolution of a gullies complex.

The results revealed that the main source of sediment in the gully studied was due to the mass movement processes. Rills and laminar erosions contributed 9% and 1%, respectively, to the total sediment yield, while the mass movements corresponded with most of the sediment generation in the gully. Of the total sediment produced in the system, only 24% was stored in the gully, indicating its high activity and instability.

4.6 References

Agüera-Vega, F., Carvajal-Ramírez, F., Martínez-Carricondo, P., López, J.S-H., Mesas-Carrascosa, F.J., García-Ferrer, A., Pérez-Porras, F.J., 2018.

Allen, P.M., Arnold, J.G., Auguste, L., White, J., Dunbar, J., 2018. Application of a simple headcut advance model for gullies. Earth Surf. Process. Landf. 43, 202–217.

Bastola, S., Dialynas, Y.G., Bras, R.L., Noto, L.V., Istanbulluoglu, E., 2018. The role of vegetation on gully erosion stabilization at a severely degraded landscape: a case study from Calhoun Experimental Critical Zone Observatory. Geomorphology 308, 25–39.

Ben Slimane, A., Raclot, D., Rebai, H., Le Bissonnais, Y., Planchon, O., Bouksila, F., 2018. Combining field monitoring and aerial imagery to evaluate the role of gully erosion in a Mediterranean catchment (Tunisia). Catena 170, 73–83.

Betts, H.D., Trustrum, N.A., De Rose, R.C., 2003. Geomorphic changes in a complex gully system measured from sequential digital elevation models, and implications for management. Earth Surf. Process. Landf. 28, 1043–1058.

Blanco, H., Lal, R., 2010. Principles of soil conservation and management. Springer, Heidelberg, Germany, 620 pp.

Carbonneau, P.E., Dietrich, J.T., 2017. Cost-effective non-metric photogrammetry from consumer-grade sUAS: implications for direct georeferencing of structure from motion photogrammetry. Earth Surf. Process. Landf. 42, 473–486.

Carollo, F.G., Di Stefano, C., Ferro, V., Pampalone, V., 2015. Measuring rill erosion at plot scale by a drone-based technology. Hydrol. Process. 29, 3802–3811.

Castillo, C., Pérez, R.; James, M.R.; Quinton, J.N.; Taguas, E.V.; Gómez, J.A., 2012. Comparing the accuracy of several field methods for measuring gully erosion. Soil Sci. Soc. Am. J. 76, 1319–1332.

Casalí, J., Loizu, J., Campo, M.A., De Santisteban, L.M., Álvarez-Mozos, J., 2006. Accuracy of methods for field assessment of rill and ephemeral gully erosion. Catena 67, 128–138.

Cook, K.L., 2017. An evaluation of the effectiveness of low-cost UAVs and structure from motion for geomorphic change detection. Geomorphology 278, 195–208.

Conoscenti, C., Angileri, S., Cappadonia, C., Rotigliano, E., Agnesi, V., Maerker, M., 2014. Gully erosion susceptibility assessment by means of GIS-based logistic regression: a case of Sicily (Italy). Geomorphology 204, 399–411.

De Rose, R.C., Gomez, B., Marden, M., Trustrum, N.A., 1998. Gully erosion in Mangatu Forest, New Zealand, estimated from digital elevation models. Earth Surf. Process. Landf. 23, 1045–1053.

Desir, G., Marín, C., 2007. Factors controlling the erosion rates in a semi-arid zone (Bardenas Reales, NE Spain). Catena 71, 31–40.

Di Stefano, C., Ferro, V., Palmeri, V., Pampalone, V., Agnello, F., 2017. Testing the use of an image-based technique to measure gully erosion at Sparacia experimental area. Hydrol. Process. 31, 573–585.

d'Oleire-Oltmanns, S., Marzolff, I., Peter, K., Ries, J., 2012. Unmanned Aerial Vehicle (UAV) for monitoring soil erosion in morocco. Remote Sens. 2012, 4, 3390–3416.

Easa, S.M., 1988. Estimating pit excavation volume using nonlinear ground profile. J. Surv. Eng. 114, 71–83.

Ehiorobo, J.O., Audu, H.A.P., 2012. Monitoring of gully erosion in an urban area using geoinformation technology. J. Emerg. Trends Eng. Appl. Sci. 3, 270–275.

Fonstad, M.A., Dietrich, J.T., Courville, B.C., Jensen, J.L., Carbonneau, P.E., 2013. Topographic structure from motion: a new development in photogrammetric measurement. Earth Surf. Process. Landf. 38, 421–430.

Foster, G.R., 2005. Terraces and terracing. In: Hillel, D. (Ed.), Encyclopedia of Soils in the Environment. Academic Press, New York, pp. 135–143.

Chaplot, V., Brown, J., Dlamini, P., Eustice, T., Janeau, J.L., Jewitt, G., Lorentz, S., Martin, L., Nontokozo-Mchunu, C., Oakes, E., Podwojewski, P., Revil, S., Rumpel, C., Zondi, N., 2011. Rainfall simulation to identify the storm-scale mechanisms of gully bank retreat. Agric. Water Manag. 98, 1704–1710.

CloudCompare (version 2.10) [GPL software], 2019. Retrieved from. http://www.cloudcompare.org/.

Gómez-Gutiérrez, Á., Schnabel, S., Berenguer-Sempere, F., Lavado-Contador, F., Rubio-Delgado, J., 2014. Using 3D photo-reconstruction methods to estimate gully headcut erosion. Catena 120, 91–101.

Gómez-Gutiérrez, Á., Schnabel, S., De Sanjosé, J.J., Contador, F.L., 2012. Exploring the relationships between gully erosion and hydrology in rangelands of SW Spain. Z. Geomorphol. 56, 27–44.

Harvey, A.M., 1992. Process interactions, temporal scales and the development of hillslope gully systems: Howgill Fells, northwest England. Geomorphology 5, 323–344.

Harvey, A.M., 1997. Coupling between hillslope gully systems and stream channels in the Howgill Fells, northwest England: temporal implications. Geomorphologie 1, 3–20.

Harvey, A.M., 2001. Coupling between hillslopes and channels in upland fluvial systems: implications for landscape sensitivity, illustrated from the Howgill Fells, northwest England. Catena 42, 225–250.

Hosseinalizadeh, M., Kariminejad, N., Chen, W., Pourghasemi, H.R., Alinejad, M., Behbahani, A.M., Tiefenbacher, J.P., 2019. Spatial modelling of gully headcuts using UAV data and four best-first decision classifier ensembles (BFTree, Bag-BFTree, RS-BFTree, and RF-BFTree). Geomorphology 329, 184–193.

Inoubli, N., Raclot, D., Moussa, R., Habaieb, H., Le Bissonnais, Y., 2016. Soil cracking effects on hydrological and erosive processes: a study case in Mediterranean cultivated vertisols. Hydrol. Process. 30, 4154–4167.

James, M.R., Robson, S., 2012. Straightforward reconstruction of 3D surfaces and topography with a camera: Accuracy and geoscience application. J. Geophys. Res. 117, F03017.

James, M.R., Robson, S., d'Oleire-Oltmanns, S., Niethammer, U., 2017a. Optimising UAV topographic surveys processed with structure-from-motion: Ground control quality, quantity and bundle adjustment. Geomorphology 280, 51–66.

James, M.R., Robson, S., Smith, M.W., 2017b. 3-D uncertainty-based topographic change detection with structure-from-motion photogrammetry: precision maps for ground control and directly georeferenced surveys. Earth Surf. Process. Landf. 42, 1769–1788.

Kaiser, A., Neugirg, F., Rock, G., Müller, C., Haas, F., Ries, J., Schmidt, J., 2014. Small-scale surface reconstruction and volume calculation of soil erosion in complex Moroccan gully morphology using structure from motion. Remote Sens. 6, 7050–7080.

Kasai, M., Marutani, T., Reid, L.M., Trustrum, N.A., 2001. Estimation of temporally averaged sediment delivery ratio using aggradational terraces in headwater catchments of the Waipaoa River, North Island, New Zealand. Earth Surf. Process. Landf. 26,1–16.

Lague, D., Brodu, N., Leroux, J., 2013. Accurate 3D comparison of complex topography with terrestrial laser scanner: application to the Rangitikei canyon (NZ). ISPRS J. Photogramm. Remote Sens. 82, 10–26.

Lin, J., Huang, Y., Wang, M., Jiang, F., Zhang, X., Ge, H., 2015. Assessing the sources of sediment transported in gully systems using a fingerprinting approach: An example from South-east China. Catena 129, 9–17.

Lowe, D.G., 2004. Distinctive image features from scale-invariant keypoints. Int. J. Comput. Vision 60, 91–110.

Morgan, J.A., Brogan, D.J., Nelson, P.A., 2017. Application of Structure-from-Motion photogrammetry in laboratory flume. Geomorphology 276, 125–143.

Murtiyoso, A., Grussenmeyer, P., Börlin, N., Vandermeerschen, J., Freville, T., 2018. Open Source and Independent Methods for Bundle Adjustment Assessment in Close-Range UAV Photogrammetry. Drones, 2, 3.

Poesen, J., 2011. Challenges in gully erosion research. Landform Analysis. 17, 5–9.

Poesen, J., Nachtergaele, J., Verstraeten, G., Valentin, C., 2003. Gully erosion and environmental change: importance and research needs. Catena 50, 91–133.

Poesen, J., Vandekerckhove, L., Nachtergaele, J., Oustwood Wijdenes, D., Verstraeten, G., van Wesemael, B., 2002. Gully erosion in dryland environments. In: Bull, L.J., Kirkby, M.J. (Eds.), Dryland Rivers: Hydrology and Geomorphology of Semi-arid Channels. John Wiley & Son Ltd., pp. 229–262.

Prosser, I.P., Slade, C.J., 1994. Gully formation and the role of valley-floor vegetation, southeastern Australia. Geology 22, 1127–1130.

Seiz, S.M., Curless, B., Diebel, J., Scharstein, D., Szeliski, R., 2006. A Comparison and Evaluation of Multi-View Stereo Reconstruction Algorithms. IEEE Conference on Computer Vision ad Pattern Recognition. IEEE Computer Society, New York.

Sidorchuk, A., Marker, M., Moretti, S., Rodolfi, G., 2003. Gully erosion modelling and landscape response in the Mbuluzi River catchment of Swaziland. Catena 50, 507–525.

Stöcker, C., Eltner, A., Karrasch, P., 2015. Measuring gullies by synergetic application of UAV and close range photogrammetry – A case study from Andalusia, Spain. Catena 132,1–11.

Valentin, C., Poesen, J., Li, Y., 2005. Gully erosion: impacts, factors and control. Catena 63, 132–153.

Vandekerckhove, L., Poesen, J., Govers, G., 2003. Medium-term gully headcut retreat rates in Southeast Spain determined from aerial photographs and ground measurements. Catena 50, 329–352.

Vandekerckhove, L., Poesen, J., Wijdenes, D.O., de Figueiredo, T., 1998. Topographical thresholds for ephemeral gully initiation in intensively cultivated areas of the Mediterranean. Catena 33, 271–292.

Zabihi, M., Pourghasemi, H.R., Motevalli, A., Zakeri, M.A., 2019. Gully erosion modeling using GIS-based data mining techniques in Northern Iran: a comparison between boosted regression tree and multivariate adaptive regression spline. In: Pourghasemi, H., Rossi, M. (Eds.), Natural Hazards GIS-based Spatial Modeling Using Data Mining Techniques. Advances in Natural and Technological Hazards Re- search. vol. 48. Springer, Cham.

5. General Conclusions

This thesis contributes to a new insight on studies of erosive processes in the Earth's surface, by investigating the efficiency and accuracy of digital photogrammetry in a detailed study of the main types and scales of occurrence of water erosion.

Considering that soil erosion is composed of three sub-processes that occur on the soil surface: erosion, transport and deposition. Collecting sediment and runoff allows only the assessment of soil volume lost, not soil erosion volume. Thus, this thesis presents techniques that allow the visualization, spatialization and quantification of soil movement during erosion-transport-deposition processes, allowing to distinguish the differences between soil erosion volume and lost soil volume, besides investigating the relative contribution. of each type of erosion in the monitored area. The erosion map, represented by the erosive processes in the area, is a powerful tool in the elaboration of effective soil and water conservation management strategies.

Under laboratory and controlled conditions, the digital close-range photogrammetry provided a detailed study of the development of rill erosion, allowing the extraction of morphological indicators and quantification of soil movement during runoff with millimetric precision. In addition, it was possible to correlate water flow rate and slope gradient with the rill erosion development.

It was also evaluated the use of SfM combined with UAV images, in obtaining soil loss measurements in areas where channelized erosion is not the main mechanism. This represents the first time this kind of research was conducted, providing valuable insight into a new direction for soil erosion studies in erosion plots. The results of the soil losses obtained by UAV-SfM presented a high correlation with the sediments collected in the plots. This is of great relevance in the context of the monitoring and modelling of water erosion, since the quantification of soil loss around the world is mainly done using plots, a method that presents high operational cost. In addition, the study of laminar erosion through the UAV-SfM allows not only to calculate the soil loss values but to visualize the spatial variation of the erosion process (detachment, transport and deposition) practically in real time along the area.

Finally, the application of the UAV-SfM technique in gully erosion was evaluated. For the first time, a study was carried out evaluating the relative contribution of the different types of erosion (sheet, rill and gully sidewall) in the gully development. This was possible due to the millimetric level of precision of the point clouds, allowing to evaluate even the contribution of the laminar erosion, which is new in gullies studies. As a result, it was possible to quantify sediments volumes stored in the channels and lost from the gully system, as well as to determine the main sediment sources. Since gully development studies are quite difficult to perform on field, due to the 3-D nature and the several factors acting simultaneously, the UAV-SfM proved to be effective in the gully monitoring and could be an important tool in the development of strategies of control and mitigation of this serious environmental problem that affects several agricultural and urban areas in tropical regions.

In summary, the results presented here indicate that the use of ground and air-based photogrammetry are precise tools in detecting soil surface changes and can be used to assess water erosion in its various forms of occurrence in nature. In addition, the UAV-SfM has proven to be a very useful technique for monitoring erosion over time, especially in hard-to-reach areas.

6. Future Work

This thesis advances our understanding of the use of ground and air-based photogrammetry for soil erosion assessment. However, it also highlighted several challenges, that would provide interesting future work.

- The results demonstrate that on steep slopes the soil erosion is dominated by the rill erosion with less rill network density. It would be interesting to develop a time-lapse study in order to see the rill erosion evolution in real time. To make it possible, it is necessary to think about an experimental design to avoid the water reflection during the 3-D reconstruction of the soil surface.
- The results of the soil losses obtained by the UAV-SfM technique presented high accuracy when compared to the sediments collected from the erosion plots. However, it would be interesting for future studies to evaluate the effectiveness of UAV-SfM in water erosion monitoring with the presence of vegetation and different levels of

soil cover. For this, the accuracy of the mathematical algorithms that filter the point cloud vegetation in order to estimate the covered soil surface should be tested.

- The 3-D reconstruction of the studied gully presented millimetric precision. However, due to the complexity of the soil surface in the gully, shading areas present a lower density of points, affecting the level of detection in these regions. Thus, it would be interesting for future studies to combine UAV and terrestrial images, using consumer-grade or smartphones cameras, in gully modelling. In addition, in large gullies, where it is difficult to install control points, it would be interesting to test the effectiveness of UAV coupled with post-processed kinematic (PPK) or RTK GPS in the generation of DEMs and point clouds.

Appendix A

ANOVA results for the effects of slope gradient and water flow rate on rill erosion and soil loss (Chapter 2).

Factors	df	Sum Sq	Mean Sq	F value	P (> F)
Rill erosion					
Slope	1	1·3488	1·3488	161·5766	$4{\cdot}32 \times 10^{-6}$ ***
Water flow	1	10·3549	10·3549	1240·4187	$3{\cdot}86 \times 10^{-9}$ ***
Slope × Water flow	1	0·0486	0·0486	5·8185	0·047 *
Residuals	7	0·0584	0·0083		
Soil loss					
Slope	1	0·0362	0·0362	1·5714	0·2502
Water flow	1	5·4430	5·4430	236·0131	$1{\cdot}19 \times 10^{-6}$ ***
Slope × Water flow	1	0·4785	0·4785	20·7468	0·002621 **
Residuals	7	0·1614	0·0231		

Significance: *** P< 0·001, ** P<0·01, * P<0·05